Modelling Microstructural and Interfacial Phenomena in Welding and Irradiation Processes for Fe-based Systems

by

Francisco Javier Pérez Pérez

A Doctoral Thesis

Submitted in partial fulfilment of the requirements
for the award of Doctor of Philosophy of
Loughborough University

March 2000

Abstract

In this thesis, different modelling techniques, including physically based molecular dynamics simulations and empirical models using neural network architectures have been used to address particular problems in the understanding of microstructural development in iron-based systems. The two main areas of investigation are concerned with the prediction of composition and mechanical properties of steel welds and the effect of irradiation on the grain boundary microstructure of α-iron, both very important industrial issues.

Microstructural evolution models in steel welds require weld metal composition as their starting point. Extensive analyses have been carried out concerned particularly with the prediction of weld metal chemistry, and also complex mechanical properties such as toughness, using neural network techniques and a database developed for one pass per side submerged arc welds typical of those used in the manufacture of linepipe. The neural network techniques used were based on a Bayesian framework, implemented using Markov chain Monte Carlo methods. The results showed a significant advantage in the use of neural network models for prediction of toughness compared with simpler regression analyses.

In order to study the effects of irradiation on the structure of Fe-based systems, a molecular dynamics methodology was initially set up to study the equilibrium relaxed atomic configuration of symmetric tilt and twist grain boundaries in α-iron. These structures have been classified in terms of both the energy and width of the grain boundary region and the atomic arrangement has been also analysed for the tilt models in terms of structural units. Radiation damage has then been studied near the relaxed structures of a symmetrical tilt and a symmetrical twist boundary in α-iron. Collision cascades have been initiated in the structure by imparting an initial energy of 1 keV to a single Fe atom, i.e. a primary knock-on atom (PKA). The subsequent interaction of the cascade with the grain boundary has been studied using molecular dynamics simulations. As a result of radiation, reordering is produced in the atomic structure of the boundaries, the damage being more pronounced in the twist model studied. Clusters of interstitial atoms are produced at the boundary. Changes in the properties of the interfaces after irradiation are discussed.

Acknowledgements

A mi hermano

Contents

Chapter 1

Introduction

1.1 Overview

Models are a simplification of the real phenomena that occur in nature. Science, and in particular materials science, has evolved by modelling nature and by necessity simplifying it. A general definition of a model is as follows:

"A model is an idealisation. ... At worst, a model is a concise description of a body of data. At best, it captures the essential physics of the problem, it illuminates the principles that underline the key observations, and it predicts behaviour under conditions which have not yet been studied. ... A model is a transfer function: it transforms the inputs into the outputs. It may take the form of algebraic, differential, or integral equations, and these may be embedded in a discretised computation (a finite element computation or an atomistic computation, for example)" [1]

Therefore, a model is firstly, a simplified description of the system, i.e. the idealisation, and secondly the formalisation of these ideas in a mathematical way. Models can be very complex mathematically even with a very simplified description of the process to be modelled. Often, the resulting equation systems are analytically insoluble requiring further simplifications of the model for their solution. However, computers may be able to provide an exact numerical solution in some cases.

Computer modelling is the implementation of a model in a computer system, e.g. in a computer code. Once a model is implemented in the computer, the system can be simulated. Computer simulations are the study of the responses of a modelled system by a given choice of inputs which simulate real events. Computers can provide numerical solution of the simulations to a degree of precision which may be limited by the available resources.

Nowadays, computer modelling plays a key role in the way we do science. Computer modelling is the link between experimental results and theory. The model can

be tested on the computer and improved as a consequence of its results compared with real data in an iterative improvement process. The requirements needed to compare with both theoretical predictions and experimental results can readily be made in computer simulations because of the ease with which inputs can be changed in the computer code.

Development in materials science and industry has been clearly enhanced by the use of computer modelling. For example, computers provide a 'virtual laboratory' where the response of the material can be predicted under conditions which are not easy (or impossible) to produce in the laboratory. One example is the simulation of the materials behaviour for the design of nuclear fusion reactors. Both material properties in service and initial processing conditions can be simulated, allowing both optimisation of manufacturing and correct materials selection at a first attempt.

Modelling of materials and industrial processes is not an easy task due to their complexity. A good model of a material has to capture in a code (or equations) the response of the material in several situations. This model has to take into account that the performance of a material can evolve with time and also all the various mechanisms that contribute simultaneously and synergistically in typical materials problems.

Models can be classified in two broad categories: empirical and physical [1]. Empirical models use approximations to fit experimental data. Therefore, empirical models cannot contain more knowledge than the data used in its creation. The simplest way to obtain an insight into the process to be described using the data provided is through standard linear regression models. In linear regression, the data can be fitted to a linear form, obtaining as a result a linear dependence between inputs and outputs.

More sophisticated methods like neural networks can be used not only to obtain the linear dependencies but also the non-linear relationships between inputs and outputs which are the most common case in materials behaviour. Neural networks are empirical models which have a proven ability of finding hidden relationship in sets of data. Neural network models have been mainly used in engineering where material problems are so complex that there are no adequate physical models to describe them. There are often large databases concerned with the processes of interest, e.g. welding, which can be presented to a network. Once the network has learnt from the data it is able to predict outputs from a given set of previously unseen inputs of interest.

A physical model is the best we can have, because it is based on well established laws which gives the model sound predictive capability. A physical model is based in

the physical mechanisms which can be described by classical and quantum mechanics, thermodynamics, kinetic theory etc.

Physical models of materials can be classified into different length and time scales. Four main broad ranges in length and time scale can be distinguished: electronic, atomistic, microstructural and continuum, see Figure 1.1. This distinction is based on the different physical theories and models which can be developed to describe material properties.
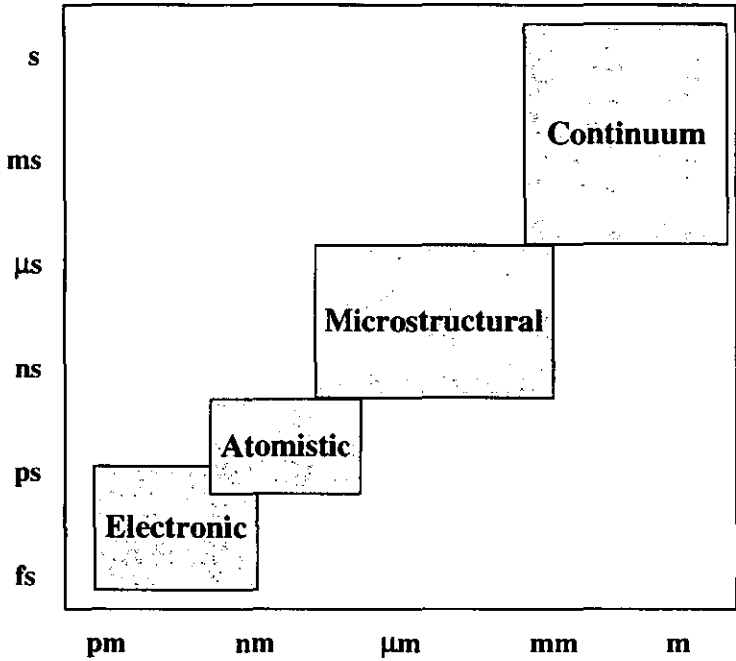
Figure 1.1: Length and time scales hierarchy

'Ab initio' methods describe the material at the electronic level. The 'ab initio' calculations only need one input which is the specification of the atomic number of the elements present in the system. These methods can predict from first principles, i.e. Schrödinger's equation, the energy, crystal structure and optical properties of most simple materials. Density functional methods have become the most widely used 'ab initio' methods for describing electrons in real materials [2]. However, even with some simplifications which speed up the calculations at the expense of losing fundamentality, 'ab initio' methods are at present limited to systems containing 100-1000 atoms.

Calculations at the electronic level often determine the interatomic force field that is the input for larger-scale molecular dynamics (MD) and Monte Carlo simulations

which can involve millions of atoms. Atomistic calculations can provide information on defect structure. Molecular dynamics is a physically-based model at the atomic scale. However, MD incorporates an empirical part, which is the interatomic potential. The empirical interatomic potential is a function which is fitted to some physical properties of the materials which can be obtained by 'ab initio' calculations.

Every scale can be thought as building on the previous one [3] and requires information to be passed over. The atomistic scale considers the electrons collectively, the microstructural scale considers the atoms collectively, and finally the continuum considers the microstructure of the material (grains) as a collective. In this process of 'coarse graining', one moves up the length scales, so that one can simulate ever larger systems but at the expense of fundamentality.

The properties and performance of materials can be ultimately explained in terms of the properties of atoms and their mutual interactions. However, it is impossible to use only atomistic theories to simulate real materials on a computer due to the large number of atoms involved in the continuum scale. Therefore, it is necessary to develop new models which are able to link between different length scales, the so-called multi-scale modelling methods. This is a new field of research which is now possible due to the increasing computer power available. Multi-scale modelling not only has need of the computer power but also of interdisciplinary collaborations which are intrinsic to the materials science field. Different disciplines are related with the different scales mentioned before, being broadly describable as physics in the electronic scale, chemistry in the atomistic, materials in the microstructural and engineering in the continuum.

Radiation damage near grain boundaries is a clear example of how phenomena at the atomic scale can affect the behaviour of the material at bigger scales. The lifetime of a nuclear reactor is clearly dependent on the effects of the radiation on its components. Radiation can provoke imperfections in the structure of the steels used in nuclear reactors. In particular, this damage has a key role at grain boundaries, where it is known that defects can accumulate and impurities segregate due to radiation effects. Changes at the atomic level of grain boundaries can change drastically the physical properties of the steels which may provoke failures on the reactor.

In this thesis, different modelling techniques, including empirically based models using neural network methods and physically based molecular dynamics simulations have been used to address particular problems in the understanding of microstructural development in iron-based systems.

There is no physical model able to describe the complexity of all the reactions which take place in a weld pool. Neural network techniques are employed in this thesis

4

to analyse two important issues in arc submerged welds; the chemical composition and toughness of the final weld. Neural network results are based on an experimental database which take into account several parameters of importance in the preparation of the weld, as well as the properties of the final product.

Molecular dynamics simulations have also been carried out in this thesis to study radiation damage near grain boundaries in α-iron. This thesis is an starting point for the study of the effects of radiation damage in grain boundaries of steels in the atomistic scale. Steel is a very complex system to be modelled, and there is no good interatomic potential to describe it. A good approximation is to choose pure iron in its bcc structure since steel is an Fe-based alloy and the solubility of carbon in ferrite is very low.

The damage produced by collision cascades in perfect crystallographic structures, such as α-iron, as a result of irradiation have been extensively studied by computer simulations [4]. However, the mechanisms that occur at the atomic level near defects such as grain boundaries are not well understood. One of the main questions is how the different atomic structure of grain boundaries can affect to the radiation damage process, the accumulation of defects and the segregation of impurities towards grain boundaries. The knowledge of these mechanisms are of extreme importance.

1.2   Layout of thesis

This thesis is organised as follows. Following this brief introduction, Chapter 2 describes both the neural network and molecular dynamics techniques which are employed through this work. After a general introduction on the main characteristics of neural network models, the particular model used in this work is introduced. This chapter also includes an introduction to the Bayesian probabilistic theory and Markov chain Monte Carlo methods applied to this particular neural network models. It is not the intention of this chapter to explain in detail these two issues, but rather to explain how the neural network training and generalisation processes are implemented. Particular details of the different stages of the application of the model are presented; the pre-handling of the data prior to 'feeding' the network and the code details for training the network, and making predictions. The second part of this chapter contains a description of the classical molecular dynamics method employed in this work. A detailed description of the interatomic potential used to simulate the interaction between Fe atoms is also presented.

The application of the neural network technique to the prediction of weld metal chemistry and toughness is detailed in Chapter 3. The submerged arc welding process,

as well as the database which has been used to train the network, is described at the beginning of the chapter. Whilst neural network results for the prediction of the final weld composition of every element have been performed, only the results for nickel and titanium are presented explicitly to illustrate the analysis procedure. Comparison with linear regression models is also presented for the prediction of weld metal composition. In this chapter, the neural network model is also applied to predict complex mechanical properties such as toughness and comparisons are made with the chemistry predictions.

The second part of this thesis deals with the application of molecular dynamics techniques to the simulation of radiation damage near grain boundaries in α-iron. Chapter 4 describes the relaxed atomic structure of symmetrical tilt and twist grain boundaries in α-iron. The geometrical description of a symmetrical grain boundary based on the coincidence site lattice model is presented, as well as its implementation in a computational block for simulation purposes. The molecular dynamics simulation procedures employed to relax the boundaries are explained. In this chapter the analysis of the atomic structures are based on the repeated configuration of atoms, energy and width of the boundaries.

Collision cascades generated near two different symmetrical grain boundaries and their evolution are studied in Chapter 5. Collision cascades have been initiated in the structure by imparting an initial energy of 1 keV to a single Fe atom. Defects and atomic reordering in the grain boundary region of both models have been analysed and discussed.

The final chapter of this thesis, summarises and discusses the main conclusions from this research and suggests areas for future investigation.

Chapter 2

Modelling techniques

2.1 Introduction

In this thesis, different modelling techniques, including physically based molecular dynamics simulations and 'blind' empirical models using neural network architectures have been used to address particular problems in the understanding of microstructural development in iron-based systems. The two main areas of investigation are concerned with the prediction of composition and mechanical properties of steel welds and the effect of irradiation on the grain boundary microstructure of α-iron, both very important industrial issues.

In the following sections a general description of both molecular dynamics and neural network techniques is made. Also, the particular details of each technique which are particularly used in this work are pointed out.

2.2 Neural networks

2.2.1 Why neural networks?

When there is no theory to describe a phenomenon or the only possible theory deals with many parameters, it is difficult, if not impossible, to understand properly (from first principles) precisely what is happening. It is then that the scientific community has no option other than to obtain as much information as possible from the process studied and analyse it in detail looking for relationships between parameters through whichever statistical method is available to get ideas and to create a model. The use of artificial neural networks has gained much popularity in both the private sector and the scientific community during the last decade [5], as a powerful tool for data analysis.

The advantages of using neural network techniques compared with other simple regression methods used to solve problems in the fields of Physics and Chemistry

are not completely clear [6]. In most cases the standard methods of data fitting are good enough if we take into account that they will provide accurate results with a lower number of adjustable parameters compared with a neural network technique. However, neural network techniques are worth using when there are data coming from experiments and there is no approximate theory to describe a phenomenon.

Neural network models are becoming more common in the materials science field. In particular, neural networks have been applied to subjects like mechanical properties, processing and welding [7]. The lack of physical models to describe these complex phenomena where a lot of parameters are involved has favoured the increasing use of neural networks for their study. In particular the use of artificial neural networks has lead recently to new approaches on this field. For an actual review of neural network models and their application in the materials science field see [8].

Neural networks are described in detail in the following section and their application to the prediction of weld chemistry and toughness is discussed in Chapter 3. In this work a database provided by British Steel, also discussed in detail in Chapter 3, has been used. This database contains in depth information on chemical, mechanical and microstructural properties of welding processes.

In addition to the prediction of weld chemistry and toughness using neural network models this work attempts to compare neural network techniques with simple regression analyses where possible. Neural network techniques for regression are more attractive because they overcome some of the disadvantages of standard regression techniques. For example, regression analysis is limited to a few input variables and one output variable. By contrast, neural networks can be used to predict several output variables with also several input variables (if the quantity of data available is enough). The most important advantage of artificial neural network models is their capacity to represent a great variety of non-linear relationships compared with normal regression methods. In linear models the analysis begins with the prior linear choice of a relationship between the output and input variables, and this linear relationship is applied across the entire input space. The ability of a good generalisation in regions where data are not available is one of the main properties of a neural network model. One of the setbacks of neural network models is that they require much more computer processing power than traditional methods. However, with the advantage of more powerful computing systems, this causes increasingly fewer obstacles. Also, the number of parameters involved in a neural network model is usually big and of course with no physical meaning. A final setback of neural network models is related with the big number of data they need to determine all their parameters.

2.2.2 What is a neural network?

A neural network as a mathematical model should properly be referred to as an artificial neural network, ANN, to differentiate it from biological neural networks which are in the human brain [5]. The design of an artificial neural network was inspired by the structure of the human brain [9]. In the brain, a typical neuron collects signals from other neurons through a host of fine structures called dendrites. This idea when modelled mathematically results in an artificial neural network model.

There is no universally accepted definition of an artificial neural network and many definitions have been given in the literature. A general definition of an artificial neural network is given here:

"A neural network is a computing system made up of a number of simple, highly interconnected nodes or processing elements, which process information by its dynamic state response to external inputs" [10]

The goal of a neural network, when used for regression problems, is to map a set of input patterns to a corresponding set of output patterns. To do this the network must first learn from a series of past examples how sets of input and output data correspond to each other. The network then applies what it has learned to a new input pattern to predict the appropriate output.

2.2.3 Feed forward neural networks

Almost any mapping between spaces can be approximated to arbitrary precision by feed forward neural networks. A schematic representation of the architecture of a typical feed forward neural network is shown in Figure 2.1. In this example the architecture of the artificial neural network has one input layer with two input units, one hidden layer with four hidden units and one output layer with one output unit.

In a feed forward network the data flow from input to output units is strictly forwards, no feedback, i.e. connections extending from the output units to the input units in the same layer or in previous layers are not present. The network in Figure 2.1 is fully connected, every node is connected with every node in the next layer and with the unit in the output layer. The units in the hidden layer are responsible for the non-linearity of the net.

In order to begin to explain how the net model works the ideal representation given by Figure 2.1 has to be mathematically implemented. The function which implements the mapping between inputs, $\vec{i}$, and the output, o, must be defined (just one output considered for simplicity). This function $o = f(\vec{i}, \theta)$ can be expressed as follows:

$$o(\vec{i}, \theta) = b^{(0)} + \sum_k \omega_k^{(io)} i_k + \sum_l \omega_l^{(ho)} f_l$$
$$f_l = \tanh(h_l)$$
$$h_l = b_l^{(h)} + \sum_k \omega_{k,l}^{(ih)} i_k \tag{2.1}$$

where the weights ω and biases b are the parameters of the net. The parameter vector θ of the net is made up of the weights ω and biases b. The input layer merely distributes the inputs, $\vec{i}$, onto the hidden layer. It is on the hidden layer where the input data are first changed. The input to the k node on the input layer is represented as an input vector $\vec{i}$, with components i_k ($k = 1$ to n). Every input is multiplied by its corresponding weight factor, $\omega_{k,l}^{(ih)}$, and an internal bias is added, b_l^h. The transfer function on the hidden units is a function of the weighted total input sum plus the internal bias, h_l. It is possible to choose any non-linear function, but in regression problems sigmoid functions are especially used. In this work the hyperbolic tangent, $f_l(h_l) = \tanh(h_l)$, which has been shown to give a good performance in neural network models [5], is selected as a transfer function for the hidden units. On the output unit there is no non-linear transfer function and the contributions from hidden f_l and input layer i_k are only weighted $\omega_{l,j}^{(ho)}$ and $\omega_{k,j}^{(i,h)}$, and a bias is added b_j^o.

The increasing of units in the model, particularly hidden units, will make a more complex model with a considerable amount of parameters to be determined. The model has to be trained with the data available in order to fit this parameters. Previous to the training stage a pre-handling of the 'rough' data coming for the experiments is necessary.

2.2.4 Normalising and scaling inputs

The initial stage where data are prepared to feed the network is of crucial importance for the success of the neural network technique. The results will be more accurate if the amount of training and test data available is large and quite representative of the whole range over which the inputs and outputs vary.

Once it has been decided which inputs and outputs (different columns in an input file) are to be analysed from the database and once they have been extracted, it is necessary to have a look for possible 'outliers' or 'wrong' values, which are obvious typographic errors representing physically incorrect data. In addition the amount of useful data are reduced because of 'missing data'. Sometimes there is no value for one of the inputs and the data pair (corresponding inputs and outputs) cannot be used,
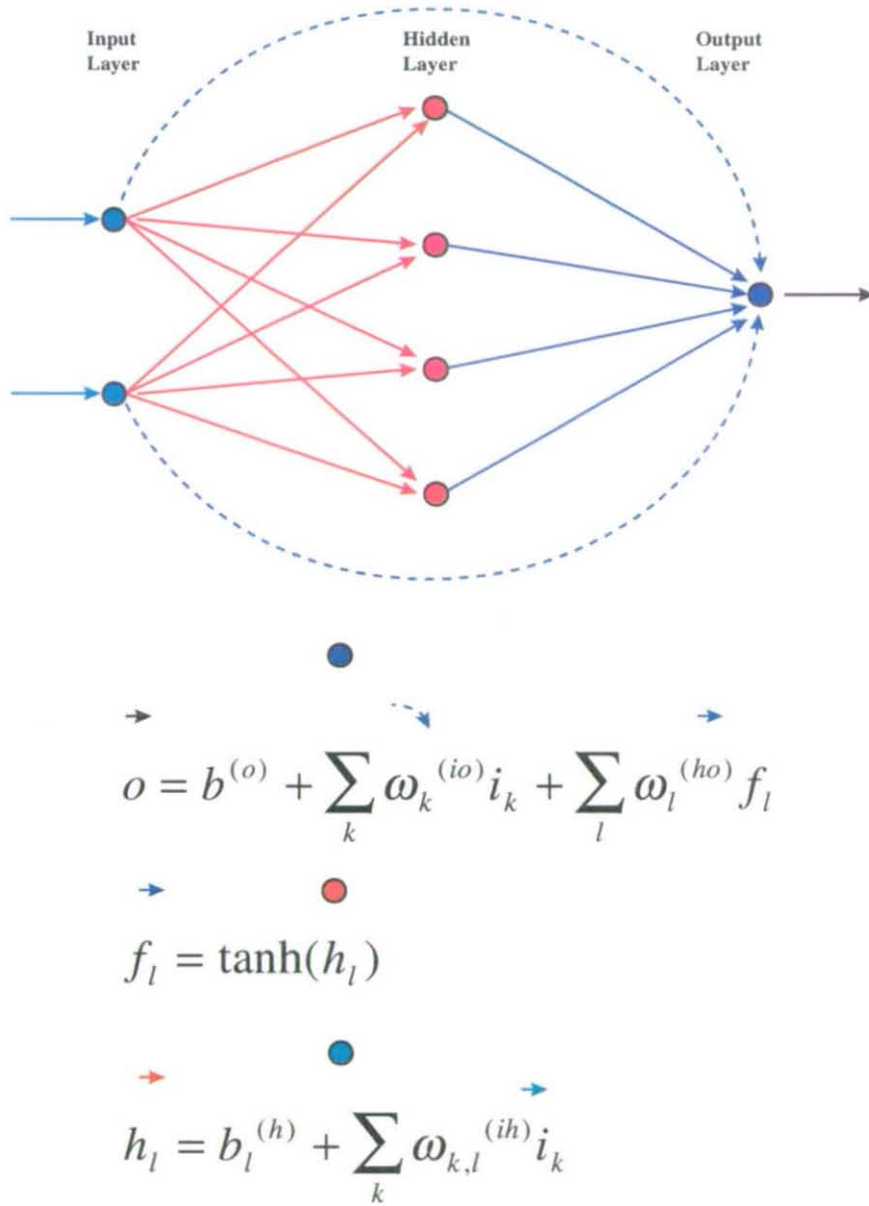
Figure 2.1: Neural network architecture

$$o = b^{(o)} + \sum_k \omega_k^{(io)} i_k + \sum_l \omega_l^{(ho)} f_l$$

$$f_l = \tanh(h_l)$$

$$h_l = b_l^{(h)} + \sum_k \omega_{k,l}^{(ih)} i_k$$

reducing the amount of data available (the number of rows in an input file). Missing data are one of the main setbacks in neural network methods reducing considerably the quantity of data available.

In artificial neural network training it is useful to scale and normalise the input and output values to a finite range. It is recommended that inputs and target variables should be scaled with zero mean and normalised in the range [-1,1] since within this range the selected transfer function varies appreciably providing a much more sensitive response, as is seen in Figure 2.2. In this way, the search for optimal parameters is easier because the weights do not run to extreme values.
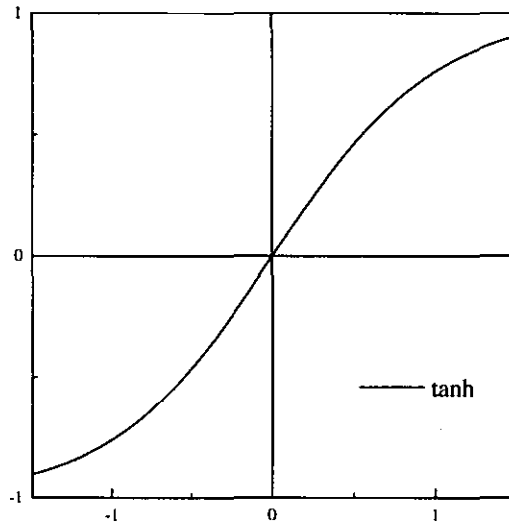
Figure 2.2: Hyperbolic tangent transfer function.

There are several ways to normalise and scale the data and it makes no difference which method is used. It is quite common to scale the data with zero mean and with a desired standard deviation as follows:

$$x_{i,norm} = \frac{x_i - \bar{x}}{\text{std}}\text{nstd} \tag{2.2}$$

where x_i identifies each value of the input or output column, $\bar{x}$ is the mean of the data in this column, nstd is the new standard deviation value, usually chosen equal to 1 and std is the standard deviation of the raw data defined by :

$$\text{std} = \frac{\sum_i^N (x_i - \bar{x})^2}{N - 1} \tag{2.3}$$

12

where N is the number of data pairs.

An alternative method consisting of a zero mean scaling and a normalisation in the range [-0.5,0.5], is defined by:

$$x_{i,norm} = \frac{x_i - x_{\min}}{x_{\max} - x_{\min}} - 0.5 \qquad (2.4)$$

where $x_{\min}$ and $x_{\max}$ are the minimum and maximum values, respectively, of the raw data.

Once a normalised and physically correct data set is obtained, approximately half of the data will be used for training the net and the other half for testing the model. A previous step to select the data for training and testing is the randomisation of the data. In this way representative values in the whole range covered by the database are included in both data sets.

2.2.5 Training and generalization

The training data set is a set of known input-output patterns which is repeatedly presented to the network in a process which minimises a particular error function, i.e. backpropagation of errors. In this process the parameters of the net are adjusted until the specified input yields the desired output. The test data are used in another phase of the process to check how good the approach is, and to ensure that net generalises properly. The desired final result would be a network that is both stable and convergent.

The main goal of the neural network training process is to obtain the parameters of the net, θ, which best accomplish the mapping between input and output values. To do this, the net learns from the data and in particular from the data pairs available in the training set $(\vec{i}^{(i)}, t^{(i)})$, being every data pair composed of inputs $\vec{i}^{(i)}$ and associated targets $t^{(i)}$. The parameters of the net are determined during the training process starting from an initial set of random values and updated in the light of the training data.

During the learning phase the input pattern is fed into the neural network and the output is generated following Equation 2.1, then this output is compared with the 'true' output and an error is obtained on the prediction. The purpose of the learning phase is to calculate the optimal weights to minimise this error, i.e. average sum of squared errors, *sse*, which is defined by:

$$sse = \frac{\sum_{i=1}^{N}(o-t)^2}{N} \qquad (2.5)$$

where o is the output (predicted value) of the network, t is the true value from the data set and N is the number of data available.

There are many algorithms to minimise the error function generated by the network, the most popular being the backpropagation of errors and many others like the Levenberg-Marquads, Trust-region, Quasi-Newton, Conjugate gradient and Genetical algorithms [5].

Our ultimate aim is to predict the target value for a new test case $t^{(n+1)}$, not included in the training set, given the corresponding new input values $\vec{\imath}^{(n+1)}$. For good predictions, the neural network model has to generalise well, i.e. these predictions must neither 'overfit', see line (c) in Figure 2.3, nor 'underfit' the data, see line (a) in Figure 2.3. If the predictions overfit the data, the data used for training will be predicted well however this model will generalise poorly and the test data, as well as new data, will be poorly predicted. Obviously a model which 'underfits' the data is a bad model because it is incapable of representing the target values.
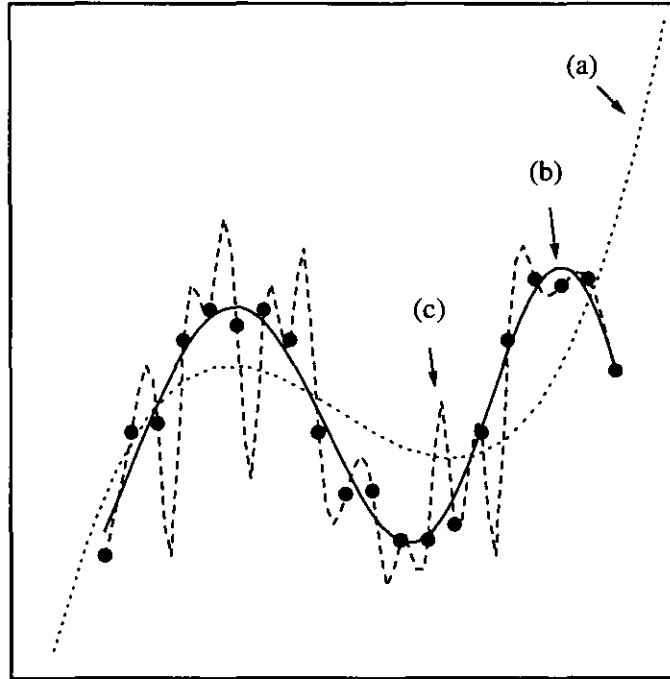
Figure 2.3: (a) the data are underfitted; (b) the model fits the data well (c) the data are overfitted.

The choice of neural network architecture is crucial to avoid overfitting. If there are too few hidden nodes the model might not be able to predict the test data, see (a) in Figure 2.4, even the training data will not be fitted well and hence the model will underfit the data. At the other extreme, if the number of hidden nodes, or non-linearity of the model, is too large, see line (c) in Figure 2.4, the training data will be very well predicted, decreasing the training error but increasing the test error.
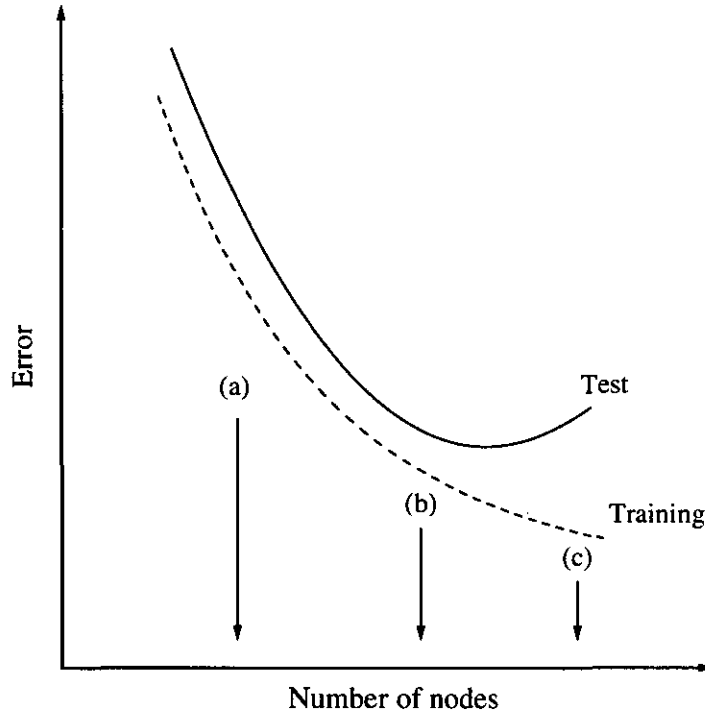
Figure 2.4: (a) this number of nodes in the model is not enough to represent the data; (b) correct choice of the number of nodes; (c) excessive number of nodes. (a), (b) and (c) corresponding with the fitted lines given in Figure 2.3 .

2.2.6 Bayesian neural networks

Bayesian ideas are based on a different view in which probability is used to represent uncertainty about the relationship being learned, in contrast with traditional methods. A traditional learning method, i.e. backpropagation of errors, gives one value for each parameter of the net, whereas Bayesian learning produces a probability distribution (posterior distribution) for a given parameter, see Figure 2.5. Mackay introduced the use of Bayesian statistics to neural networks, which successfully facilitated the training process, [11, 12, 13].
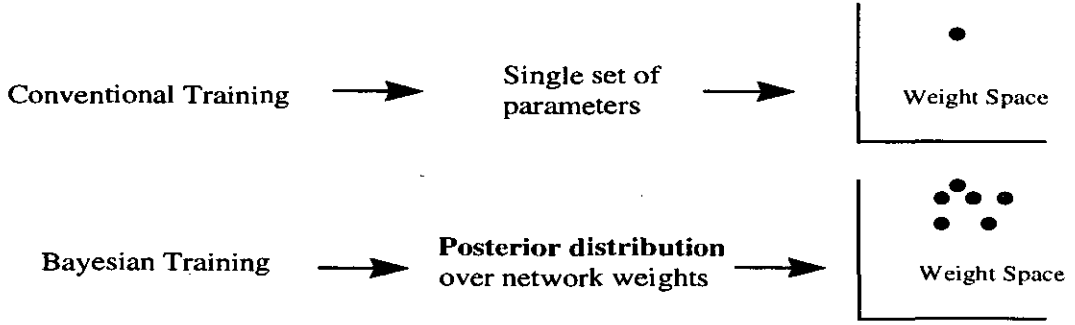
Figure 2.5: Conventional regression techniques gives one value for each parameter of the net, whereas Bayesian training produces a probability distribution on the weight space for each parameter.

In the same way as a learning process is started in a traditional way by giving random initial values for the parameters, in Bayesian learning a prior distribution, for the parameters might be specified, $P(\theta)$, where previous beliefs about their values can be introduced. This step is precisely one of the setbacks in Bayesian learning because it is not well understood how prior knowledge of the parameters affects the final model and usually the choice of a prior distribution is arbitrary. In addition, it may be useful to specify a joint prior distribution for the components of θ, using a common hyperparameter for weights in the same layer for example, γ, which is given its own prior, $P(\gamma)$. The priors are just a probability distribution on a particular region of the weight space, i.e. Gaussian distribution for the network parameters and Gamma distributions for the hyperparameters.

In the light of new data, the probability of network weights that do fit the data well will increase and the prior distribution, $P(\theta)$, will be updated to a posterior distribution, $P(\theta, \gamma | (\vec{i}^{(1)}, t^{(1)})...(\vec{i}^{(n)}, t^{(n)}))$, using Bayes' Rule.

$$P(\theta, \gamma | (\vec{i}^{(1)}, t^{(1)})...(\vec{i}^{(n)}, t^{(n)})) \propto P(\gamma)P(\theta|\gamma) \prod_{c=1}^{n} P(t^{(c)}|\vec{i}^{(c)}, \theta, \gamma) \qquad (2.6)$$

$P(A|B)$ is read as the probability of B given A, where $P(t^{(c)}|\vec{i}^{(c)}, \theta, \gamma)$ is the conditional distribution or probability densities for the target and $P(\theta|\gamma)$ is the prior density for the parameters.

The result of Bayesian training is a posterior distribution over network weights. If a prediction is made based on some new inputs, the posterior distribution over

network weights will give rise to a distribution over the outputs, which is now a predictive distribution for the new case. The predictive distribution for a new output value $t^{(n+1)}$, given the input $\vec{i}^{(n+1)}$ and the training data $(\vec{i}^{(1)}, t^{(1)})...(\vec{i}^{(n)}, t^{(n)})$, is given by:

$$P(t^{(n+1)}|\vec{i}^{(n+1)}, (\vec{i}^{(1)}, t^{(1)}), ..., (\vec{i}^{(n)}, t^{(n)})) =$$

$$\int P(t^{(n+1)}|\vec{i}^{(n+1)}, \theta, \gamma)P(\theta, \gamma|(\vec{i}^{(1)}, t^{(1)}), ..., (\vec{i}^{(n)}, t^{(n)}))d\theta d\gamma \qquad (2.7)$$

If a single-valued prediction is needed (example, for a regression model), the prediction that minimises the expected squared-error loss is the mean of the predictive distribution, $\hat{t}^{(n+1)}$. This optimal prediction is given by:

$$\hat{t}^{(n+1)} = \int o(\vec{i}^{(n+1)}, \theta)P(\theta, \gamma|(\vec{i}^{(1)}, t^{(1)}), ..., (\vec{i}^{(n)}, t^{(n)})d\theta d\gamma \qquad (2.8)$$

where $o(\vec{i}^{(n+1)}, \theta)$, is the output of the network defined by Equation 2.1.

2.2.7 Markov chain Monte Carlo methods

The evaluation of the integrals in Equation 2.7 and 2.8 are very complex because of the complexity of the posterior distribution due to the large quantity of variables involved. This is a major problem in Bayesian learning. There are two typical methods based on different approaches which can simplify the posterior distribution to make the integral easier: the evidence framework developed by Mackay [11, 12] and the Markov chain Monte Carlo method developed by Neal [14]. The evidence framework is based on the optimization of hyperparameters and the approximation of the previous integral by a Gaussian centred on the maximum for the posterior distribution and single-valued estimates for the hyperparameters. A C code implementing the MacKay framework for artificial neural networks can be found in [15]. However, there may be situations where these Gaussian assumptions are inaccurate [14]. A more precise method, but still an approximation, is the one based on sampling from the posterior, such as the Markov chain Monte Carlo method developed by Neal [14].

In this work, the Markov chain Monte Carlo method approach has been used to implement the Bayesian learning in the neural network model. The idea behind the sampling method is to approximate the integral in Equation 2.7 over a sum as follows:

$$P\left(t^{(n+1)}|\vec{i}^{(n+1)}, (\vec{i}^{(1)}, t^{(1)}), ..., (\vec{i}^{(n)}, t^{(n)})\right) =$$

$$\int P(t^{(n+1)}|\vec{i}^{(n+1)}, \theta, \gamma)P(\theta, \gamma|(\vec{i}^{(1)}, t^{(1)}), ..., (\vec{i}^{(n)}, t^{(n)}))d\theta d\gamma$$

$$\simeq \frac{1}{T}\sum_{t=1}^{T} P(t^{(n+1)}|\vec{i}^{(n+1)}, \theta^{(t)}, \gamma^{(t)}) \qquad (2.9)$$

17

where each t represents samples drawn from the posterior $P(\theta, \gamma | (\vec{i}^{(1)}, t^{(1)}), ..., (\vec{i}^{(n)}, t^{(n)}))$. Such a series of samples may be generated using a Markov Chain with the posterior as its stationary distribution. To estimate the predictive distribution, or a single valued prediction, with respect to the posterior distribution, the Markov Chain must have a unique equilibrium distribution, i.e. the posterior, which converges as rapidly as possible leaving the posterior distribution invariant [14].

In Neal's work, a Markov chain that explores the entire posterior distribution is obtained by alternating Gibbs sampling, known as the 'heatbath' method, updates for the hyperparameters γ, with hybrid Monte Carlo [16] updates for the network parameters θ. This helps to explore weight space efficiently. An example of Monte Carlo Implementation of Bayesian Learning on neural networks is explained in detail by Neal and Rasmussen [14, 17, 18]. The implementation for neural networks of the algorithms used in this work can be found in the C code written by Neal [19].

2.2.8 Optimal architecture and input relevance

There is no way to determine a good network architecture simply from the number of inputs and outputs. It depends critically on the number of training cases, the amount of noise on the data, and the complexity of the function the neural network is trying to learn. Trial and error seems to be the best way to get a good network architecture, systematically trying many networks with different numbers of hidden units, estimating the sum squared error for each network, and choosing the one with best average sum squared error performance, i.e. the minimum generalization (test) error. Bayesian learning is supposed to be a good learning method that generalises well, see Figure 2.3.

A great variety of methods have been proposed to measure the importance of inputs. The main conclusion is that there is no single measure of importance that is appropriate for all applications [5]. In a straightforward linear model, i.e. a neural network without hidden units, each weight is the change in the output associated with a unit change in the corresponding input, assuming all other inputs are held fixed. However, this interpretation depends on whether one input can change independently of the other inputs. If the inputs include characteristics that one external operator cannot control and that are not independent, the interpretation has no base. Comparing weights in a neural network is more problematic than comparing weights in linear models, because now the simple interpretation does not exist due to the hidden layer.

Neal's code implements the idea of Automatic Relevance Determination, ARD. This idea is based on a hierarchical choice of hyperparameters controlling different

18

groups of weights, i.e. input-hidden layer, input-output and hidden-output connections. If one input is irrelevant the hyperparameter grows and forces the associated parameters to vanish (it is necessary to scale the inputs so that a one-unit change has similar significance for each of them). This idea is called automatic relevance determination ARD, and was introduced by Mackay and Neal [14]. Then, by comparing the values of the hyperparameters which control the weights outwards in each input, it would be possible to get an idea of the important inputs. However, it is still not clear how good this measure is and how to interpret it in an architecture with input-hidden and input-output connections.

In this work a measure of 'importance' has been taking into account by manipulating the values of the inputs, and then studying how much the outputs will change. A way to measure the input relevances based on differences is used in this thesis. Only one input will be varied at a time in order to study the effect on the output, the remaining inputs being kept constant. The effect of equal variation in the inputs allows us to compare between inputs in the light of the output variation because the data are normalised.

2.2.9 Network training method details

This is a typical example of a run used with Neal's code [19] for a given architecture

```
net-spec c-ce1-log.net 5 1 1 / - 0.05:0.5:1 0.1:0.5 -x0.1:0.5 0.05:0.5:1 1
model-spec c-ce1-log.net real 0.05:0.5
data-spec c-ce1-log.net 5 1 / c-c.dat@1:144 . c-c.dat@145:288 .
net-gen c-ce1-log.net fix 0.5
mc-spec c-ce1-log.net repeat 10 sample-noise heatbath hybrid 100:10 0.2
net-mc c-ce1-log.net 1
mc-spec c-ce1-log.net sample-sigmas heatbath hybrid 1000:10 0.4
net-mc c-ce1-log.net 100
```

The first command of the run, 'net-spec', creates a 'log' file containing the specifications for the network architecture and the priors to use for the network parameters. Once the network has been specified, the 'model-spec' command specifies how the network outputs will be used to model the targets; in this case the targets are real-valued and modelled as the network output plus a Gaussian noise. The data sets used for training and for testing have to be specified with the 'data-spec' command. The next three commands, 'net-gen', 'mc-spec' and 'net-mc' start the simulation with a short initial phase where the hyperparameters and parameters take on moderate, not extreme, values. The most important and final part of the run is the sampling

19

phase which is specified by the last two commands 'mc-spec' and 'net-mc'. The first command of the sampling phase, 'mc-spec', appends a new set of Markov chain operations to the 'log' file. These operations are Gibbs samples for both hyperparameters and parameters. The iterations of the sampling phase started with the last command, 'net-mc' [19].

The architecture used is the same as that one represented by Equation 2.1. Only one hidden layer has been used for simplicity. The success of networks with this architecture is demonstrated in Chapter 3. The above example of a run is for a given architecture with 5 inputs, 1 hidden unit and 1 output, used in Chapter 3 for the prediction of weld metal chemistry. However, in this work the behaviour associated with using 1 to 10 hidden units in the hidden layer has been analysed for each output predicted. The one with the best performance based on the average sum squared error consideration of the test data will be chosen.

The parameters have been divided into 5 groups: input-hidden weights, hidden biases, hidden-output weights, input-output weights and output biases. It is necessary to specify a prior distribution for each group and for the noise expected on the data. After many attempts based on trial and error, it is concluded that the choice of these priors is not crucial to the results providing that extreme values are not selected; if sensible values are chosen, the training process will be able to achieve the required parameters by inferring them from the data. These values have been chosen based on experience. The noise is supposed to be drawn from a Gaussian distribution with variance σ^2 or precision $\tau = \sigma^{-2}$. Then a 'vague' gamma probability, $p(\tau)$, is given to the precision allowing it to vary in a wide range. The gamma probability is given by

$$p(\tau) \propto \tau^{\frac{\alpha}{2}-1} \exp(-\tau\alpha/2\mu) \qquad (2.10)$$

and the values selected are $\sigma = 0.05$ and $\alpha = 0.5$, where α is the shape parameter.

For the input-hidden weights a three layer prior is given, that is to say, one more parameter than the prior which was used for the noise, which is in a higher status. Each weight is given a zero-mean Gaussian distribution of variance σ^2 being this variance controlled by a Gamma distribution as in Equation 2.10. The parameters used are $\sigma = 0.05$, $\alpha_0 = 0.5$ and $\alpha_1 = 1$. The same prior is given to the input-output weights.

The hidden-output prior is given a two layer prior, with parameters $\alpha = 0.5$ and $\sigma = 0.1$, but scaling the variance to the number of hidden units, following [14].

The output-biases are given zero-mean Gaussian priors with a standard deviation of $\sigma = 1$. The hidden-biases group is given a prior consisting of two hierarchical layers, given by a gamma distribution with $\sigma = 0.1$ and $\alpha_0 = 0.5$.

The network training begins with a short initial phase where the hyperparameters are kept constant at 0.5, allowing the weights to grow during 100 leapfrogs (finite time steps). The short initial phase is followed by a long sampling phase, then the simulation is brought to equilibrium and a sample of 100 networks is produced from the posterior for use in prediction after Monte Carlo updates of 1000 leapfrogs.

In general it is very difficult to know when a Monte Carlo chain has reached equilibrium, i.e. when the algorithm reaches regions of high posterior probability. An approximate way to guess when the chain has reached equilibrium is by plotting the training and test sum average squared error.
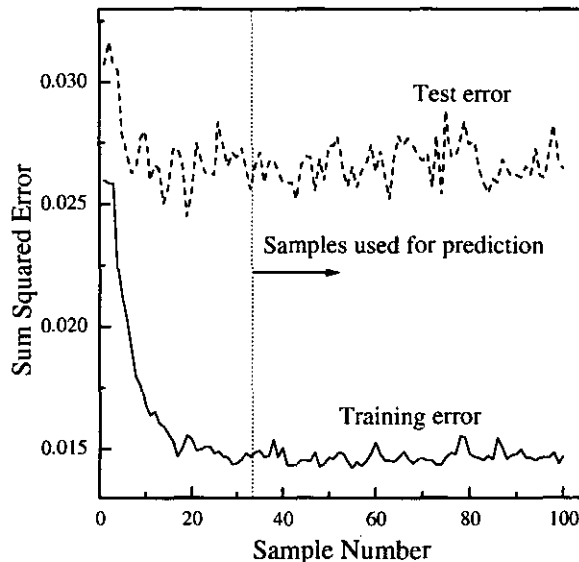
Figure 2.6: Sum Squared Error evolution during the sampling phase

In most of the simulation in this work the training and test errors show the behaviour presented in Figure 2.6, during the sample phase. In this example the initial 30 nets can be discarded and the remaining 70 networks (70 different sets of weights), can be used to make predictions. A single valued prediction will be the mean of the 70 guesses with the error as the standard deviation error. The command to make prediction in Neals' program is 'net-pred', where it has to be specified, the 'log' file (with all the information), the input data for prediction and how many samples are going to be used need to be specified.

An error bar for each value predicted can be obtained from the predictions of the networks from the Monte Carlo chain. It is also possible to obtain from them the standard deviation for each value. The standard error deviation is given by

$$sd = \sqrt{\frac{\sum(t - o)^2}{N - 1}} \qquad (2.11)$$

where o is the mean value predicted, t is the 'real' value from the database and N the number of predictions, in this case 70.

2.2.10 Summary

The characteristics of the neural network models employed in this thesis have been reviewed. Feed-forward neural network models with one hidden layer are employed. The data used to feed the network are normalised and scaled in the range where the transfer function, i.e. hyperbolic tangent, varies the most. The number of inputs and hidden nodes depend on the particular output to be predicted. Several networks with increasing numbers of hidden nodes, i.e. from 1 to 10, and different choices of input variables are tested and the one with least error in the prediction of the test data is chosen. Predictions and their errors are calculated as the average of the latter samples of the Monte Carlo chain which are in equilibrium, i.e. typically 70 samples. The relative importance of the inputs in the prediction of the output is measured by a simple difference method.

2.3 Molecular dynamics

2.3.1 Introduction

Molecular dynamics is a computer technique that solves Newton's equations for a system of particles. The full set of classical equations of motion are simultaneously solved for all the particles in the system. Molecular dynamics simulations (MD) also provides the whole dynamics of the process studied, allowing one to follow the trajectory of any particle in the real space. Molecular Dynamics is an ideal simulation method when the dynamical properties of a many-particle system are required [20]. Molecular dynamics have been widely used for the simulation of radiation damage in solids, where many-body interactions are of great importance for the accurate description of the process.

Models based on the binary collision approximation (BCA), are also extensively used in radiation damage studies. In the BCA the trajectories of energetic particles

are represented as a series of two-body encounters in which the other particles do not take part. The binary crystal model (BC) and Monte Carlo models (MC) are two types BCA models. The BC model assigns atoms with well-defined initial positions and the collision parameters are calculated from them in a geometrical manner. On the other hand MC models commonly use aleatory methods to locate atoms and calculate the collision parameters. These methods based on the binary collision approximation have been extensively used in the interaction of ions with solid surfaces. For a review of them see [21].

In this thesis classical MD simulations have been chosen to analyse the structure of grain boundaries and the effect of collision cascades near them. The intrinsic many-body interaction nature of a collision process in a system with many particles is completely described by MD simulations.

2.3.2 Equations of motion

Classical molecular dynamics assumes that the particles of the system move according to the classical Newton's equations of motion. Given a system of N particles the equations of motion can be written as follows:

$$
\frac{d\vec{r}_i}{dt} = \vec{v}_i
$$
$$
m_i \frac{d\vec{v}_i}{dt} = m_i \vec{a}_i = \vec{F}_i \tag{2.12}
$$

where $\vec{r}_i$, $\vec{v}_i$, $\vec{a}_i$, m_i and $\vec{F}_i$ are the position, velocity, acceleration, mass and force respectively, associated to each particle i. It is usually assumed that the forces between particles can be derived from a potential only dependent on the positions of the particles. In this case the force on a particle i, $\vec{F}_i$, is given by the differential of the potential energy function, V, with respect to the position of the considered particle as follows:

$$
\vec{F}_i = -\nabla^i V \tag{2.13}
$$

Once the potential energy function of the system is known, the equations of motion can be simultaneously solved for all the particles on the system.

2.3.3 The Verlet algorithm

Solving the equations of motion is a means to obtain, given the particle positions, velocities and forces at time t, the positions velocities and accelerations at a later time $t + \Delta t$. The standard numerical solution of the equations of motion is obtained by a finite difference approach where the time is discretised. A numerical algorithm is needed to solve the equations of motion. There are several integration methods which can provide different levels of accuracy on the calculation. In molecular dynamics simulations the accuracy of the integration algorithm is always in compromise with the speed of the calculation.

One of the most popular integration algorithms is the Verlet algorithm [22]. The Verlet algorithm is derivable from a Taylor series expansion and it is of second order accuracy for positions and velocities. The Verlet algorithm can be expressed as follows:

$$\vec{r}_{n+1} = \vec{r}_n + \vec{v}_n \Delta t_n + \frac{1}{2}\vec{a}_n \Delta t_n^2 + \theta(\Delta t_n)^3$$

$$\vec{v}_{n+1} = \vec{v}_n + \frac{1}{2}(\vec{a}_{n+1} + \vec{a}_n)\Delta t_n + \theta(\Delta t_n)^3 \tag{2.14}$$

where $\vec{r}$, $\vec{v}$ and $\vec{a}$ are the position, velocity and acceleration of a given particle. Subscripts indicate the time step number at which the values are calculated. Δt is the time step length.

As it can be seen from the previous equation positions of the particles at time step $n + 1$ are obtained using the positions, velocities and accelerations associated to the particle in the previous step. After obtaining the new positions of the particles the accelerations and forces at the new time step can be also calculated, because the potential only depends on the positions of the particles. Accelerations at the new time step are required to calculate the velocities as is indicated by Equations 2.14. This algorithm has been proved to be of great accuracy, however, because this algorithm is of order 2 only small time steps can be used, i.e. the order of femtoseconds. The Verlet algorithm is also symplectic, which means that it preserves all the Hamiltonian invariants, i.e. energy, to the numerical accuracy employed. As such the method preserves energy better than many higher order methods.

Higher order integration methods can be derived by truncating the Taylor expansion to greater powers of the time step. One example of this higher order methods is the third-order, two-step method of Smith and Harrison [23]. This higher order method calculates higher derivatives of the forces and increases the storage requirements. It might appear that this could be compensated by the fact that the time step can be increased without losing accuracy however, often empirical potentials

have discontinuities in the higher derivatives and in such cases higher order methods which attempt to approximate these derivatives numerically can be inaccurate. Thus low order methods are preferred.

Better accuracy of the trajectories is needed when the particles suffer big changes in their position during small times. This is the typical situation of a collision cascade simulation where collisions involve close interaction with big repulsion forces. A good algorithm is needed to keep accuracy in these cases but also, a good choice of the time step. This time step can be automatically adjusted in the simulation in order to optimise accuracy and speed of the simulation [23, 24, 25]. Accuracy of the simulations can be estimated by monitoring the total energy conservation of the system.

This thesis uses the Verlet algorithm for the integration of the equation of motion. Accuracy is optimised in this thesis by setting up different time steps depending on the stage of the simulation. In the first instants of the simulation, when close interactions i.e. collisions, are more frequent and strong repulsive forces appear, the time step is reduced typically to the tenth of femtosecond to keep accuracy. During the simulation the time step is gradually increased until a maximum value of typically 2 fs, which happens when the system is close to its relaxed state and no close interactions occur.

2.3.4 Boundary conditions

Molecular dynamics simulations start from a predefined arrangement of particles. The initial positions of every particle involved in the simulations has to be specified. If the system has a crystal structure this arrangement can be very easily coded by repetition and translations of the basic unit cell until the required size of the system is reached. A three-dimensional rectangular box is usually the shape of the system which is simulated. The finite size of the system to be simulated will depend on the computational resources available. Systems up to 10^8 atoms have been simulated in parallel computer systems, this gives systems of the order of nm.

Possible edge effects can be of great importance when the size of the system to be simulated is under consideration. Edge effects are caused by atoms at the boundaries of the computational cell. These atoms are not surrounded by the same crystallographic atomic configuration as an atom in the bulk. The behaviour of this atoms will be completely different compared with those in the bulk. Therefore, if the phenomenon which is simulated takes place in the bulk of the material the size of

the computational cell have to be big enough in order to avoid the interaction of the boundaries with the region of interest.

Depending on the purpose of the simulation and how the edge effects can affect it, different boundary conditions can be applied. Free and periodic boundary conditions are commonly used in MD simulations [20]. Free boundary conditions are applied when there are no restrictions of mobility for the particles and they can move beyond the initial limits of the computational cell. Free boundary conditions as well as fixed boundaries can clearly provoke edge effects in small systems. On the other hand, periodic boundary conditions are usually applied to avoid this edge effects. Periodic boundary conditions basically means that if a particle reaches a boundary then automatically enters the computational cell on the other side of the cell, simulating in this way a quasi-infinite system. For example, if a particle moves to the coordinate $lx+a$, being lx the dimension of the cell in the x dimension, the new coordinate of the particle will be a. Periodic boundary conditions make no sense if the surroundings which the particle finds when is reallocated are different from the ones on the other side of the cell. The previous fact imposes a restriction on choice of the size of the computational cell, being that any dimension where boundary conditions are applied has to be an integer number times the length of the greatest symmetry periods in this direction.

Free boundary conditions are usually preferred to periodic boundary conditions in simulations of high-energy atomic collision events, because it is preferable that energetic particles leave the simulation cell than reappear on the opposite side [25]. However, large enough system will be always preferable whatever type of boundary conditions are used in order to minimise the boundary effects.

In this thesis, rectangular computational blocks are employed. This computational blocks have two different orientated bicrystals forming a symmetrical interface in the middle of the system. Periodic boundary conditions parallel to the interface and free boundary conditions on the dimension perpendicular to the boundary are applied as it will be explained in Chapter 4. The size of the blocks considered are big enough to contain the collision cascades studied avoiding interactions with the boundaries. The number of atoms which are contained in the simulation box depends on the model of the boundary being use, but is typically 40,000 atoms.

2.3.5 Neighbour lists

The evaluation of forces is the most computationally expensive step in molecular dynamics simulations. Force evaluations can take up to 90% of CPU time during a single simulation [24]. A good optimised code has to be well tuned in force calculations.

Most commonly the potentials used in simulations are short ranged potentials. For these potentials it is inefficient to examine all the interactions because, clearly, only atoms between a distance smaller than the potential cut-off distance will contribute to the forces. Methods to avoid this situation are based on the generation of neighbour lists.

A neighbour list is generated for every atom and it contains all the atoms in a sphere of radius r_o which is slightly larger than the cut off r_c distance of the potential. In this way the code only goes over the atoms on the neighbour list calculating the forces for those ones within a distance less than the cut off distance. These neighbour lists can be updated every time step, however by choosing a radius r_o bigger than the cut off radius the frequency at which the neighbour lists are updated decreases. The neighbour lists are usually updated when the value of an accumulator, which is made by adding the two largest displacements suffer by the particles at every time step, is bigger than the difference between the outer and the cut off radius, $r_o - r_c$.

Updating neighbour lists can be time consuming because of the distance checking and some methods have been proposed to optimise it. The coarse grained cell or linked list method [26] has been shown to be faster for system sizes usually employed in molecular dynamics simulations, than other methods like the Verlet method and the method of lights [24, 25]. The linked list method divides the simulation region into a set of cubic regions with sides bigger than the outer radius then a cell list is generated by sorting all the atoms in their cells. Therefore for each atom, all its possible neighbours are in its own cell or any of the 26 neighbour cells that surround it. The algorithm will only consider atoms in neighbour cells for updating the neighbours within a distance of r_o.

In this thesis, neighbour lists updated with a linked list method are used.

2.3.6 Statistics

Enough simulations, must be generated in molecular dynamics simulations to obtain reliable quantities of the physical properties studied and give meaningful comparisons with experiments. Different simulation of the same phenomenon, are obtained by changing the initial conditions of the system without changing the physical nature of

the process to be studied. In radiation damage simulations, for example, statistics can be generated by changing the velocity direction of the primary knock-on atom.

When generating statistics, it has to be taken into account, that the same simulation can give different results on different computers. This is due to the different optimisation of the code in different architectures, rounding errors and the inherent chaos of many Hamiltonian systems.

2.3.7 Interatomic potentials

Atomistic modelling of materials are based on the knowledge of the interatomic energy potential function. A requirement for good model of a material, i.e. the interatomic potential, is that it has to be accurate enough to permit the modelling of a broad range of experiments [27]. The complexity of the model has to be in accordance with the computer resources available which permit a simulation of a experiment between certain limits of computing time. For a reliable model in the case of metals, it has to be fitted or reproduce parameters like the lattice constant in its stable configuration, heat of sublimation, vacancy and interstitial formation energies and for cubic metals reproduce the elastic constants.

Pair potentials

Modelling of metallic systems was initiated with the use of the so called pair potentials or semiempirical potentials. This pair interatomic potentials give the total energy per atom, u_p, as a sum of independent pair interactions functions, V, as follows

$$u_p = \frac{1}{2} \sum_j V(x_j) \qquad (2.15)$$

where the sums extend over all neighbours j at distance x_j, V represents the (repulsive) interaction between ions, and the 1/2 factor is because the energy of each bond can be thought of as being equally divided between both particles. The Lennard-Jones and Morse potentials are two typical examples of this pair potentials.

Pair potentials have many setbacks when used to model metallic systems. Pair potentials cannot reproduce the Cauchy relation between the elastic constants in cubic crystals. They cannot accurately reproduce the cohesive energy and the vacancy formation energy. If one of them is fitted the other one wrongly predicted by the model. Also, pair potentials result in surface relaxations which are always outward. This is basically due to the linear dependence of the cohesive energy per atom on the local coordination number, contrary to the observed non-linear dependence [28].

Many-body potentials

To overcome some of these problems a series of interatomic potentials for metallic systems have been developed since the 1980s. These interatomic potentials which include methods like the embedded-atom method [29], Finnis-Sinclair N-body potentials [30, 31] and the glue model [32], are generally referred as a many-body potentials or pair-functional methods. In these potentials a density-dependent term, the so-called embedding function is added as a functional associated with the local environment of a particular atom.

The energy per atom in a crystal (the cohesive energy), u_t, is given by the many-body potentials as the sum of pairwise, u_p, and many-body terms, u_n, thus:

$$u_t = u_n + u_p \tag{2.16}$$

where u_p is given by equation 2.15 and u_n is as follows

$$u_n = F(\rho) \tag{2.17}$$

$$\rho = \sum_j \Phi(x_j) \tag{2.18}$$

where the sums extend over all neighbours j at distance x_j. This many-body part of the potential has different interpretations in the embedded atom method developed by Daw and Baskes and the Finnis-Sinclair N-body potential. In the embedded atom method, based in the density functional theory, the function ρ gives a measure of the local electron density at a site due to the linear superposition of electronic densities of neighbouring atoms, $\Phi(x_j)$. The embedding function F is the energy associated with placing an atom in that electronic density. The Finnis-Sinclair interpretation is based on second momentum approximations of tight-binding theory. As a result, Finnis and Sinclair take $F(\rho)$ as proportional to the square root of ρ

$$u_n = -A(\rho)^{\frac{1}{2}} \tag{2.19}$$

being A a proportionality constant which depends on the material.

The many-body potentials have also serious limitations when modelling metallic systems [33]. The main setback is that these potentials are more suitable for metals with completely empty or filled bands. Partial filling of the d bands, i.e. transition metals, implies an angular character of the interactions between atoms in the material which this form of the many-body potentials cannot represent. Some efforts have

been done to incorporate the angular nature of the bonding to metallic intaratomic potentials by including higher-order moments of the density of states of the tight binding theory [34, 35].

In particular, two main approximations are involved in the use of a many-body potential when dealing with interfaces: Firstly, no directional bonding between atoms on the crystal is assumed, because of the isotropic nature of the many-body potential, which is a clear approximation for a transition metal. Secondly, the validity of the many-body potential is assumed on the interface. Atoms interacting across the interface experience an electron density different from atoms interacting in the perfect crystal structure of the bulk. The isotropic nature of the many-body potentials does not take into account the previous fact, however their use can be justified by considering that the change of the electronic density near the interface is small compared with the crystal bulk [36].

2.3.8 Calder and Bacon potential

In order to represent the interaction between iron atoms, a many-body potential for α-iron has been used [37] in this work. This potential has the Finnis-Sinclair form [30] with modifications on the ion-ion repulsive part in order to give a good description of the collision event at high energies [37], which will be of importance in Chapter 5 of this thesis.

The many-body part of the potentials given by the cohesive part of the Finnis-Sinclair potential [30, 31] and is defined as:

$$
\Phi(x) = 0.582674 \text{ Å}^2, \qquad \text{if } x \leq 2.2476 \text{ Å}
$$
$$
\Phi(x) = (x - d)^2 + \frac{\beta(x - d)^3}{d}, \qquad \text{if } 2.2476\text{Å} < x \leq d
$$
$$
\Phi(x) = 0, \qquad \text{if } x > d \tag{2.20}
$$

The parameters involved in the previous equation are given in Table 2.1

d(Å)	A(eVÅ^{-1})	β	c(Å)	c_0(eV)	c_1(eVÅ^{-1})	c_2(eVÅ^{-2})
3.569745	1.828905	1.8	3.4	1.2371147	−0.3592185	−0.0385607

Table 2.1: Parameters for α-iron in the Finnis-Sinclair potential.

There exist different choices of this parameters which can reproduce all the properties fitted in the Finnis-Sinclair potential [38].

According to the distance between ions, x, the repulsive part of the many-body potential, $V(x)$, is described in four different parts as follows:

1) The repulsive part of the Finnis-Sinclair potential for $x \geq 2.4507$ Å , given by:

$$V(x) = (x - c)^2(c_0 + c_1 x + c_2 x^2), \qquad \text{if } x \leq c$$
$$V(x) = 0, \qquad \text{if } x > c \tag{2.21}$$

where the parameters are given in Table 2.1.

2) A Born-Mayer type potential for 0.62 Å$\leq x \prec 2.4507$ Å, given by:

$$V(x) = 7069.7203 \exp(-4.3991821 x) \tag{2.22}$$

3) An exponential type potential for 0.305 Å$\leq x < 0.62$ Å, given by:

$$V(x) = \exp(9.7262382 + 1.8058868 x - 26.7488847 x^2 + 23.3815021 x^3) \tag{2.23}$$

4) The Ziegler, Biersack and Litmark's universal potential (ZBL), [39], for $x \leq 0.305$ Å, given by:

$$V(x) = \frac{Z_1 Z_2 e^2}{4\pi\varepsilon_0 x} \Theta(X) \tag{2.24}$$

with

$$\Theta(X) = 0.18175 \exp(-3.1998 X) + 0.50986 \exp(-0.94229 X) +$$
$$+ 0.28022 \exp(-0.40290 X) + 0.028171 \exp(-0.20162 X) \tag{2.25}$$

where

$$X = \frac{x}{a}$$
$$a = \frac{0.88534 a_B}{(Z_1^{0.23} + Z_2^{0.23})} \text{ (if } Z_1 = Z_2 \text{ then } a = \frac{0.44267 a_B}{Z^{0.23}})$$
$$a_B = 0.530\text{Å}$$
$$\frac{e^2}{4\pi\varepsilon_0} = \frac{2.3070796 \times 10^{-28}}{10^{-10} \times 1.60217733 \times 10^{-19}} \text{ (in Å and eV)} \tag{2.26}$$

being e the electronic charge and ε_0 the permittivity of free space.

It was noticed that this parameterisation of the potential was slightly discontinuous between the Born-Mayer and the Finnis-Sinclair part of the potential. The joint point between these two potential parts was moved to 2.4507 Å, from the original 2.35053 Å. At this distance the potential derivative is continuous between both parts. In addition an almost negligible term, -0.03416 eV, was added to the ZBL, exponential and Born-Mayer parts of the potential to make the potential continuous. This potential give us a minimum of the potential energy per atom (cohesive energy) for a lattice constant equals 2.8665 Å, being the energy -4.28 eV, see Figure 2.7.
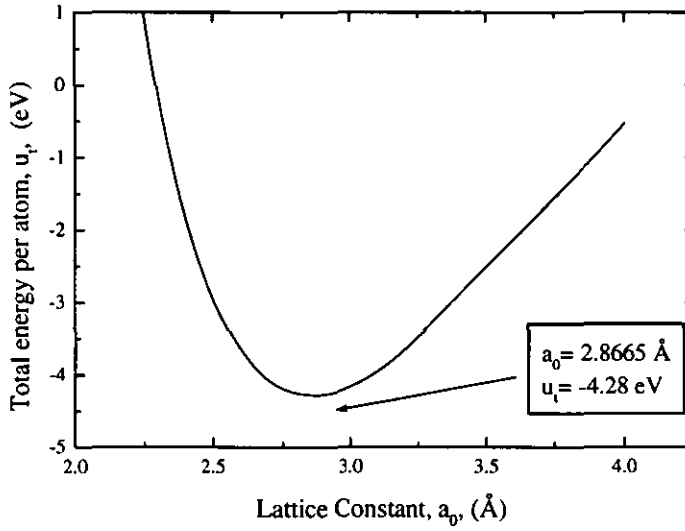
Figure 2.7: Cohesive energy of the Finnis-Sinclair potential as a function of the lattice constant in a iron bcc lattice.

2.3.9 Summary

The main characteristics of the molecular dynamics technique used in this thesis have been reviewed. The technique is applied to rectangular computational blocks which contain a symmetrical planar interface, i.e. grain boundary, between two bicrystals of α-iron. Periodic boundary conditions are applied to the plane parallel to the interface, with free boundaries used in the direction perpendicular to the interface. A many-body interatomic potential of the Finnis-Sinclair form has been used to represent the interaction between iron atoms. Molecular dynamics is used to calculate relaxed structures of the interfaces and to simulate collision cascades near the boundaries.

2.4 Computing

The implementation for neural networks of the Markov chain Monte Carlo methods used in this work can be found in the C code written by Radford Neal [19]. The molecular dynamics code used in this thesis has been developed at Loughborough University and is written in FORTRAN code. This code has been optimised for its use with many-body, short-ranged potentials and system sizes of around 100,000 atoms [24]. The code implements in Fortran code all the previous considerations for a optimised molecular dynamics simulation. This code has been adapted to the simulation purposes of this thesis with some additions and minor changes have been done. The main addition is a new subroutine which generates the initial computational block including a symmetrical tilt or twist boundaries between two bcc bicrystals with the desired misorientation, as it will be explained in Chapter 4.

All the simulations have been mainly performed at the SUN UNIX workstations of Loughborough University. The configurations of this workstations are typically between 128-512 MB of RAM, 143-333 MHz, and they are running the 'Solaris 2.x' operating system. Also the Silicon Graphics Origin 2000 processors placed in the computing facilities of Manchester University have been used.

The images showing different instants of the simulation have been obtained by using the UNIX based package 'Rayshade' [40]. Also movies from the molecular dynamics simulations have been done in MPEG format. The analysis and graphs of data have been made in its major part using the PC based package 'Microcal Origin' version 5 [41].

Chapter 3

The prediction of weld metal chemistry and mechanical properties

3.1 Introduction

Weld metal chemistry and toughness are focus of this work. Attempts to calculate from first principles the final weld chemistry from the various reactions occurring in a weld pool and the final physical and mechanical properties of the weld in the case of submerged arc welding have not been very successful to date. It is very difficult to determine what is happening in the pool due to the great variety of complex processes which may occur.

Extensive analyses have been carried out concerned in this work with the prediction of weld metal chemistry and toughness using neural network techniques. A large, valuable, database, compiled over a number of years, provided by British Steel was used for the predictions. Neural network techniques based on a Bayesian framework which allows the net to learn from data in order to generalise properly for the prediction of outputs for previously unseen data were used. The implementation of the Bayesian learning in these neural network techniques is based on Markov chain Monte Carlo methods as explained in Chapter 2.

Weld metal chemistry predictions have been made for 17 elements. It was found that the non-linear regression models generated by the neural network gave a slight improvement compared to simple linear regression for most of the elements considered. The importance of each input in the prediction of the weld metal composition has also been studied - it is found that the plate and wire chemistries dominate in the prediction of the weld metal chemistry in line with known metallurgical experience. Neural network models have also been generated to enable prediction of weld

metal toughness, a complex mechanical property. Neural networks present a clear improvement, with respect to linear models for the prediction of weld metal toughness, showing the intrinsic non-linearity of the relation between toughness, weld metal chemistry, temperature and microstructure.

3.2   Submerged arc welding processes

In general, an arc welding process occurs when two pieces of metal are joined in the presence of an electric arc. The general configuration of a typical arc welding system can be: a power source, which generates the arc between the electrode (wire) and the workpiece (plate) and a shielding system which is used to protect the molten weld from the air [42]. Submerged arc welding processes are usually operated with a single wire, although a common variant is the use of multiple wires. A shielding gas is not required for submerged arc welding processes, instead, prior to welding, a thin layer of flux powder is placed on the workpiece surface. These fluxes are formulated to be compatible with a given electrode wire so that the combination of flux and wire yields the desired mechanical properties through the optimization of weld metal composition. Submerged arc welding processes are suited for longitudinal and circumferential butt and fillet welds. Depending on material thickness, either single-pass, two-pass or multipass weld procedures can be carried out. - the experimental database used in this work used three wires. A schematic diagram of the submerged arc welding process is given in Figure 3.1.

The electric arc formed between the workpiece and the electrode creates a plasma consisting of ionized atoms and free electrons. The heat generated is carried from the plasma to the workpiece and melting occurs. A weld pool is thus created composed of the material from the workpiece and drops of liquid (consumable or filler material) which are produced by the effect of the heat on the electrode.

The complex dynamics of the submerged arc welding process that uses a filler wire and flux shield are shown schematically in Figure 3.2. Several complex reactions are produced and various reaction zones may be considered: around the droplet at the electrode tip, around the droplet during flight, under the arc root at the weld pool surface (hot zone), and the weld pool surface away from the arc root (cold zone) and in the weld pool itself.
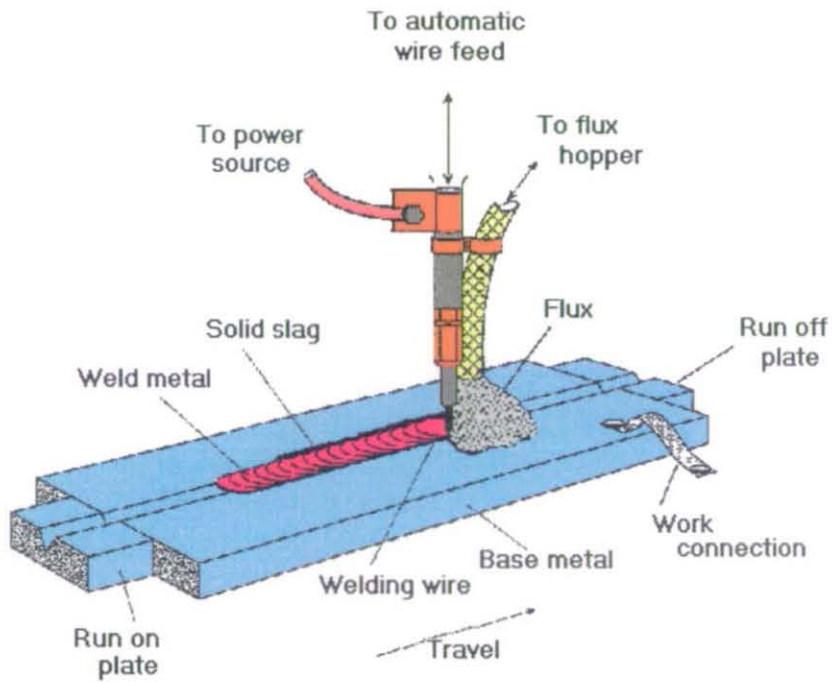
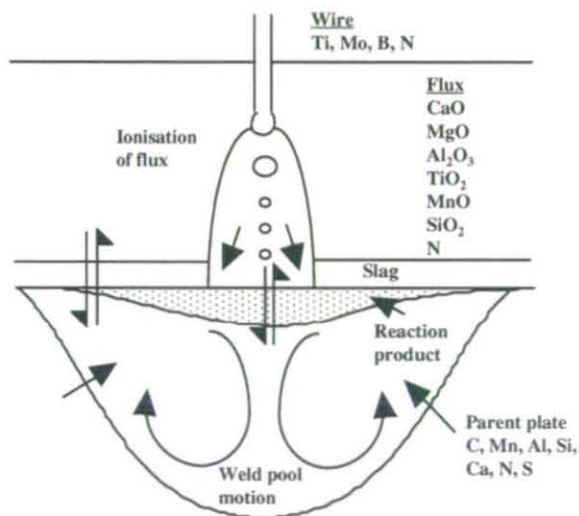Figure 3.1: General configuration of a typical welding system.

Figure 3.2: Submerged arc welding process dynamics in the weld pool.

3.3 Predicting weld metal chemistry

3.3.1 Introduction

In seam welding of linepipe the choice of base plate and consumable chemistry, together with welding parameters, to meet the required mechanical property specifications is often based on previous experience. The ability to predict weld metal chemistry is extremely important because the properties of a weld are determined primarily by its chemical composition and cooling rate. Microstructure prediction models, and ultimately mechanical property prediction models, both require weld metal chemistry as their starting point.

There have been a number of experimental investigations of the various interactions between wire, plate and flux during submerged arc welding processes, see for example [43, 44, 45, 46, 47, 48]. However, attempts to calculate from first principles the final weld chemistry from the various reactions occurring in the weld pool, and hence the final physical and mechanical properties of the weld, in the case of submerged arc welding [49, 50, 51] have met with limited success to date. It is very difficult to determine what is happening in the pool due to the very rapid temperature cycles to very high temperatures during the welding process. In addition, reactions are unlikely to reach equilibrium given the short times available during the welding process and the effect of process variables on the extent of reaction is complex.

Thier and Killing [50] eloquently simplify the problem by assuming that the chemical composition of the welding electrode can be changed in three specific zones during the welding process.

(1) The 'droplet' reaction: in which all metallurgical reactions are included from the welding electrode just prior to the droplet entering the liquid metal pool, expressed as:

$$x_D = x_E + \Delta x_{DR} \qquad (3.1)$$

where x_D is the concentration of the element x in the droplet at the point of entry into the weld pool, x_E is the concentration of the element x in the electrode and Δx_{DR} is the change in concentration of element x as a result of any chemical reaction.

(2) Dilution: in the second zone the droplet is mixed with the molten base metal, the degree of dilution, D, being given by:

$$D = \frac{Area\ of\ plate\ melted}{Area\ of\ weld\ bead} \qquad (3.2)$$

37

with the chemical composition of the liquid pool, x_P, being given by:

$$x_P = (1 - D)(x_E + \Delta x_{DR}) + Dx_B \qquad (3.3)$$

where x_B is the composition of the base plate.

(3) Reaction of the liquid metal with the molten slag, giving the final composition of the solidifying weld, x_W, as:

$$x_W = (1 - D)(x_E + \Delta x_{DR}) + Dx_B + \Delta x_{BR} \qquad (3.4)$$

where Δx_{BR} is the change in concentration of the element x on reaction with the molten slag.

These expressions require extension for the case of a multipass weld, in which the degree of dilution will vary as a function of position of an individual bead within the weld, with some beads being a simple function of only the wire chemistry.

In order to be able to predict the final composition of the weld, a detailed knowledge of the extent of chemical reaction in the various zones would be required. Thier and Killing [50] demonstrate that this is possible with reference to data available in the literature for specific fluxes, however Δx values are not generally available for all elements of interest.

More recent work [51] has proposed that chemical interaction between the slag and metal occurs in three stages: (i) droplet reactions, (ii) dilution and weld pool reactions and (iii) the zone of cooling and the solidifying weld pool. These authors propose that oxygen transfer primarily occurs in the droplet zone. A kinetic model is proposed to explain the transfer of elements between the slag and the weld metal. Hence, it is possible to predict weld metal chemistry for some elements for single pass welds, however, the model requires extension to multipass welds and systems containing alloy fluxes.

In view of the complications presented above, an alternative, simpler, approach was adopted by Thewlis and Dainty [52] which was to essentially treat weld metal chemistry as a mass balance between wire and plate chemistry. In order to use equations 3.3 and 3.4 to make predictions of final weld metal chemistry, taking into account dilution and element transfer, it was necessary to reduce the number of variables. Given the complexities introduced in multipass welding, a sensible starting point was a much simpler geometry consisting of only one pass per side. Observation of such welds showed that dilution was invariant with heat input, and that to a first

approximation, it could be considered as having a constant mean value of approximately 56%. This was not unexpected because the plate and wire melting efficiencies were likely to remain invariant with heat input [53, 54].

Therefore, using a simplified form of equation 3.4, i.e.

$$x_W = (1 - D)x_E + Dx_B + \Delta x \tag{3.5}$$

where Δx now represents a more global element transfer function, values for Δx were calculated using values of dilution calculated from bead area measurements for a number of the welds. It was found that Δx values were reasonably small for the elements of interest for the particular ranges of plate, wire and flux chemistries being considered.

For the purposes of linear regression dilution and element transfer were eliminated as regression variables[52], and an equation of the form

$$x_W = Ax_E + Bx_B + C \tag{3.6}$$

was used, in which A, B and C are constants unique for each element, x, which embody information about dilution, element transfer and the presence of a tack weld. A tack weld causes some dilution of the parent plate, and is itself diluted into the weld beads. Therefore, if x_E and x_B are zero for a particular element then a positive value of C would indicate the presence of that element in the tack weld.

Linear regression analysis produced r^2 values which were in most cases significantly greater than 0.8, with multiple correlation coefficients above 0.9. For the particular database welds of interest, it therefore seems that it is possible to make predictions of weld metal chemistry using primarily plate and wire chemistry as inputs, largely justifying the assumptions that dilution is invariant with heat input and that element transfer is small.

The next logical step is to investigate the prediction of weld chemistry through non linear relationships, i.e. neural networks.

3.3.2 Database description

A database was used in this work which contained information for welds manufactured in the laboratory using 3-wire submerged arc welding with one pass on each side. The welding parameters and plate and wire chemistries used were typical of those used in linepipe seam welding. This database was compiled over a number of years at British Steel Technical, Swinden Laboratories, Rotherham, United Kingdom, (now Corus).

Complete data, consisting of approximately 200 different fields (some related) were available for approximately 250 different welds, with partial information for a further 50. According to the characteristics they describe, these fields can be separated into different groups including welding parameters, chemical analysis, mechanical properties and metallography. This work is primarily concerned with prediction of weld metal chemistry and also, with prediction of the mechanical properties, such as toughness, based on metallography, chemical analysis and welding parameters.

The plates used varied in thickness from 15.9 mm to 25.4 mm and were either accelerated cooled or thermomechanically controlled rolled. Different values for the preparation angle of the plate (30-60°) and the electrode stickout (35-45 mm) were used. The database also included both balanced and unbalanced welds, and data for both the inner and outer diameter weld beads. The heat input range is 2.4-7.4 kJ mm^{-1}. The majority of the welds were manufactured using 4 mm diameter wires alloyed with Ti-B or Ni-Mo using Oerlikon OP122 basic agglomerated flux. Where possible, the chemical composition of the exact batch of welding electrode was entered, however, in some cases a mean composition was used.

It is important to note that most of the plates were welded with a tack weld using an Fe-Mn-C wire. The tack weld was mainly continuous along the length of the weld, although some of the welds contained in the database were formed using intermittent tack welds. The location of the tack weld is illustrated in Figure 3.3.

3.3.3 Models used

The first step in applying a regression or neural network technique to a large database is to determine which variables are necessary as inputs. Two different choices of inputs have been used to predict weld chemistry, based on previous knowledge of important parameters and exhaustive trials of possible candidates which may influence the final composition. These two choices represent the best possible performance in the prediction of the composition of each element in the final weld.

The first choice includes 6 variables extracted from the database. The model consists of 5 input units and 1 output. For a given element the output will be the
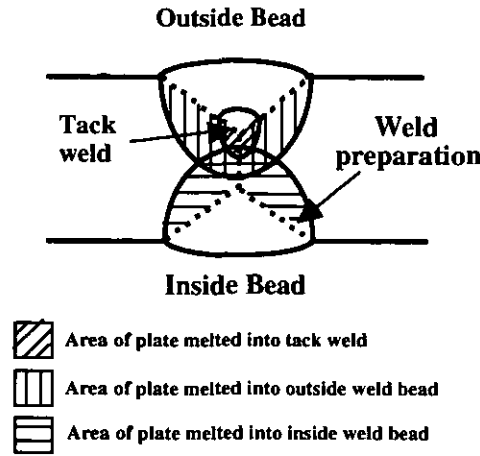
Figure 3.3: Location of tack weld bead geometry, after [53].

concentration of that element in the weld metal. The chosen inputs for this model are: plate thickness, heat input, stickout and the initial composition of the element considered in both the plate and wire.

The second model considered is basically the same as the previous one but adding two more new inputs. The first of the two new inputs takes into account whether the given data belong to inner or outer diameter weld beads. The second one takes into account possible differences if the weld had been made with continuous or intermittent tack welds. These two new inputs are different in that they do not have a particular numerical value, but rather can only be 'yes' or 'no'. It is therefore possible to assign for one of the two choices the number -1 and for the other 1, for example. In the following analysis which involves this 7 input model it must not be forgotten that the data for these two additional inputs are not continuous.

Before feeding the network with the data, each variable (input and output columns) has been scaled with zero mean and normalised with standard deviation 1, as defined in Chapter 2. New data using a neural network model have to be normalised and scaled with the same values as for the training data.

The total number of data pairs used for training and testing the 5 input units to the network for each model predicted is presented in Figure 3.4. Half of the data pairs from the total data available were used for training and the other half for testing the network. After putting the data all together, deleting data with typographic errors and eliminating data from the welds which do not have an entry of every necessary input variable, the number of data decreased from the original database. Missing data is one of the most important problems when neural networks use real data. The

41

lack of data limits the ability of the neural network to accurately predict the weld composition of these, as can be seen particularly for the case of calcium and oxygen. Magnesium has not been studied because there are not enough data available. The number of total data pairs used for the model with 7 inputs has just one or two data pairs, depending on the element, less than the model with 5 input units.
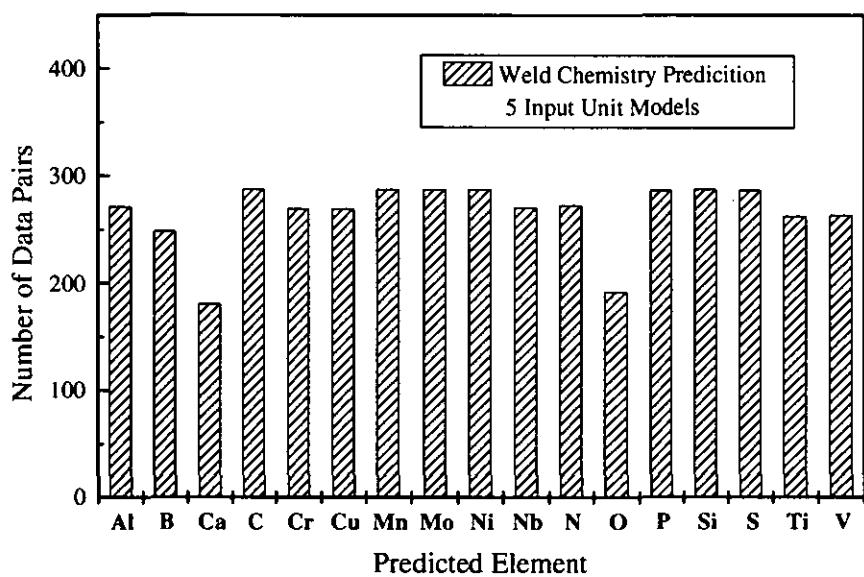

Figure 3.4: Total number of data pairs used for training and testing the neural network models with 5 inputs for every element.

In Figure 3.5 the average chemical composition for each element in the plate, wire and weld for each element is illustrated. An important point to consider is the distribution of the data. For the major elements within the welds, Mn, Si, Ni, Mo, Cu and to some extent C, there was a good spread of chemical compositions present. However, for elements present in only minor quantities, such as Ca, Mg, and to some extent O, all welds contained similar amounts of each, giving a much reduced range over which predictions can be made.

The architecture used, consisted of one input layer with 5 or 7 inputs, as described above, an output layer with one output, the weld composition of the element. Architectures with one hidden layer containing from 1 to 10 hidden units have been evaluated for each element and each choice of inputs. The optimal number of hidden units for each number of inputs and element for the predictions has been selected as the one showing the least test error, and preference has always been given to the simplest model.
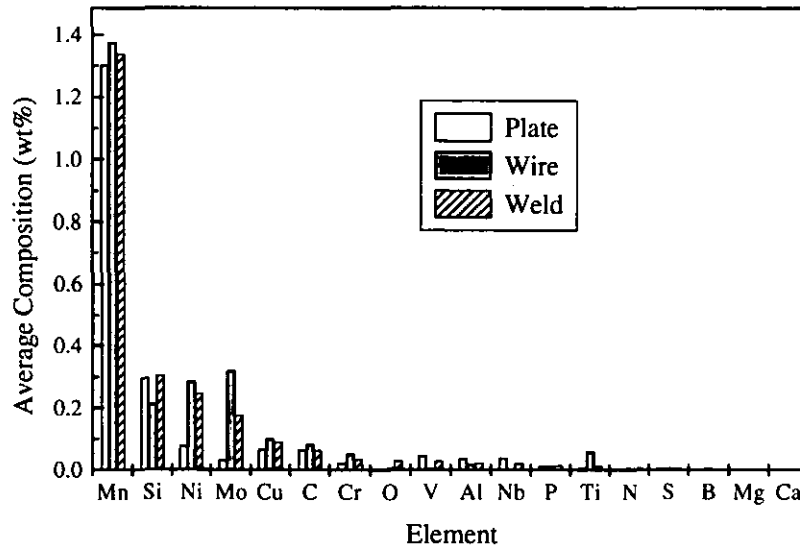
Figure 3.5: Plate, wire and weld average composition for each element available in the database.

3.3.4 Network results and comparison

Throughout the remaining sections of this chapter the main features of the results for the weld metal chemistry prediction will be explained by consideration of two elements: titanium and nickel.

Firstly, the results for the model with 5 input units which predicts weld titanium composition are presented. In Figure 3.6 the average sum squared error for the total, training and test data sets, is plotted as a function of the number of hidden units in the neural network. As the number of hidden units increases the complexity of the model grows, that is to say, that the number of parameters in the model increases and therefore the non-linearity of the relationship between the inputs and the output is more acute. If there are no hidden units the model is simply a linear model with direct proportionality between the input and outputs. As has been discussed, it is the test data set which gives more information about the capabilities of generalisation of the net. Plotting the results in this way makes it is possible to choose a correct model within the ones considered, i.e. one which is able to generalise appropriately.

The titanium error plot, Figure 3.6, shows a typical behaviour. The errors are decreasing from a hypothetical linear model until an optimum non-linearity which in this case happens at 4 hidden units. From 4 hidden units onwards the test error is quite similar. Therefore a reasonable choice to predict titanium weld chemistry is a model with 4 hidden units.
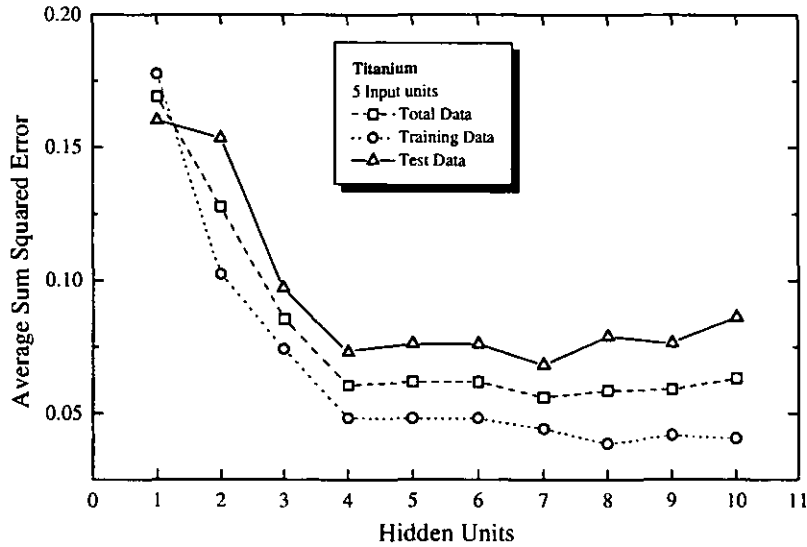
43

Figure 3.6: Average sum squared error as a function of the hidden units predicting titanium weld composition. Up triangle, circle and square symbols represent test, training and total data sets respectively, with the lines drawn for convenience. The model used has 5 input units.

The results for the model with 4 hidden units are presented in Figure 3.7 for the training and test data. The data predicted by the network are plotted as a function of the target data from the original database. It should be noted that the numerical values on the axis represent the normalised data rather than the absolute values. If the network prediction was perfect all the points would lie on the line '$y = x$', also illustrated. It can be seen from Figure 3.7 that the distribution of data points for both the training and the test set are similar and close to the '$y = x$' line. The error in the results for the training set always are expected to be better than for the test set because of the network has learnt from the training set.

A slightly different behaviour is presented in the case of nickel with a 5 inputs network model, i.e. plate thickness, heat input, stickout and the initial composition of nickel in both plate and wire. In Figure 3.8 the average sum squared error for the different data sets as a function of the number of hidden units is presented. In this case the trend is quite different from titanium and there is no clear difference between a simple model and a more complex one; a good choice, therefore, may be a simple model with two hidden units.

In Figure 3.9, training and test results are presented. There is a very good match between target for this relatively simple model with only a few 'outliers' poorly predicted.

44

Figure 3.7: Training and test data versus target data for the prediction of titanium weld composition using a model with 5 input units and 4 hidden units. The numerical values on the axes correspond to the normalised values of the target data such the mean is zero and the standard deviation 1.

Figure 3.8: Average sum squared error as a function of the hidden units for the prediction of nickel weld composition. Up triangle, circle and square symbols represent test, training and total data sets respectively, with the lines drawn for convenience. The model used has 5 input units.
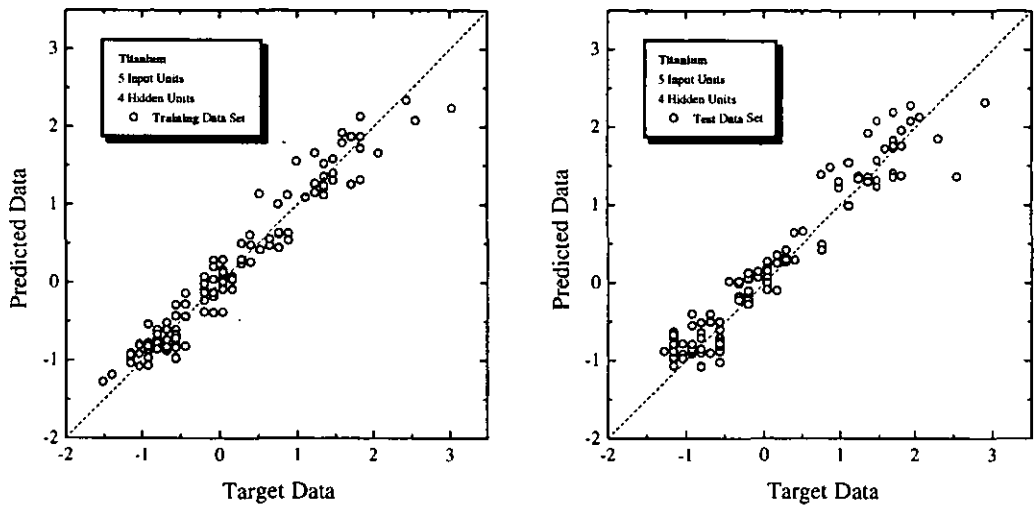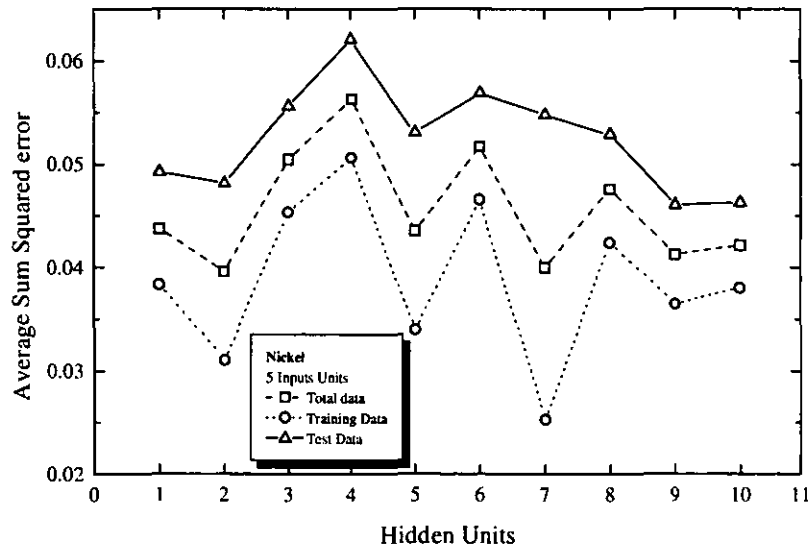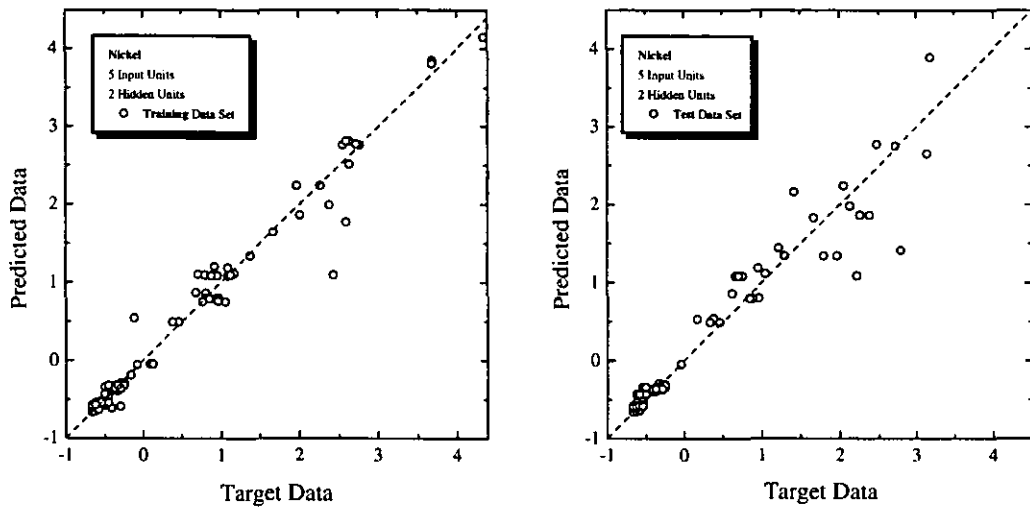
Figure 3.9: Training and test data versus target data for the prediction of nickel weld composition using a model with 5 input units and 2 hidden units. The numerical values on the axes correspond to the normalised values of the target data such the mean is zero and the standard deviation 1.

In Figure 3.10 the results for titanium and nickel are now presented together with the error as a one standard deviation. If the nickel test data set is considered, the points poorly predicted have an associated large error given by the net. This error, however, usually incorporates the 'correct' value which means that some of the samples from the Monte Carlo chain have predicted correct values, but not the majority of them. This is different from the situation where a predicted point is very far away from the correct value and in addition the error bars are very small which would mean that all the samples gave wrong values for this data pair, indicating that the network model is not flexible enough.

The results using the second model with 7 inputs are now presented. This new model incorporates the same 5 inputs as the previous model plus a new one taking into account whether the given data belong to inner or outer diameter weld beads and a second one taking into account whether the weld has been made with continuous or intermittent tack welds.

In Figure 3.11 the error for the different data sets predicting titanium with 7 inputs are presented. The errors for the data sets for titanium when the number of hidden units is increased have a similar behaviour to the model with 5 inputs. A 'good' choice again for the number of hidden units would be 4. In this 7 input case adding the two new inputs to the model makes no significant improvement in the results. Figure 3.12 shows the predicted data for training and test data, together
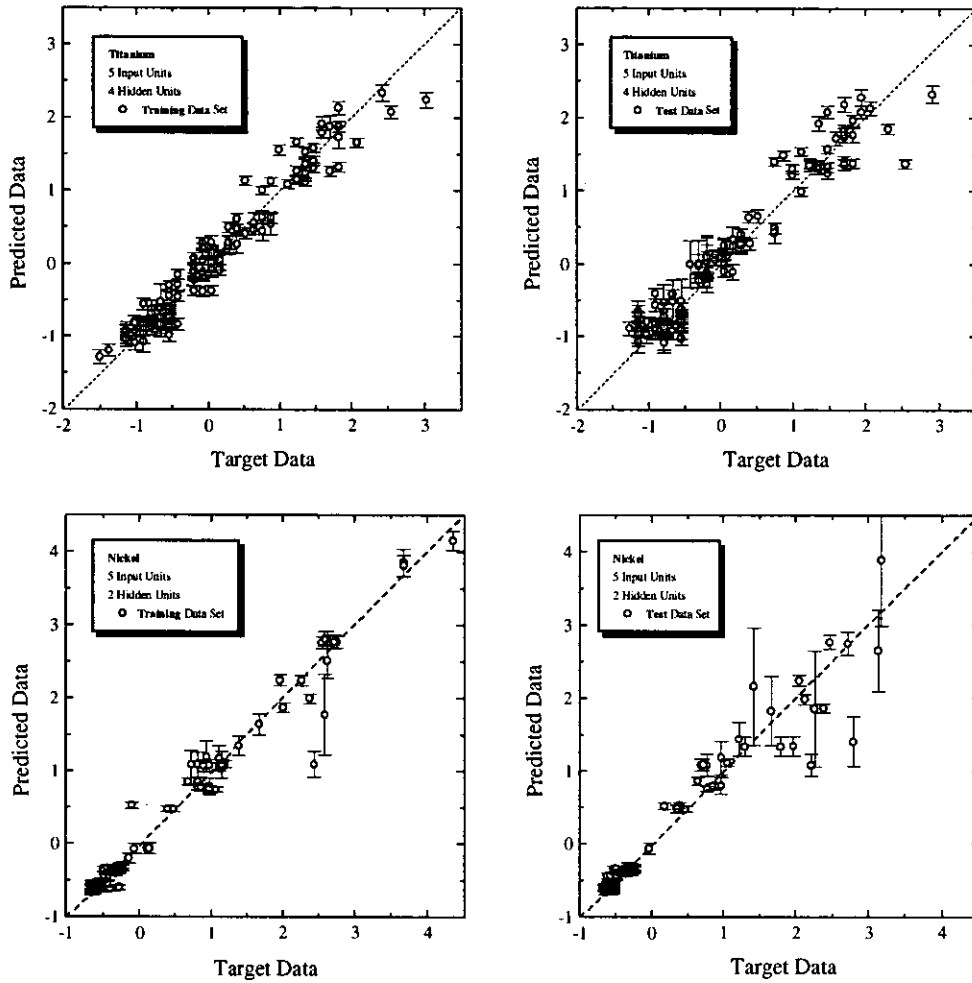
Figure 3.10: Comparison between the best models used to predict titanium and nickel weld composition, both with 5 input units but with 4 hidden units in titanium case and 2 hidden units in nickel case. Predicted training and test data versus target data are plotted with error bars. The error bars represent one standard deviation.

with one standard deviation as the error bar, for the model with 7 inputs and 4 hidden units.

In the case of nickel using the 7 inputs model, the behaviour of the results is again quite similar to the model with 5 inputs, Figure 3.13. Increasing the number of hidden units makes no appreciable change in the error, and therefore it is adequate to choose 1 hidden unit and even it is sufficient to chose a linear model without any hidden units. In Figure 3.13 there is a big test error found for the case of 3 hidden units. This is because this particular network run has not reached equilibrium and some of the samples considered are 'wrong' because, due to the short initial phase, the parameters of the net have taken on extreme values. With these kind of graphs

47

Figure 3.11: Average sum squared error as a function of the hidden units predicting titanium weld composition. Up triangle, circle and square symbols represent test, training and total data sets respectively, with the lines drawn for convenience. The model used has 7 input units.
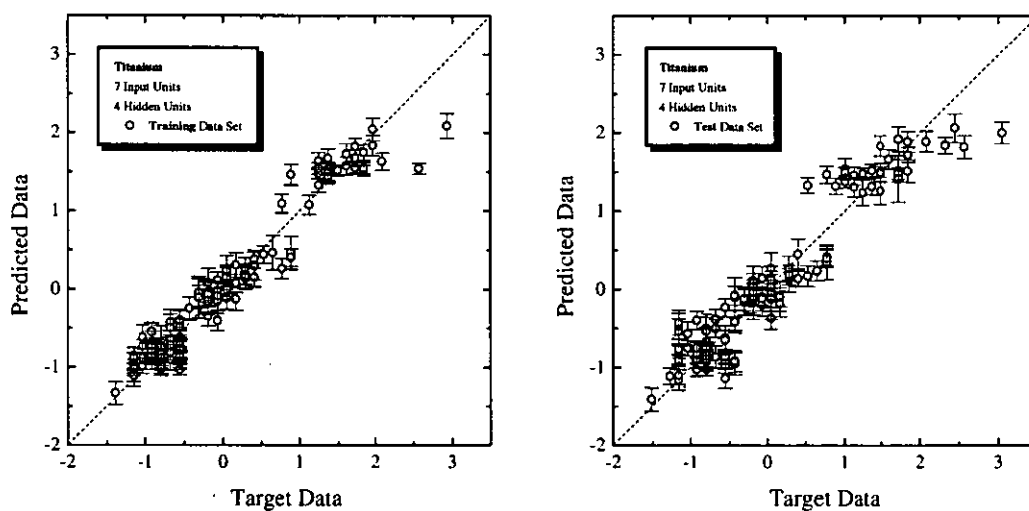
Figure 3.12: Training and test data versus target data for the prediction of titanium weld composition using a model with 7 input units and 4 hidden units. The numerical values on the axes correspond to the normalised values of the target data such the mean is zero and the standard deviation 1. The error bars represent one standard deviation.

it is very easy to say when a net is not working properly, because such large changes in the errors are unlikely when the number of hidden units is only increased by one. In Figure 3.14 the training and test data predicted are shown for the model with 7 inputs and 1 hidden unit for nickel. Now the model is not as flexible as the one with 5 inputs. In Figure 3.10, for the test data, the points which were poorly predicted at least had a big error which contained the real value, however, for 7 inputs the error bars for such values are smaller, indicating that the samples cannot predict properly, even including the error bar, the correct values for these data pairs. In general, it was found for all the elements that the choice with 5 inputs was better than the one with 7 input units.
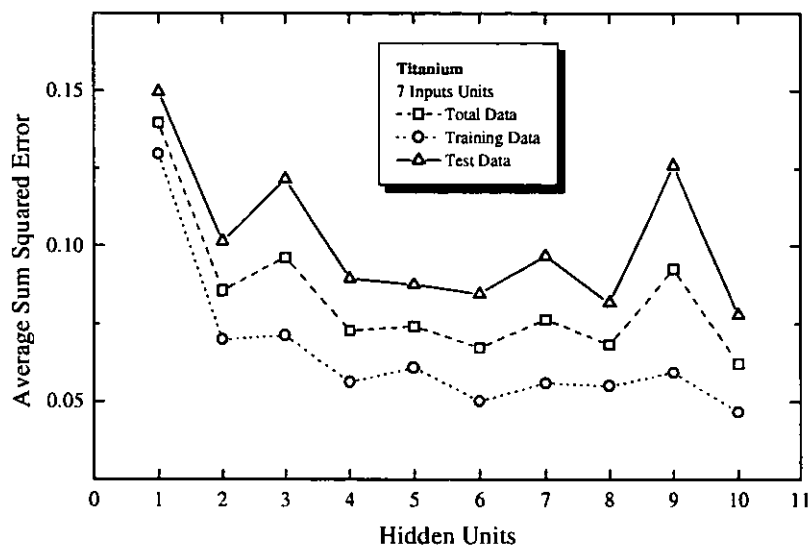

Figure 3.13: Average sum squared error as a function of the hidden units predicting nickel weld composition. Up triangle, circle and square symbols represent test, training and total data sets respectively, with the lines drawn for convenience. The model used has 7 input units.

It is important to note that no allowance for flux chemistry has been made in the neural network models developed above. The majority of the welds in this example were made with very similar fluxes, and indeed ones that are expected to be essentially neutral. One interesting example has been found in the case of the nickel predictions. Inspecting the points which are not predicted well by the network and tracing them back to the database, it was found that most of them belong to welds made with a different flux which contains Ni-Mo powder. It is possible to introduce an additional input into the network taking this into account. In this case the extra input was chosen to have the form of a binary input, with a discrete value for welds without

49
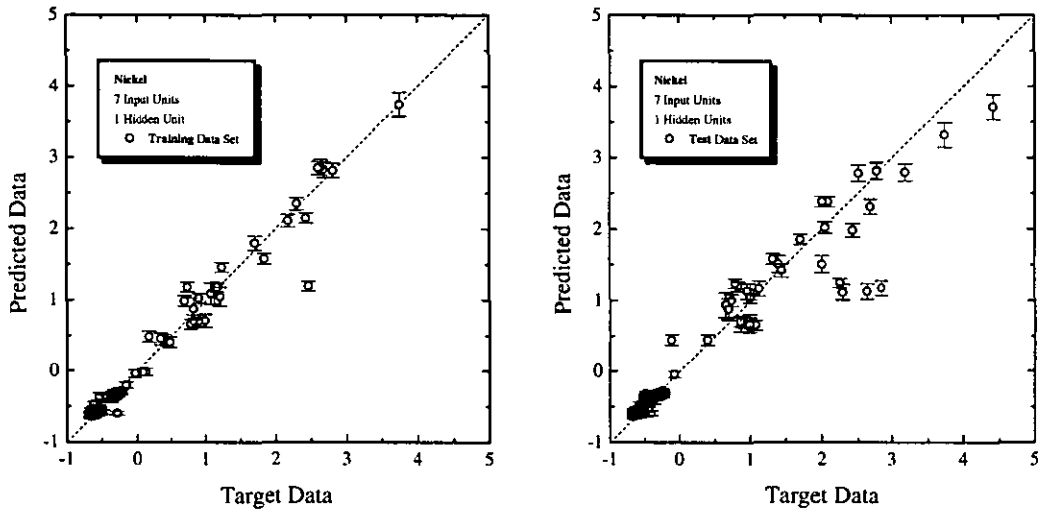
Figure 3.14: Training and test data versus target data for the prediction of nickel weld composition using a model with 7 input units and 1 hidden units. The numerical values on the axes correspond to the normalised values of the target data such the mean is zero and the standard deviation 1. The error bars represent one standard deviation.

Ni-Mo powder and a different discrete value for welds made with Ni-Mo powder. The new model will therefore have 6 inputs: plate thickness, heat input, stickout, initial composition of the element considered in both plate and wire and this new binary input. If such a neural network was required to be extended to fluxes of many different chemical compositions then the type of input variable needed to enter the flux composition would have to be considered very carefully. In order to produce a completely general model for a variety of different fluxes, e.g. some fluxes are known to be manganese and silicon donating, some just manganese donating etc., an additional input variable would be necessary for the flux composition with respect to each element.

The new predictions incorporating the extra input variable representing flux composition are shown in Figure 3.15 for models with 6 input units. It can be seen that the results with the new model taking into account the additional input are significantly better, the test error being lower than that for the model with only 5 inputs. However, investigation of the sum squared error of the network as a function of the number of hidden units actually shows that with the extra input concerned with the flux composition, a more complex neural network model with 4 hidden units is even more accurate, indicative of possible interactions between the wire, plate and flux. This is illustrated in Figure 3.16.

Thus, the importance of prior metallurgical knowledge in the selection of the input variables needed to create the neural network models has been demonstrated. If relevant inputs are not included the network cannot hope to predict accurately.
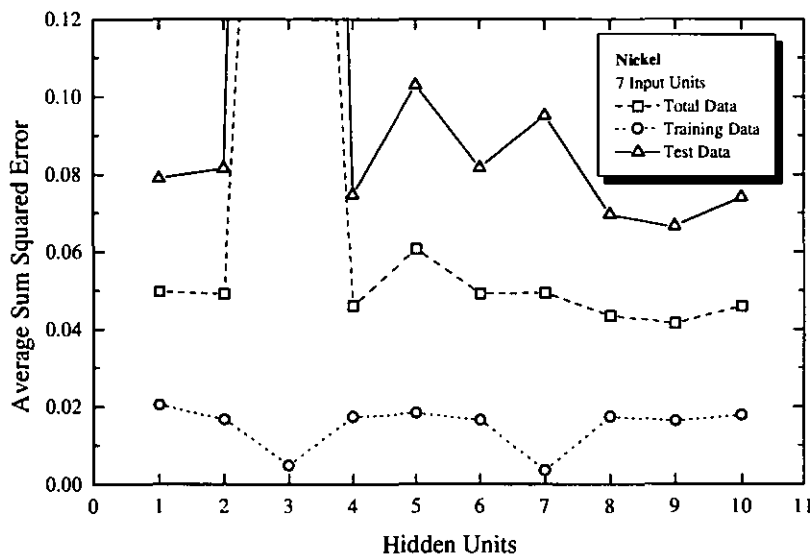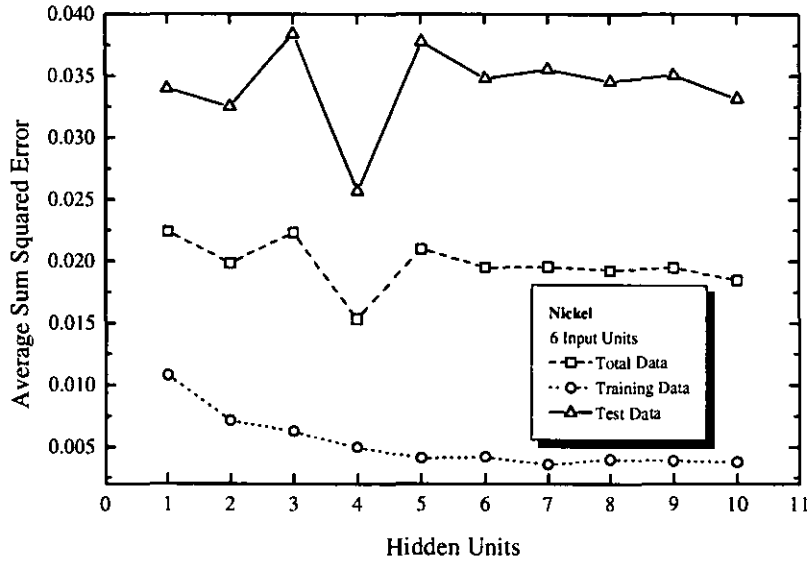

Figure 3.15: Average sum squared error as a function of the hidden units for the prediction nickel weld composition. Up triangle, circle and square symbols represent test, training and total data sets respectively, with the lines drawn for convenience. The model used has 6 input units.

A summary of all the results can be obtained from Figure 3.17. In this figure the average squared error for 4 different models have been plotted. These four models are: the neural network models with 5 and 7 inputs and two linear regression methods with 2 input units (plate and wire composition) and 5 input units (same inputs as the neural network model with 5 inputs). Basically, the linear regression models have been fitted following:

$$Y = b_0 + b_1 X_1 + ... + b_k X_k \qquad (3.7)$$

where b's are parameters, Y is the output and X's are the inputs considered. Given the training data pairs,$((i^{(1)}, t^{(1)}), ..., (i^{(n)}, t^{(n)}))$, a residual having Gaussian distribution with mean 0 and variance σ^2 can be defined as follows:

$$res_i = y_i - (b_o + b_1 x_{1i} + ... + b_k x_{ki}) \qquad (3.8)$$

51

Figure 3.16: Training and test data versus target data for the prediction of nickel weld composition using a model with 6 input units and 4 hidden units. The numerical values on the axes correspond to the normalised values of the target data such the mean is zero and the standard deviation 1. The error bars represent one standard deviation.

The best parameters, b, can be obtained by minimising the chi-squared (or sum squared error SSE)
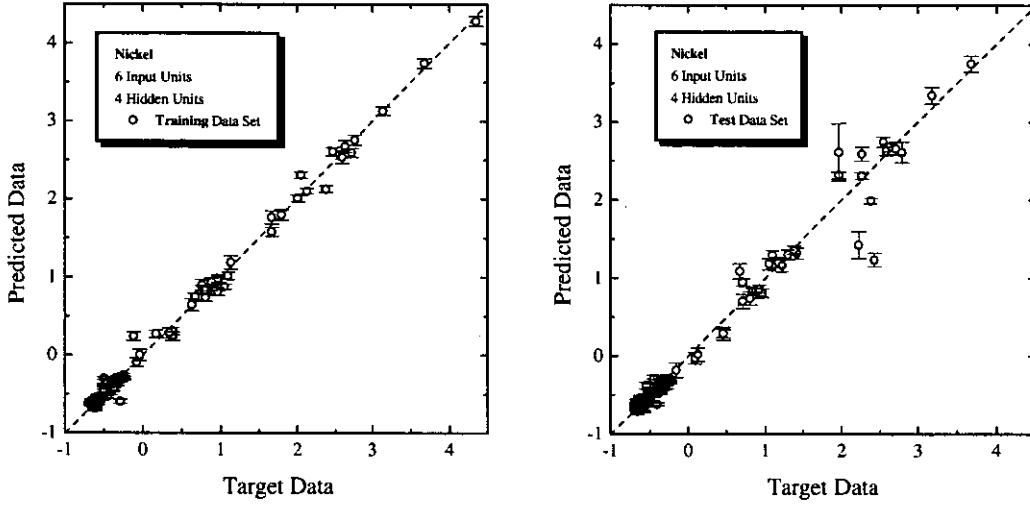
$$\chi^2 = \sum_{i=1}^{N} res_i^2 \qquad (3.9)$$

One method to simulate a linear relationship would be to use the same algorithms as in the Monte Carlo approach with 0 hidden units, in order to minimise the residuals. However, in this case linear regression has been performed using the facilities given by the commercial package Microcal Origin [41]. Similar, if not identical, results would be obtained for the linear relationship when calculated with different packages and methods. In order to compare with the neural network models, the same random training and test data have been used in each case.

Many of the conclusions from this work can be obtained from Figure 3.17. In general, for almost all elements, the linear approach with 2 inputs is not a bad option to predict properly the weld composition. This means that for many of the elements a simple relationship must exist between plate, wire and weld chemistry. The best improvement can be achieved using a neural network with 5 inputs. In general, a model with 7 inputs does not give an appreciably large improvement. On the other hand, there are a few elements poorly predicted for all of the methods - oxygen,

niobium, sulphur and calcium. One of the main reasons for this could be that there are not enough data available, or simply that the choice of inputs is not appropriate for these elements. It should be noted that the concentrations of these elements, which are poorly predicted, are very small. Also, it should be noted that the comparison between neural networks and linear regression is made here only on the basis of the experimental dataset used, which was restricted largely to similar one pass per side welds, with a very limited range of flux chemistries.
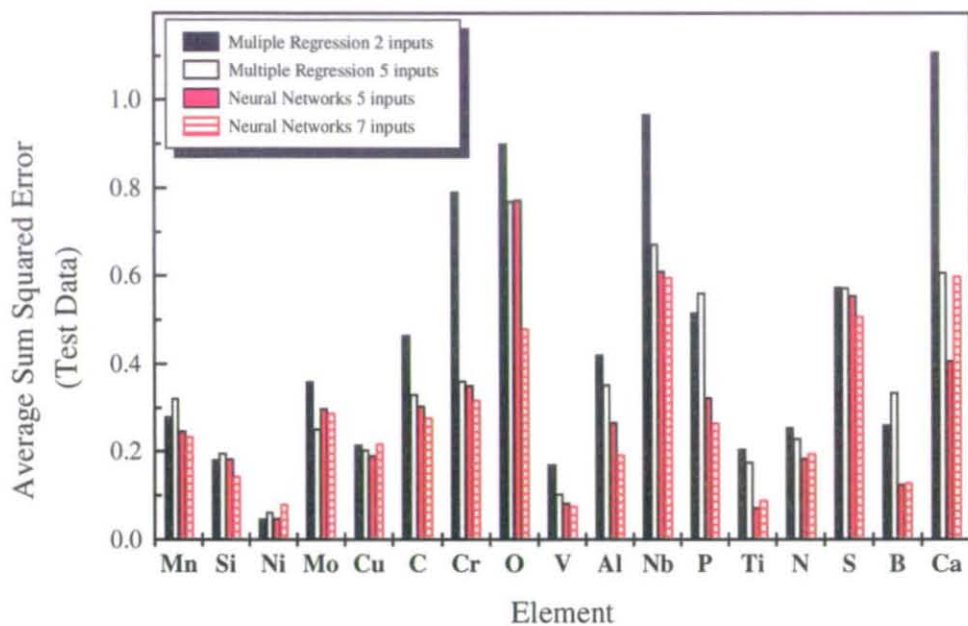
Figure 3.17: Average sum squared error on test data for the prediction of weld composition of each element in the database using different regression models: multiple regression with 2 inputs and 5 inputs and neural networks analysis with 5 and 7 input units. Only the best models for each neural network with the optimum number of hidden units are showed.

3.3.5 Input relevance

An attempt to measure the importance of the inputs on the final weld composition has been made. After trying with many different ways to determine which input is the most important [5, 55, 19, 13] a simple method based on differences, i.e. the effect of a change in an input on the output, has been used.

A simple method can illustrate how each input affects the output. To explain the method, it should be noted that all the inputs and outputs are normalised with standard deviation 1 and scaled with zero mean. In a previous stage, the net is fed

with all the inputs set to their mean value, zero, and a value for the output is obtained. The objective is to see how the output is modified when each input is changed in a systematic manner. As the inputs are normalised, it is possible to compare equal relative changes. For example, feeding the net with two data pairs created as: all the inputs are set to zero and one of them set to the value 0.25, and similarly with all set to zero and one to -0.25. This method cannot be used to measure the importance of each input in models with binary inputs like the one that has been used with 7 inputs, or the special one used with 6 inputs for nickel. In order to use this method, all the inputs must be continuous. Also it is important to note that this combination of values selected by hand does not represent a real experiment, rather a thought experiment which throws light on the relevance of each of the inputs.

In Figure 3.18 the results of this method are presented for the titanium model with 5 inputs and 4 hidden units. The absolute differences between the maximum and minimum value are plotted for each input, also an arrow showing the tendency of the output by an increasing of the correspondent input is shown. It is found that it is the wire variation which provokes a major change on the output, followed by the plate composition. As expected, it is possible to see that increasing the values of plate and wire concentrations keeping the rest of the variables constant, increases the weld composition. The same study has been done for the nickel model with 5 input units and 2 hidden units, and the results are shown in Figure 3.19. The behaviour of nickel is quite similar to that of titanium.

The same input relevance study has been performed for the other elements in the database. From all of the calculations performed it is clear that for certain elements, for example nickel, titanium, molybdenum, chromium, and sulphur it is the wire composition which dominates the final weld composition. However, for other elements, for example vanadium, aluminium, copper, phosphorus and nitrogen it is the plate composition which dominates the final weld composition. For the other elements it is not clear which of the two is the dominant input. However, a general conclusion is that the plate and wire composition dominates the final composition of the weld above factors such as heat input.

3.4 Predicting mechanical properties: toughness

3.4.1 Introduction

The ability to predict weld metal chemistry is of great importance in the determination of microstructure, and ultimately the mechanical properties of a weld metal.

Figure 3.18: Relevance of every input on the prediction of titanium weld chemistry. Arrows represent increasing or decreasing of titanium in the final weld with an increasie of every input. Predictions are based on a simple model in which one input is changed, keeping the others with a fixed value.
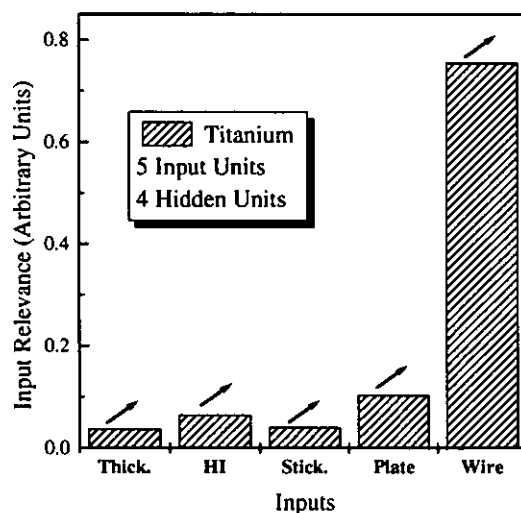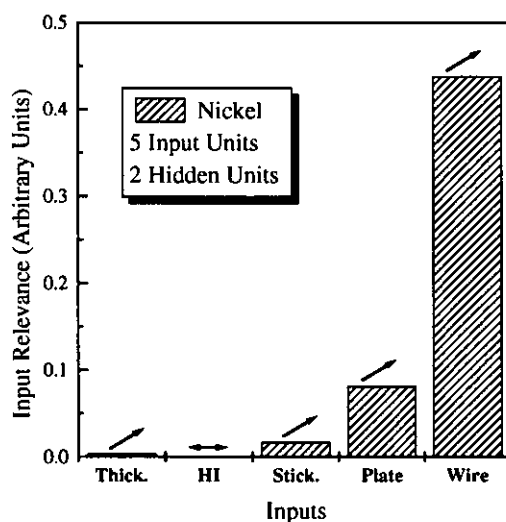

Figure 3.19: Relevance of every input on the prediction of nickel weld chemistry. Arrows represent increasing or decreasing of nickel in the final weld with an increase of every input. Predictions are based on a simple model in which one input is changed, keeping the others with a fixed value.

One of most important mechanical properties for engineering purposes is toughness. Toughness of a material is defined as the energy needed to break it (energy absorbed in fracture). There are several ways to measure toughness, the most common is by impact testing in which the material is struck with a hammer and the energy absorbed by the material in fracture is obtained. Impact toughness testing is mainly a ranking technique [42]. A brittle material is defined as one absorbing little energy, whereas a tough material would absorb large amounts of energy in the fracture process. Metals generally have high toughness, whereas glasses and ceramics have low toughness values. One of the most important requirements from welded joints is that they should not fail in a brittle manner, i.e. that they should be tough and absorb a large amount of energy during fracture.

Typical approaches used to predict toughness are based on linear regression analysis of many variables. These linear regression methods used traditionally [56] are not capable of simulating the toughness behaviour properly because the real behaviour of the toughness with respect to the variables in weld process is clearly non-linear.

A neural network technique has been used to predict Charpy impact toughness of C-Mn Steel arc welds following Mackay's ideas by Bhadeshia et al. [57]. The database used in Bhadeshia's work and the parameters for the network can be obtained from the MAP Website [58]. The same technique has been used by Cool [59] to predict the yield and ultimate tensile strength of steel welds.

3.4.2 Models used

For the prediction of toughness, the results of three different models chosen will be shown in this chapter. Different combinations of variables and models have also been tested but the results are not remarkable. The first two models take into account only weld composition. The inputs chosen for the first model with 9 input units are: the weld composition of carbon, manganese, silicon, nickel, aluminium, phosphorus, sulphur, nitrogen and oxygen, and also test temperature. A second model has been tested with the same input units as above plus two new input variables: the weld composition of molybdenum and nickel. A third model contains also microstructural information. This third model contains 13 input units including the input variables for the model of 11 inputs plus acicular ferrite percentage (AF%) and primary ferrite (PF%). In Table 3.1, the range of all variables used in the 13 input model are presented.

In Table 3.2, the total data available and the quantity of data used for both training and test data are shown. It can be seen from Table 3.2, that the quantity

Variable	Range
Weld C (wt%)	0.042-0.096
Weld Mn (wt%)	0.91-1.56
Weld Mo (wt%)	0.005-0.46
Weld Si (wt%)	0.19-0.53
Weld Ni (wt%)	0.02-0.96
Weld Al (wt%)	0.008-0.04
Weld P (wt%)	0.009-0.023
Weld S (wt%)	0.002-0.011
Weld N (wt%)	0.004-0.013
Weld O (wt%)	0.021-0.043
Temperature (K)	143-333
Acicular Ferrite (%)	60.5-98.2
Primary Ferrite (%)	1.6-25.1
Charpy toughness (J)	7-211

Table 3.1: Variable descriptions for the 13 input units model predicting toughness

	Toughness (9 i)	Toughness (11 i)	Toughness (13 i)
Total Data	1270	1270	842
Training Data	635	635	421
Test Data	635	635	421
Input Units	9	11	13

Table 3.2: Number of data pairs for models predicting toughness

of data available to predict toughness is larger than for the models used to predict weld chemistry, because the database included the values of toughness at various temperatures, in particular: -1300°C, -1100°C, -900°C , -700°C, -500°C, -300°C, -200°C, -100°C, 200°C, 400°C and 600°C.

The data have been scaled to zero mean and normalised between the range [−0.5, 0.5]. Note that earlier work with the same data has previously been carried out with a different normalisation method, i.e. zero mean scaling and normalised with one standard deviation, although this is of no consequence for the final predictions.

3.4.3 Network results and comparison

The results of the three models used to predict toughness are shown in Figures 3.20, 3.21 and 3.22. The average sum squared error for the models with 9, 11 and 13 input units respectively, are presented. It can be seen that the behaviour follows the same trends for each of the three models. The errors decrease with the number of hidden units until an optimal configuration is reached. This optimal configuration is reached for each model at 7 hidden units, see test error on the figures. These figures reveal

also the non-linearity of the toughness with respect to the input variables, because of the sharp decrease in the error if it is compared with a model with one hidden unit or extrapolating with zero hidden units, which represents a linear model.
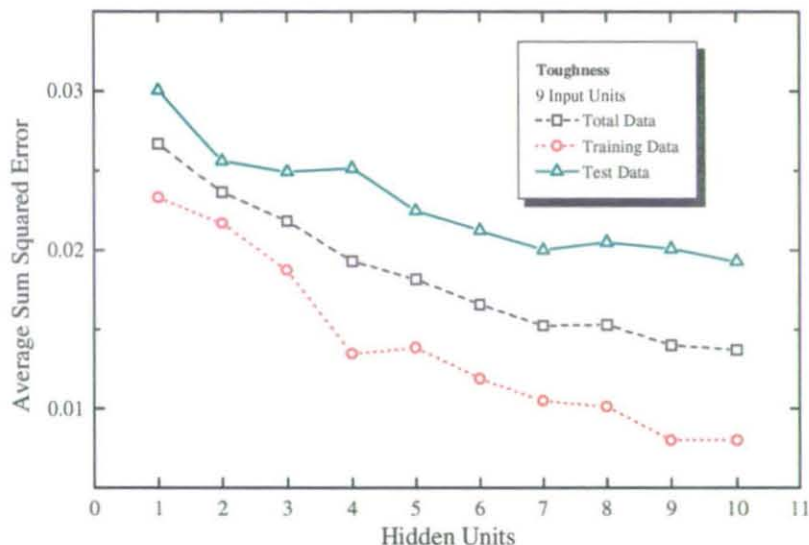

Figure 3.20: Average sum squared error as a function of the number of hidden units for prediction of toughness. Up triangle, circle and square symbols represent test, training and total data sets respectively, the lines drawn for convenience. The model used has 9 input units.

The second model, in which molybdenum and nickel were added as inputs, does not make significant improvement if it is compared with the 9 inputs model. However, the third model which includes microstructure information does give a significant improvement, i.e. smaller test errors. It is this third model with 13 input units and 7 hidden units which appears to be the best of those considered. This model is therefore selected to make predictions, and the results for training and test data are presented in Figures 3.23. In Figure 3.23, the error bar for each point is not plotted due to clarity.

When comparing between models with different number of inputs, we have to be aware that different training and test data set are used with normally a different number of data pairs. The training and test data have been extracted randomly and therefore are representative of the whole range of the data, so the differences arising from the use of different training and test sets are not important. It should be noted that if we want to use the same dataset used in one model, i.e. 13 inputs, with another model, i.e. 9 inputs, we have to be aware that different values for normalisation are

Figure 3.21: Average sum squared error as a function of the hidden units for the prediction of toughness weld composition. Up triangle, circle and square symbols represent test, training and total data sets respectively, the lines drawn for convenience. The model used has 11 input units.
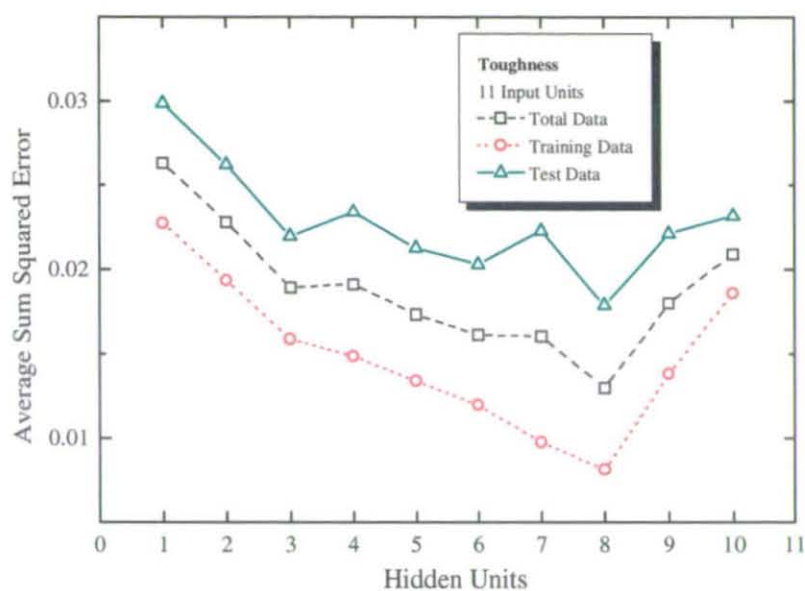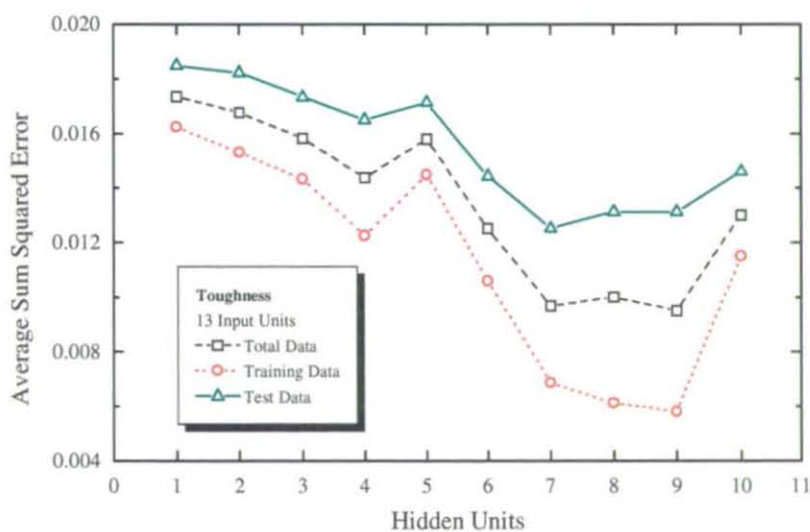

Figure 3.22: Average sum squared error as a function of the hidden units for the prediction of toughness. Up triangle, circle and square symbols represent test, training and total data sets respectively, the lines drawn for convenience. The model used has 13 input units.
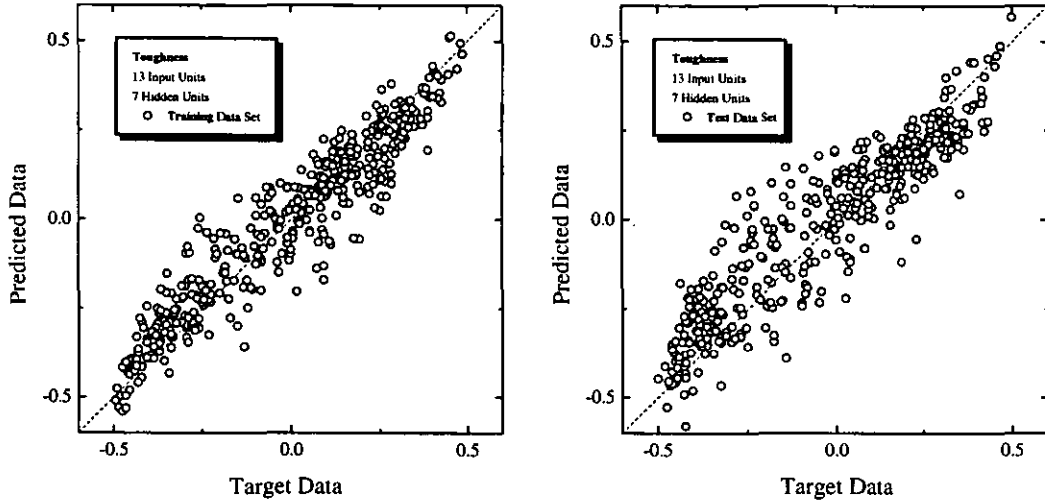
Figure 3.23: Training and test data versus target data for the prediction of toughness using a model with 13 input units and 7 hidden units. The numerical values on the axes correspond to the normalised values of the target data such the mean is zero and the scaling is in the range [-0.5, 0.5]

required. The data set used for 13 inputs has been normalised to use on the 9 input units model with 7 hidden units; the sum squared error obtained was 0.16 higher than the 0.12 obtained with the model with 7 hidden units and 13 inputs.

Hence, it can be seen that the models needed for the prediction of weld metal toughness are much more complex than those for the prediction of weld metal chemistry, and indeed provide a significant advantage over predictions which could be made using simpler linear regression techniques.

It should be noted that the neural network model gives the same predictions if an additional input which effectively contains no additional information is fed into the net. For example, if in the last model we added the ferrite sideplate as an input variable, the main results and behaviour are the same as in the model without this additional input. This is because acicular ferrite, primary ferrite and ferrite sideplate are not independent; they have to sum to 100%.

3.4.4 Input relevance

The importance of each input variable has been studied for the best model, the one with 13 input units and 7 hidden units. To measure the input relevance of each input the same simple method employed on weld chemistry prediction, based on differences

has been used [1]. As has been explained, this method measures the importance of inputs feeding the network with artificial values (not real ones). An input variable is changed in an interval, for example $[-0.5, 0.5]$ keeping the rest of the input units constant at their average value. Extreme values in this interval are calculated by the net for different inputs and the variation on the output response is compared.

The results are shown in Figure 3.24. Figure 3.24 shows clearly that temperature is the most important input of all the 13 variables considered, as expected. Increasing the temperature increases the toughness, alternatively if the temperature decreases the material become brittle. After temperature, it is the quantity of acicular ferrite in the weld which influences the toughness the most. It is well known that the acicular ferrite content of weld metals is one of the most important properties which determine changes in toughness, a tougher weld having a higher acicular ferrite content [42]. It is also found that in terms of the weld metal chemistry, silicon has an important influence on toughness. Also an increase in levels of nitrogen, sulphur or aluminium decrease toughness, making the material brittle, as can be inferred from Figure 3.24, see the arrows. It is necessary to remember that these changes in toughness and associated input relevances are studied in a hypothetical weld. Another thing to take into account is the fact that some of the input variables may not be predicted to be relevant for measurements of toughness, but instead their effect is noticed through other input variables, such as microstructure (acicular ferrite and primary ferrite).

A similar study for the prediction of toughness has been done by Bhadeshia and co-workers [57]. They used a different database from the one used in this work, which included both submerged and manual arc welds. Their model used basically the same inputs as this work as inputs but additionally included yield strength and the type of welding process. Also a different approach of the neural network technique based on the evidence framework was used in their work. They found that the welding process and the acicular ferrite content were deemed to be the most important inputs. Test temperature was also included as an input but was not, however, predicted to be the most important factor. This might be due to the different choice of inputs and the different ranges of temperature contained in the database, being smaller in Bhadeshia's work, i.e. temperature range being 213-293°C in their work and 143-333°C in our database. Also, the possible interdependence of inputs has to be considered when comparing results of input relevances, i.e. acicular ferrite contents would greatly affect yield strength.

---

[1] Other methods, i.e. comparison of weights associated to every input, have also been used to predict input relevances. In all cases the methods agree on the most important input, test temperature, but different predictions are made for the second most important input, revealing the complexity of calculating input relevances, see comments on input relevances in Chapter 2.
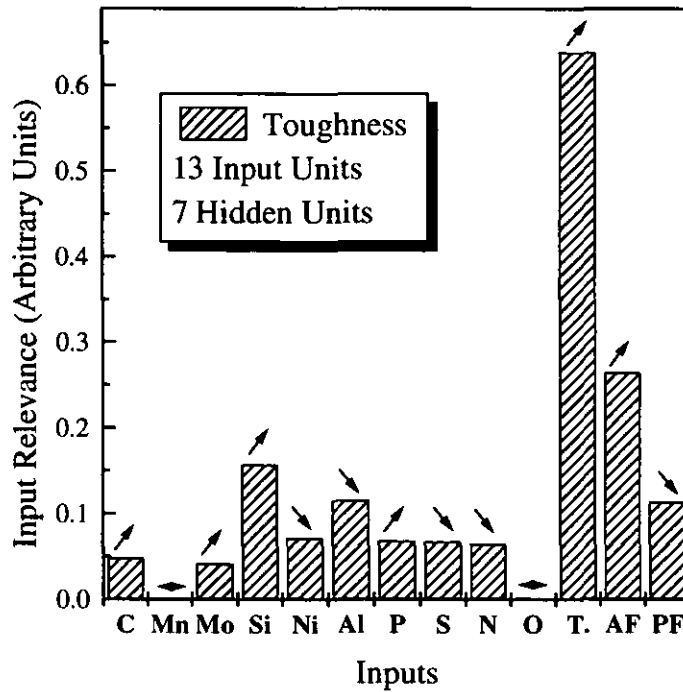
Figure 3.24: Relevance of every input on the prediction of toughness. Arrows represent increasing or decreasing of the input on the final weld with an increasing of every input. Predictions based on a simple model in which one input is changed keeping the others constant.

3.5 Summary

An extensive and complete study of the prediction possibilities of neural network models has been made using a submerged arc weld database. An attempt to predict both weld composition and toughness has been made.

The first part of this chapter was devoted to predicting final weld composition from welding parameters. Each final element concentration in the weld has been studied separately from the others, creating different models. The main inputs taken into account in this part of the work are: plate thickness, heat input, stickout, initial composition of a given element in plate and in the wire. Two additional inputs taken in consideration are whether the welds have been made using continuous or intermittent tack welds, and whether it is the inner or outer diameter bead which is being considered.

Basically, simple models with few ($\sim$ 2) hidden units and 5 input units are suitable to predict weld composition. The small number of hidden units required indicates that relationships between welding parameters and final composition do not require complex models to obtain reasonable predictions, i.e. there is not a high non-linearity

62

so there is not clear improvement compared with multiple linear regression methods. In support of this, a relevance study shows that the composition of plate and wire dominate the final composition in the weld. Elements like nickel, vanadium, titanium and boron are accurately predicted whereas oxygen, niobium, sulphur and calcium are poorly predicted.

The second part of the chapter deals with toughness predictions taking into account weld composition, temperature as well as microstructural characteristics. The best model for predicting toughness contains 13 inputs and 7 hidden units. This model shows a big improvement compared with a linear model, i.e. without hidden units, and it reveals that neural networks are more suitable to predict mechanical properties due to the intrinsic non-linear relationship involved than linear models.

The relevance study shows that test temperature is the most relevant input for predicting toughness, followed by the percentage of acicular ferrite in the weld, as expected intuitively. A higher temperature or percentage of acicular ferrite makes the material tougher, as expected. The model is able to predict that increasing the concentration of N, S or Al, makes the material more brittle.

This work has clearly demonstrated that neural networks are useful in the prediction of complex phenomena for which it is difficult to derive a fundamental model. Similarly, it has been shown that where an intrinsically simple physical relationship exists between input variables (weld metal chemistry) the neural network does not provide a significant advantage over linear regression techniques. For special cases, for example, the welds made with a NiMo flux, the neural network is able to provide fine tuning. In the case of a complex relationship between input and output variables (weld metal toughness) the neural network does provide a significant advantage. It is therefore imperative to carefully consider the structure of the data and the properties which are desired to be predicted before time is expended in creating neural network models. Meaningful predictions cannot be made unless a significant quantity of data is available.

In summary, the application of neural networks to welding problems has been investigated and a number of recommendations have been made as to their future use.

Chapter 4

The atomic structure of symmetrical grain boundaries

4.1 Introduction

Metals are usually present in nature in the form of polycrystalline materials composed of random oriented crystals. The junction of these crystals are bulk interfaces where the perfect crystal structure of both sides is broken by a disordered region. Interfaces are regions of a material composed of just a few atomic layers where the atomic structure and physical properties, i.e. thermal expansion, electrical resistivity, elastic response etc., can differ substantially from those of the bulk and be highly anisotropic. These variations in properties, at the atomic level, affect the behaviour over bigger scales of the material [3], determining some of the most important properties in polycrystalline materials, i.e. embrittlement and toughness. Therefore, a good understanding of the microstructure of such interfaces and their relationships with the physical properties of the bulk material is necessary [60]. Unfortunately, our basic understanding of the atomic structure and properties, even for the simplest interfaces such as grain boundaries, is still very limited mainly because of limitations of experimental techniques.

Bulk interfaces can be classified according to the phases of the crystals at the junction. If these two crystals, which form a bicrystal, are not of the same composition or they are different phases of the same material, the interface is usually referred to as an interphase or heterophase boundary; the interface is usually termed as a grain boundary when both crystals are of the same composition and phase. Grain boundaries are therefore the most common interfaces in polycrystalline materials. Earlier definitions of grain boundaries were also extended to heterophase boundaries and defined as follows:

A grain boundary in a piece of metal is the boundary separating two crystals (or 'grains') that differ either in crystallographic orientation, composition, or dimensions of the crystal lattice, or in two or all of these properties [61].

The complete characterisation of the structure of a grain boundary in a polycrystal requires its study on different length scales [62]. The structure of an interface may be studied at three different levels: large length scales, mesoscopic scale and atomic scale [36]. At large length scales the interface is viewed as flat or curved, separating two crystals with different orientations. In Figure 4.1 an optical micrograph of polycrystalline bcc iron is shown where each individual shape is a unique crystal and the boundary of the shape is the grain boundary. The shape and size of the grains are determined by nucleation and growth events during processing. At such large length scales the characterization of the interface is described in terms of the geometrical (macroscopical) degrees of freedom which determine the orientation of the crystals forming the interface. On the mesoscopic scale, arrays of dislocations can be observed at the interface. To characterize the structure at the mesoscopic scale the dislocation model of interfaces has been used widely [63]. Finally, the atomic scale is described by the various atomic arrangement of atoms at the interface.

At large length scales a grain boundary is defined by its geometrical parameters or degrees of freedom. The grain boundary geometry is related to the orientation of the two crystals forming the interface. Depending on the relative orientation between crystals grain boundaries have been traditionally classified in small and high-angle boundaries. Grain boundaries are normally classified as small-angle when the misorientation between the same crystallographic planes of the two crystals forming the interface is less than approximately $15°$; and high-aengle boundary when is bigger. High-angle grain boundaries can also be distinguished as singular (or special), and general [36, 65, 66]. This definition is based on the relationship between any property of the grain boundary and any of the macroscopic degrees of freedom (geometrical parameters). A singular interface is that the property of which has a cusp with respect to at least one macroscopic degree of freedom, being general boundaries the ones which do not exhibit any cusp on diagrams of a boundary property versus a geometrical parameter. This definition has been usually based on plots between the grain boundary energy and the misorientation angle of the boundary. In these plots, some boundaries present minima of energy compared with the vicinal boundaries with misorientation angles close to these special ones. The special character of a grain boundary compared with others has to be related to its atomic structure [66].

In principle, there are infinite types of grain boundaries depending on which way the two crystals meet. The frequency with which some types of grain boundaries
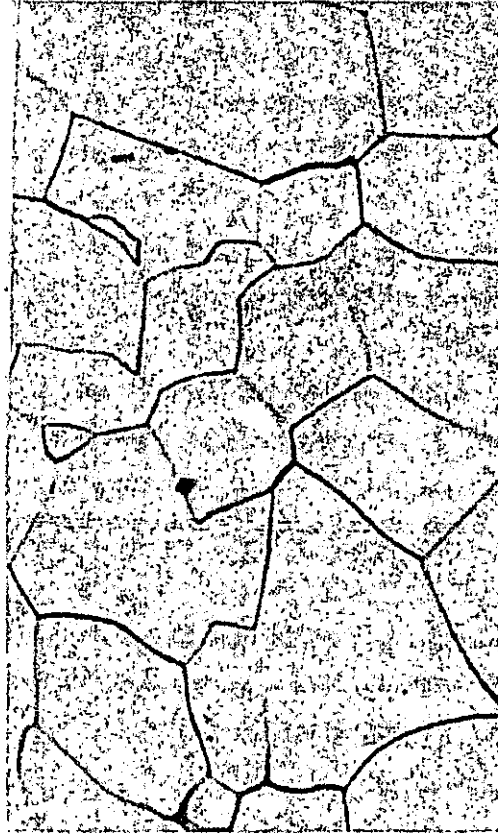
Figure 4.1: Optical microgaph of polycrystalline α-iron, 250×. After [64].

appear in polycrystalline materials is strongly dependent on the processing history of the material [67]. The orientation of crystallographic planes at the boundary can be obtained using the scanning electron microscope (SEM), the transmission electron microscope (TEM) or with X-ray diffraction techniques. On the other hand, to form images in real space of the atomic structure of grain boundaries needs a more powerful technique such as high-resolution electron microscopy (HREM). High resolution electron microscopy can be used to analyse the atomic structure of the boundary region, although there are a number of limitations. Firstly, it is not an easy task to produce oriented bicrystals for the study of a specific boundary required. Secondly, the HREM technique is typically limited to low index tilt axis grain boundaries, i.e. such as <100> and <1$\bar{1}$0>, where the atomic planes parallel to the interface in each crystal have an interlayer distance big enough for the resolution of the microscope [68, 69]. Thirdly, the grain boundary observations are limited to a view along the tilt axis, i.e. parallel to the interface. Also, some magnetic materials interfere with the electron beam of the microscope. Despite all these limitations, images of more complicated grain boundary configurations are becoming available after recent HREM studies [70].

It has been shown above that due to experimental limitations, few grain boundary structures can be experimentally studied and it is in such situations that computer modelling can play an important role. We can use atomistic simulations to gain an insight into the atomic structure of grain boundaries. A study of all the possible types of boundaries can be made in the computer because of the ease with which the macroscopic degrees of freedom can be varied and controlled. Different atomistic simulation techniques have been applied to the study of microstructure and properties of interfaces including: molecular dynamics, Monte Carlo methods, which are reviewed in [71, 36, 65], and more recently ab-initio methods [72, 73, 74] and genetic algorithms [75]. However, comparison of computer modelling with HREM structures, where available, are necessary to validate the models employed [65]. Several studies deal with the comparisons of atomic grain boundary structures obtained by computer modelling and the experimental using the HREM [76, 77, 78, 79, 80, 81, 82].

The main results from experimental techniques and simulations regarding the atomistic structure of interfaces reveal many interesting features:

- the boundary region is composed of a few atomic layers in which the arrangement of atoms is different from those of the bulk;

- there exists a volume expansion close to the interface due to its presence, i.e. the interlayer distance between distinguishable atomic layers parallel to the boundary is larger than in the bulk;

- the 'new' arrangement of atoms is periodic along the interface;

- some typical groupages of atoms, basic units, are identified at different boundaries;

- more than one typical arrangement of atoms can exist for a determined grain boundary, i.e. metastable structures may appear.

In spite of these main results more work is required because there are few systematic studies which can lead us to a quantitative descriptions of the grain boundaries. Few theories, most of them related, have appeared to predict the structure of grain boundaries and quantify the relationship between them and some of their physical properties, e.g. grain boundary energy. The dislocation theory due to Read and Shockley [63] was one of the first models describing the structure of grain boundaries, in terms of a dense array of dislocations or disclinations. The dislocation model, which is based on elasticity theory, has succeeded on the description of small-angle

grain boundaries failing when describing high-angle ones. In high-angle grain boundaries where the overlap between atoms at the core of the grain boundary become important, elasticity theory is no longer applicable and it is necessary to consider the interatomic interactions at the boundary.

All the models that appear after the dislocation theory, are essentially based on Bollman's coincident site lattice model (CSL)[83] which is itself based on geometrical considerations. These models have succeeded in describing the properties of some singular grain boundaries but they have failed to provide their detailed atomic structure, which has been usually inferred from computer simulations. More recently, the so-called generalized coincidence site network has been introduced [84], which generalizes the coincidence site model.

In addition, there are models based on repeated 'units' of atoms at the interface, like the polyhedral and the structural unit model. In the polyhedral unit model the atomic structure of interfaces, the boundary core, is described in terms of the stacking of polyhedra along the interface, which consist of closely packed clusters of atoms [85]. However, this model can only be applied to describe configurations of already known structures obtained by experiment or simulations. In contrast, the structural unit model [86] has been shown to be a very successful method to predict the microstructure of symmetrical grain boundaries. Supported by computer simulations, the structural unit model indicates that any boundary consists of structural units of two other favoured boundaries. Favoured boundaries are composed of only one type of structural unit and normally, they are special boundaries with minimum energy configuration and short periodicity. These favoured boundaries determine a misorientation range describing all the boundaries inside this range by combination of their short periodicity structural units. This description is approximate for the fact that units in intervening boundaries are distorted and also, several metastable structures may appear in the favoured boundaries and therefore at the intervening boundaries [87].

Atomistic simulations of the atomic structure of grain boundaries are based in a good description of the atomic interaction. Different ways of modelling , i.e. different interatomic potentials, have been used in atomistic simulations of grain boundaries, in metals in particularly. The use of pair potentials was widespread in the early atomistic simulations of the atomic structure and energies of grain boundaries in fcc metals [88, 89, 90, 91, 92, 93, 94, 86, 87, 95, 96]. With the development of many-body potentials, these have been common in simulations of defects in fcc metals [97, 80, 98, 99, 100] and bcc metals [78, 82, 81]. However, it has been shown that different choices of interatomic potentials, i.e. pair or many-body potentials, have more influence on

values of grain boundary energies than on the calculation of grain boundary structures [101, 102]. Differences in the atomic structure of grain boundaries can appear when using non-central interatomic potentials. Many-body potentials tend to maintain the interatomic separations and coordinations as close as possible to the bulk, while interatomic potentials including angular dependence prefer to maintain bond angles close to those in the bulk [35].

Simulation studies on grain boundaries in α-iron also started with the use of pair potentials [103, 104, 105, 106, 107], basically using Johnson's pair potential [108]. More recently, several semi-empirical many-body potentials have been developed for α-iron [30, 31, 109, 110, 111], all of them trying to describe the delocalized nature of the metallic bonding and overcoming the problems of the pair potentials. The use of these many-body potentials in the study of grain boundaries in α-iron has been limited to a few grain boundaries [112]. Full ab initio energy calculations have been applied to the study of iron, however these have been limited to the study of small clusters of atoms forming simple grain boundaries [113].

The object of this chapter is to gain an insight into the structural aspects of grain boundaries in α-iron from an atomistic point of view. The first aim is to study the structure of symmetrical grain boundaries in ferritic steels using molecular dynamics simulations. Ferritic steels at typical service temperatures have the bcc-iron structure, α-iron, and therefore simulations have focused on bicrystals of α-iron. This chapter is also a necessary step for the study of radiation damage near grain boundaries, which is the subject of the following chapter in this thesis.

When two crystal grains are adjacent the atoms near the boundary will arrange themselves into some kind of minimum energy configuration. The are many possibilities for local minima, however such possibilities must be consistent with the fact that the particles "should not move too much". It is not really possible to decide in advance how to carry out this minimisation process since the energy depends in a complex way on the positions of the atoms. To determine the minimum energy configurations we cleave two perfect crystals and place them adjacent to each other, following a CSL geometrical description of the bicrystal, but move the positions parallel to the interface to the minimum energy position and allow the crystal to relax.

This chapter explains the computer modelling procedure to obtain final relaxed structures at the atomic level of symmetrical tilt and twist boundaries in α-iron. The chapter starts with a geometrical description of symmetrical interfaces and how they have been implemented as computational atomic blocks. Second is a description of the molecular dynamics procedure employed to relax the simulated bicrystal. Finally, the relaxed structures of symmetrical tilt and twist boundaries are presented and

discussed. Grain boundaries are classified in terms of energy, width and volume expansion.

4.2 Modelling grain boundaries in bcc iron

4.2.1 Bicrystal

Real grains in polycrystalline materials are three-dimensional with curved or flat boundaries. Considering a grain as a perfect sphere, a typical grain in iron has a radius of ~ 10 μm. The computer simulation of a real curved interface of a grain in iron with a full molecular dynamics description would involve large computational resources. Modelling of grain boundaries in this work is therefore based on flat interfaces. These flat interfaces were set up at the centre of rectangular three-dimensional bicrystals. The size of the crystals were of the order of 3.10^5 Å^3 and, contained approximately 40,000 atoms depending on the grain orientation.

The minimum number of geometric variables required to specify a complete geometrical characterization of the interface is called the number of geometrical degrees of freedom of an interface. We distinguish between macroscopic and microscopic degrees of freedom of an interface [36]. The geometrical parameters at the macroscopic level can be thought of as the information required to manufacture a bicrystal from given crystals, with a particular orientation relation between the crystals and a particular interfacial plane. The macroscopic definition of a general grain boundary can be made with five geometrical degrees of freedom which will take into account all the different possible orientations of the two crystals when they meet. Also, three additional microscopic degrees of freedom, (T_x, T_y, T_z), regarding rigid-body translations between both crystals are needed.

There are different ways to define the geometry of a bicrystal. Two common schemes are the interface-plane scheme and the CSL-misorientation scheme [114]; each of them use a different but related set of geometrical parameters.

For the study of grain boundaries, the choice of geometrical parameters based on the misorientation of both crystals, the so-called CSL-misorientation scheme, has been a common practice and this is used here. Following the coincident site lattice misorientation scheme the five macroscopic degrees of freedom are a rotation axis in the direction of the unit vector, $\hat{n}$, the misorientation angle, ϕ, and the grain boundary plane normal, $\hat{n}_1$, in either of the two halves of the bicrystal [114], $\{\hat{n}, \phi, \hat{n}_1\}$. These vectors are defined in the unrotated coordinate system of one of the halves. With these parameters all the lattices sites of a perfect bicrystal can be generated. Knowing

the plane normal to the boundary, $\hat{n}_1$, the lattice sites of the first crystal are also known by just continuing a bcc structure on the direction perpendicular to the plane. The lattice sites of the second crystal are completely determined by rotation of the lattice site vectors of the first crystal, $\vec{r} = (r_1, r_2, r_3)$ in a clockwise sense about an axis $\hat{n}$ through an angle ϕ to a new position $\vec{r'} = (r'_1, r'_2, r'_3)$ (lattice site vectors of the second crystal), following

$$r'_i = \sum_{j=1}^{3} R_{ij} r_j \tag{4.1}$$

$$R_{ij} = \delta_{ij} \cos\phi + n_i n_j (1 - \cos\phi) - \sum_{k=1}^{3} \varepsilon_{ijk} n_k \sin\phi \tag{4.2}$$

were δ_{ij} is the Kronecker delta and ε_{ijk} the permutation tensor. Also, the plane normal of the other crystal is easily determined by $\hat{n}_2 = \mathbf{R}(\hat{n}, \phi)\hat{n}_1$, where $\mathbf{R}$ is the rotation matrix from the previous equation.

Following the CSL scheme, a pure tilt boundary is defined by the condition that the rotation axis, $\hat{n}$, lies in the boundary plane, whereas a pure twist boundary has the rotation axis perpendicular to the boundary plane. Tilt or twist boundaries are symmetric in cubic crystals, if the plane of the boundary has the same Miller index form in both crystals, i.e. if the Miller index in both crystals are the same by any permutation including their signs, e.g. (320) in one crystal and (230) in the other, being asymmetric if the Miller index form is different [1].

Symmetric tilt boundaries are also called twin boundaries, or simply twins. The symmetrical tilt grain boundary (STGB) or twin boundary is the simplest of all grain boundaries made up of two crystals with specular symmetry structure. Given the plane of one half of the bicrystal the other is defined as a specular inversion of the first one with the rotation axis perpendicular to the normal plane, so only two degrees of freedom are necessary to define geometrically a symmetrical tilt boundary.

In Figure 4.2 the arrangement of atoms close to the interface based on a CSL description is plotted for a (210) symmetrical tilt boundary. A solid line separates both crystals forming the interface clearly showing the mirror symmetry of the structure.

---

[1] Planes with Miller indexes h, k and l are denoted by (hkl). To specify all planes of a given crystallograpic type, curly brackets are used, i.e. the class of all cube faces is denoted by $\{100\}$, and includes (100), ($\bar{1}$00), (010), (0$\bar{1}$0), (001) and (00$\bar{1}$) planes. Crystallographic directions are denoted with square brackets, i.e. $[abc]$ is a vector with 'coordinates' $x = a$, $y = b$ and $z = c$. To specify all directions of the same cyrstallographic type arrow brackets are used, i.e. the class of all cube edges is denoted by $< 100 >$, and includes the [100], [$\bar{1}$00], [010], [0$\bar{1}$0], [001] and [00$\bar{1}$] directions.

Solid and open symbols represent atomic sites in adjacent atomic layers along the rotation axis, which in this case is the [001] direction of the bcc structure. The structure is repeated every two atomic layers, $P = 2$, along the rotation axis, being the interlayer distance, d, in the [001] direction of the bcc structure equal to $a_0/2$, where a_0 is the lattice constant. In Figure 4.2 the periodicity of the structure on directions parallel and perpendicular to the interface is shown by repeated squares. The periodicity length of the structure in directions parallel, x coordinate, and perpendicular, y coordinate, to a symmetrical tilt boundary is the same because of symmetry of the bcc structure. (210) and (120) are the planes parallel to the boundary for each crystal of the symmetrical tilt boundary presented in Figure 4.2. The periodicity along this planes is equal to 10 and the interlayer distance equal to 0.64Å i.e. the periodicity length is equal to $P.d$. The misorientation angle between crystals is also drawn and is equal to $\phi = 36.87°$.
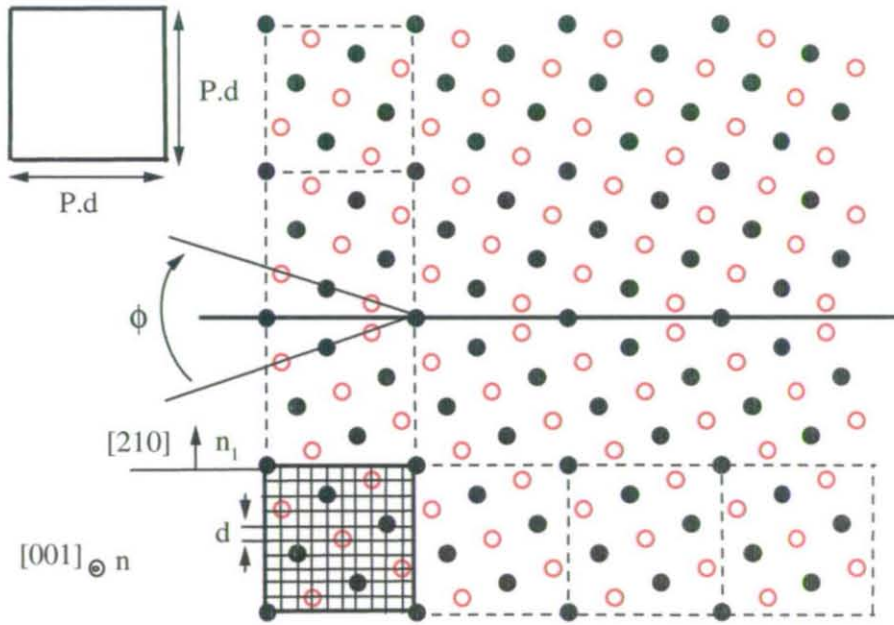

Figure 4.2: Projection along the rotation axis, e.g. [001] coming out of the page, of a (210) symmetrical tilt grain boundary. Solid and open circles represent atomic sites in adjacent planes along the rotation axis. Values of the misorientation angle, interlayer distance and period are $\phi = 36.87°$, $d = 0.64$ Å and $P = 10$ respectively.

In Figure 4.3 a schematic representation of the crystallographic planes and misorientation angle involved in a (210) symmetrical tilt boundary is presented. Planes (120) and (210) represent the same crystallographic planes in a bcc lattice, i.e. <120>. The misorientation angle is defined with respect to the [110] direction of

the ideal crystal, i.e. the normal vector of the grain boundary plane in one of the crystal and its symmetric across the [110] direction, therefore, in this case, $\phi = 36.87\,°$. Alternatively, it is equivalent to define the misorientation angle as the complement of the previous one $\phi = 90 - \phi'$. Therefore knowing the boundary plane, (hk0), the misorientation angle, ϕ', is easily obtained by $\tan(\phi'/2) = k/h$.
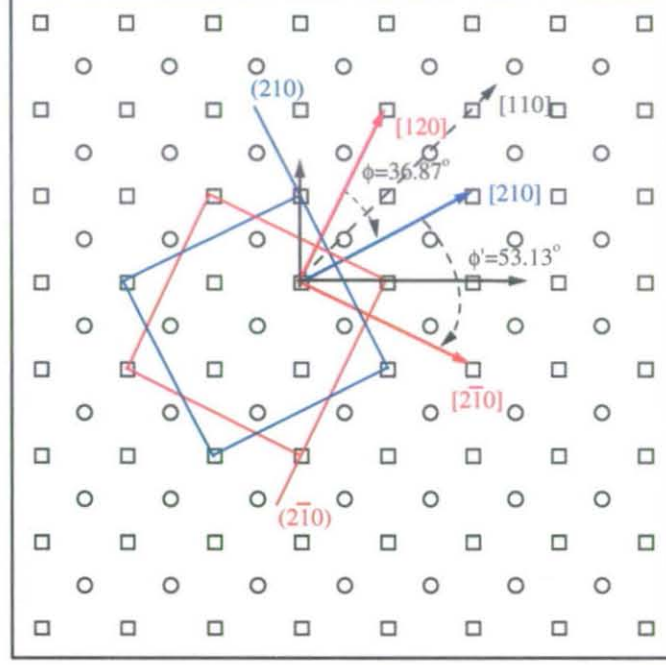

Figure 4.3: Crystallographic planes and angles involved in the construction of a (210) symmetrical tilt boundary in a bcc lattice. Circles and squares represent atomic sites in adjacent planes in the [001] direction.

On the CSL-misorientation scheme the inverse volume density of CSL sites is usually added as a redundant sixth parameter, Σ, a schematic representation of which is shown in Figure 4.4. The value of Σ is a function of the relative orientation of the two grains. By superposing the two cells of length the periodicity of the structure from both halves the number of coincident sites is obtained and the Σ parameter easily calculated as is shown in Figure 4.4.

On the other hand, symmetrical twist boundaries occur when one of the crystals is rotated about a rotation axis which is perpendicular to the boundary plane and both normal planes have the same Miller index form. In Figure 4.5, a schematic representation of a (210) symmetrical twist boundary based on the a CSL model is presented. The rotation axis is chosen along the [001] direction. Top and side views of the boundary are presented in Figure 4.5. The top view is the projection of atomic sites to a plane parallel to the boundary being the side view a projection to a plane
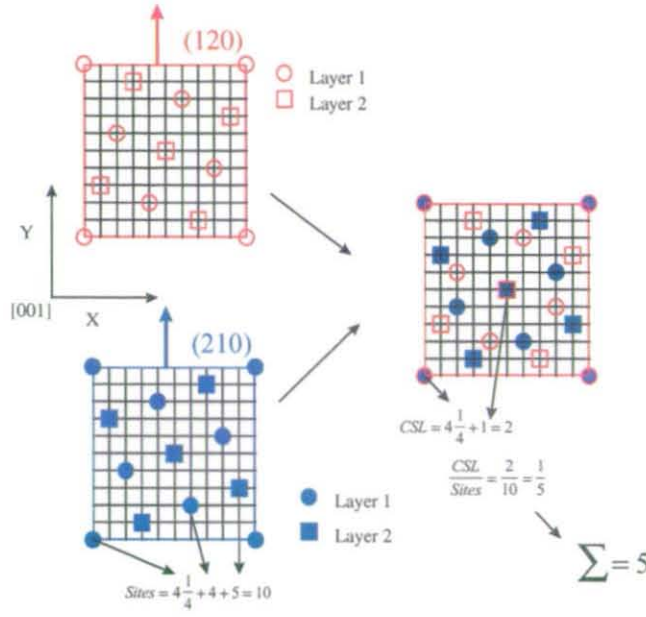
Figure 4.4: Schematic representation of the coincidence site lattice parameter, Σ. Squares and circles represent atomic sites in adjacent planes perpendiclar to the [001] direction.

perpendicular. In the side view of Figure 4.5 a dotted line separates the upper and bottom crystals forming the interface. Only four atomic layers, i.e. the two closest atomic layers of each crystal, are plotted with different symbols. The projection of atomic sites onto the grain boundary plane leads to periodic structures similar to moiré patterns [83]. Periodic structure and misorientation angle are also drawn in Figure 4.5.

It should be noticed that the separation between crystals, in tilts or twist models based in a coincident site lattice model are initially chosen to be the same as the interlayer distance of planes parallel to the boundary. This is done in order to maintain the atomic density of the perfect crystal.

Asymmetric twist boundaries are the most general boundaries and the whole set of macroscopic degrees of freedom are needed for their description. An asymmetric twist boundary is an asymmetric tilt boundary that has been subjected to a further twist about the boundary normal.

It is also useful to specify the five macroscopic degrees of freedom in a way which focuses attention more on the interface plane normal in both crystals rather than the relationship between the crystals [36]. This is the so-called interface-plane scheme
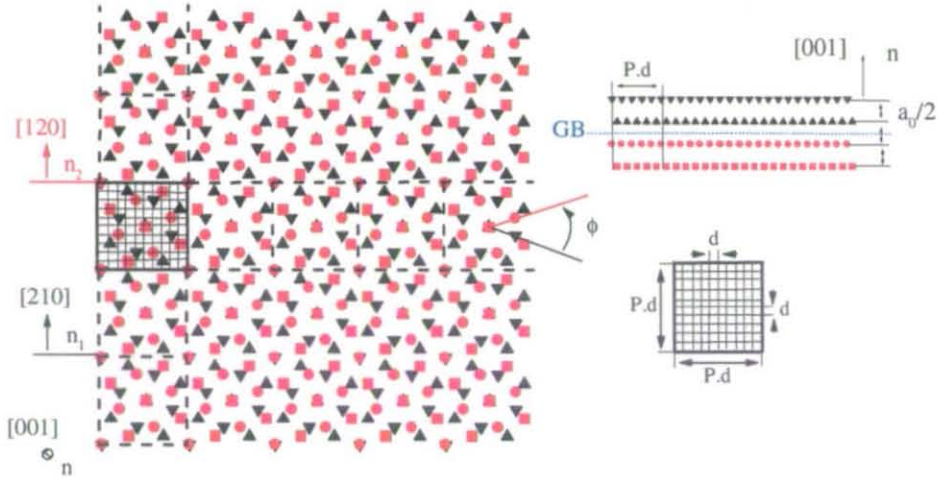
Figure 4.5: Projection along the rotation axis, i.e. top view, [001] coming out of the page, of a (210) symmetrical twist grain boundary. Values of the misorientation angle, interlayer distance and period are $\phi = 36.87°$, $d = 0.64$ Å and $P = 10$. The top right hand figure shows a projection perpendicular to the boundary, i.e. side view, of the two closest atomic planes to the boundary in each crystal. Different colours represent atoms at different crystals and different symbols represent atoms at different atomic layers.

[114]. The interface-plane scheme chooses the two boundary normals of both bicrystals and a twist angle as the five geometrical parameters which define the orientation of the two halves. The creation of an interface can be viewed as the sum of two operations: first bring together two crystal free surfaces with normals $\hat{n}_1$ and $\hat{n}_2$, into contact and secondly a rotation, θ_{twist}, about their common normal, $\hat{n}$, referred to the same principal coordinate system, see Figure 4.6 . So the five macroscopic degrees of freedom in the misorientation scheme $\{\hat{n}_1, \hat{n}_2, \theta_{twist}\}$, are defined by the unitary normal vectors $\hat{n}_1$ and $\hat{n}_2$, and the twist rotation, θ_{twist}. Following the interface-plane scheme symmetric grain boundaries are defined by the condition that $\hat{n}_1 = \pm \hat{n}_2$.

For practical reasons the CSL scheme is suited for the description of dislocation grain boundaries, i.e. low angle, whilst the interface-plane scheme is best suited for the description of high-angle grain boundaries [115], however both are complementary and related. The relationship between the CSL and misorientation geometrical sets of parameters can be found elsewhere [114].

4.2.2 Computational blocks

The procedure used to build an initial computational block containing a symmetrical grain boundary was based on the CSL definition. The implementation of the com-
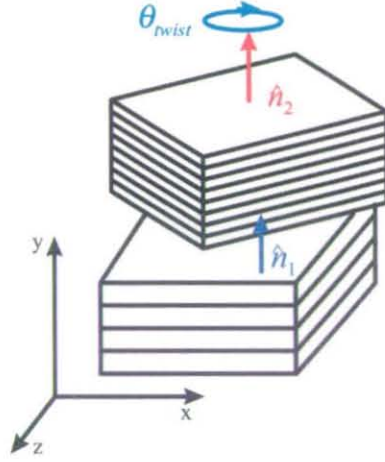
Figure 4.6: Geometrical parameters involved in the interface-plane scheme.

putational block, i.e. FORTRAN code, was mainly reduced to four steps because of the symmetry of the interfaces studied, i.e. symmetrical tilt and twist boundaries.

In Figure 4.7 the procedure to build both symmetrical tilt and twist boundaries is schematically presented. Firstly, a block of atomic sites (three-dimensional coordinates of lattice sites) was generated following a perfect bcc structure, Figure 4.7 (a). Secondly, two other bcc structures were created by a rotation of the initial one. The first new block was created by a rotation of the bcc lattice sites of half the misorientation angle required, $\phi/2$, about a rotation axis, $\hat{n}$, which goes through the middle of the block on the [001] direction following equations 4.1 and 4.2. The second block was made by a rotation of the initial bcc structure of half the misorientation angle but in an anticlockwise sense, $-\phi/2$, about the same rotation axis. The final result of the second step was two interpenetrating lattices which were centred but with different orientations, Figure 4.7 (b). The third step, was to extract from this double pattern a rectangular block with the desired dimensions for the simulation block, Figure 4.7 (c). Related to this step is the size of the initial bcc block, because the initial block has to be big enough to create, after rotation, a double structure from which the desired computational block can be extracted.

Finally, from the rectangular double patterned block, either a symmetrical tilt or twist boundary can be made. To create a symmetrical tilt boundary, the rectangular computational block was first divided by an auxiliary plane parallel to the rotation axis and then, only atoms coming from one of the rotated structures, were removed
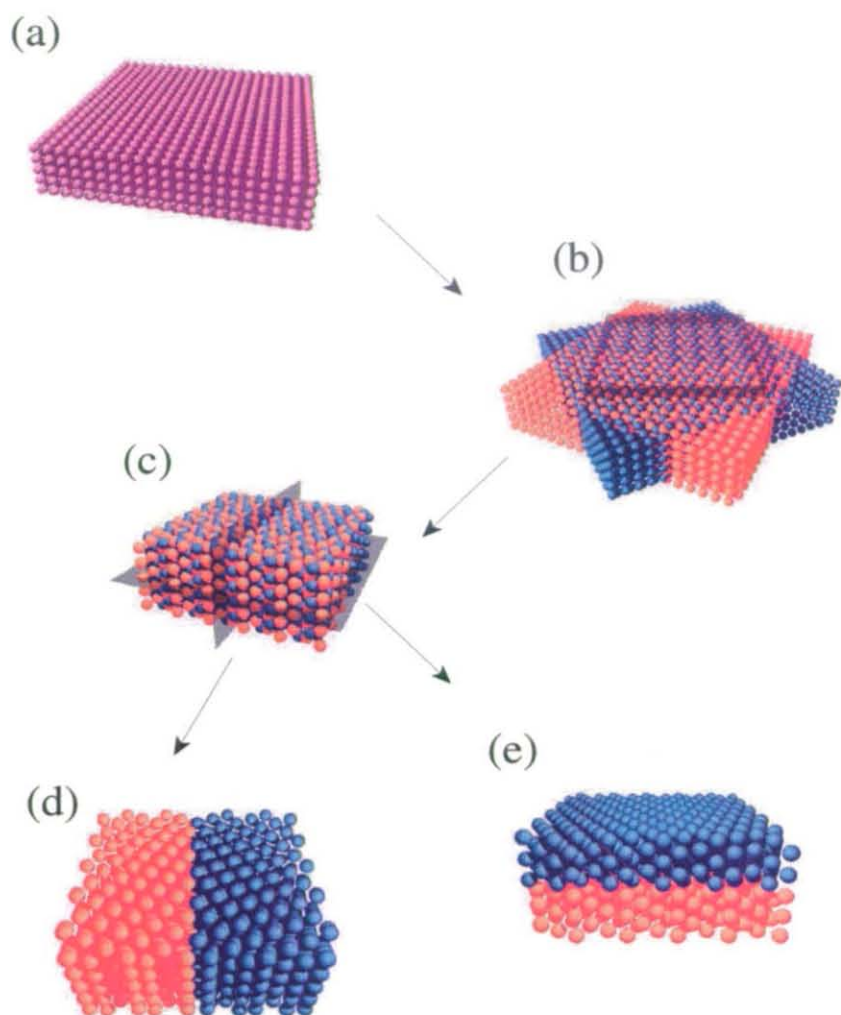
Figure 4.7: Building a computational block containing a symmetrical grain boundary. (a) Initial bcc structure. (b) Two rotated bcc structures. Grey box indicates which region is extracted. (c) Double patterned block. Vertical grey plane indicates the separation for a symmetrical tilt, and the horizontal plane, the symmetrical twist. (d) Symmetrical tilt boundary. (e) Symmetrical twist boundary. Red and blue spheres belong to the initial bcc structures rotated $\phi/2$ and $-\phi/2$ respectively.

on one side of the plane, whereas atoms coming from the other block, were removed on the other side, Figure 4.7 (d). In order to create a symmetrical twist boundary, the auxiliary plane was chosen at the middle of the rectangular computational block and perpendicular to the rotation axis, and following the same procedure as for the tilt boundary, i.e. atoms were removed in each side of the bicrystal, see Figure 4.7 (e). The final result was a rectangular computational block with two bicrystals either on a symmetrical tilt or twist configuration with the interface in the middle of the computational cell. For convenience, the interface was chosen parallel to the x and z directions.

Periodic boundary conditions just on planes parallel to the boundary were applied during the relaxation procedure, because of the two-dimensional nature of the grain boundaries. In this way, an 'infinite' grain boundary, e.g. extended defect in two dimensions, is modelled. Care was taken in choosing the sizes of the computational blocks to include a number of layers proportional to the periodicity of the planes on the x and z direction, i.e. parallel to the boundary, in order to apply periodic boundary conditions. Free boundary conditions were applied on the perpendicular direction of the boundary plane allowing expansion of atomic layers in this direction. The computational cell was chosen big enough in order to avoid possible surface effects on the bulk interface.

4.2.3 Relaxation procedure

The initial structure is assumed to be at 0 K, but contains an excess of potential energy. The initial but unrelaxed structure is allowed to evolve until the block reaches a minimum energy configuration at a given temperature using classical molecular dynamics (MD). In order to represent the interaction between iron atoms, a many-body potential for α-iron of the Finnis-Sinclair form has been used [37] (see Chapter 2). During the relaxation procedure the atoms will rearrange, seeking an optimal configurational structure of the system with minimum potential energy. The atoms close to the interface will be the ones that will change position the most, see Figure 4.8.

The relaxation procedure was to run the MD simulation for approximately 3-5 ps depending on the speed of the rearrangement process. Figure 4.9 shows the typical evolution of the kinetic, potential and total energy of the system as a function of the time. As can be seen from Figure 4.9, at the beginning of the simulation the kinetic energy of the system increases suddenly, with the potential energy decreasing. Atoms are moving increasing the kinetic energy and rearranging in a more optimal
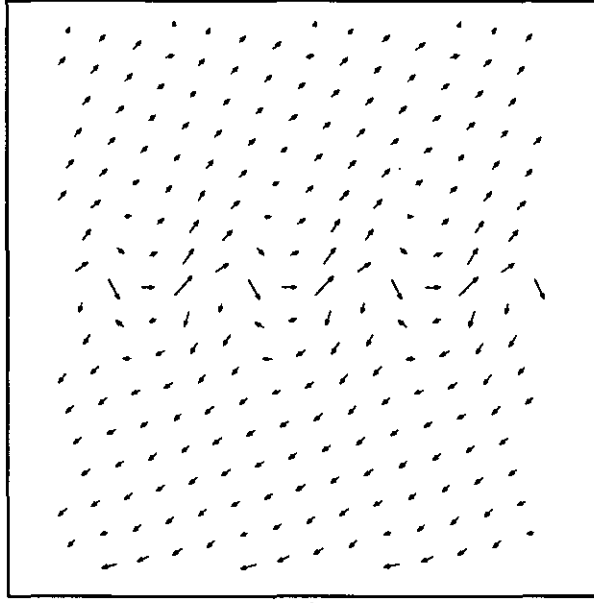
Figure 4.8: Vector plot showing a typical atomic rearrangement during the relaxation procedure from a initial CSL description of a symmetrical tilt grain boundary. The arrows point from the unrelaxed to the relaxed configuration. View along the rotation axis of an initially unrelaxed (210) symmetrical tilt boundary.

distribution in such a way that they reduce the potential energy of the system. After a few femtoseconds, the system reaches a much more stable situation where there are small fluctuations of kinetic energy and potential energy. After, typically 3 ps, the system is considered structurally stable enough to 'freeze' the atoms, and extract excess kinetic energy. For the 'freezing' process, a damping term proportional to the velocity is applied to the system, reducing the kinetic energy of the system as implemented in References [116, 117]; also the potential energy and the total energy decrease during this process. The simulation was run for another typically 10 ps for a crystal containing 40,000 atoms until the temperature dropped to approximately 10 K and the equilibrium configuration at this temperature was reached. The final temperature of the system, calculated from the mean kinetic energy of the atoms, was chosen for practical (computational) reasons. The kinetic energy of the system decreases following an exponential decay due to the damping imposed on the velocity of the atoms, therefore decreasing of temperatures when the system has low kinetic energy requires longer computational times.

Different choices of time step have been considered during the relaxation procedure according to the stage of the simulation as follows: $\Delta t = 0.5$ fs for $t < 0.1$ps, $\Delta t = 1$ fs
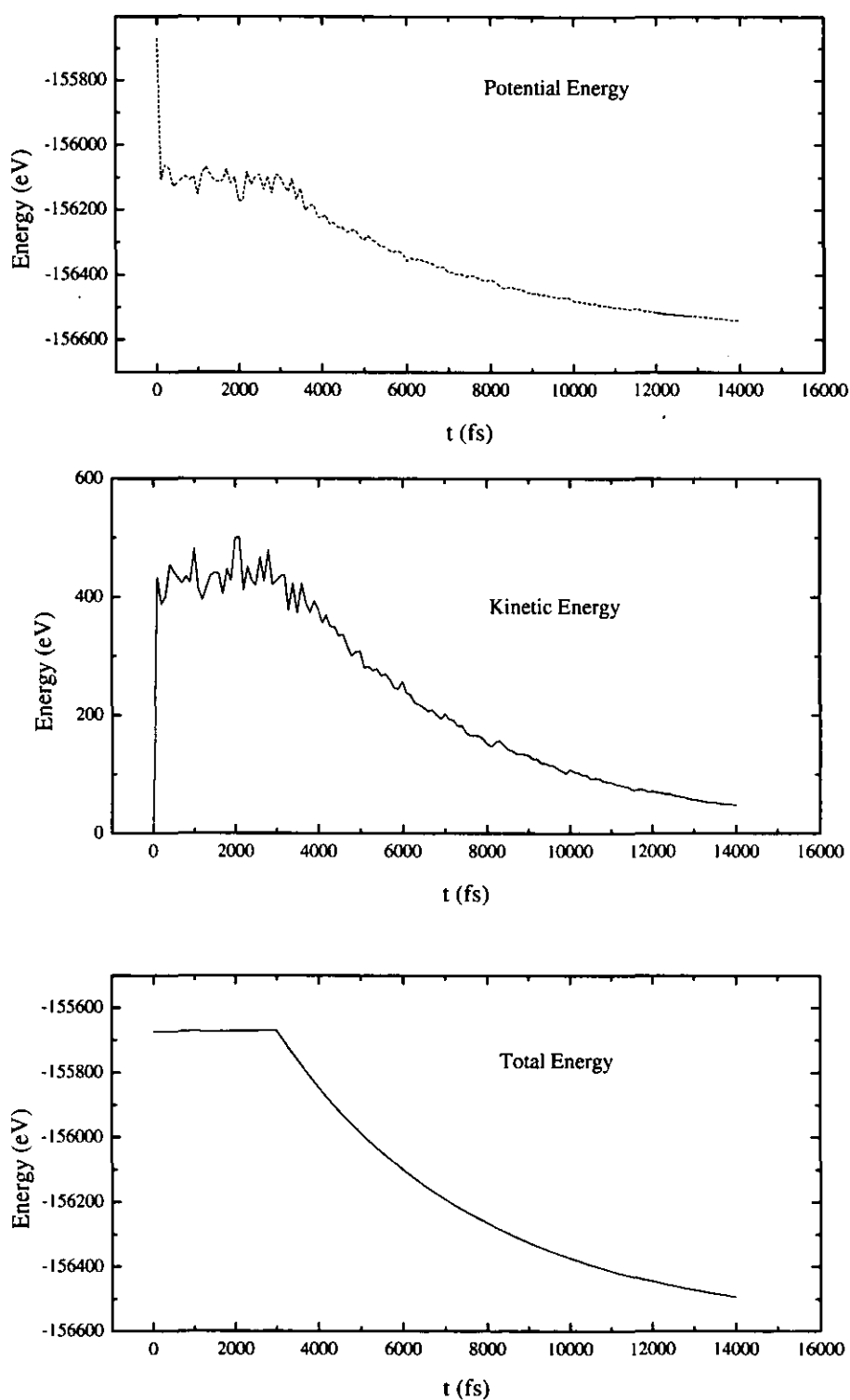
Figure 4.9: Typical potential, kinetic and total energy evolution during the relaxation procedure. The values plotted correspond to a (530) symmetrical tilt grain boundary in a computational block of dimensions $100 \times 100 \times 42\text{Å}$ containing 36900 atoms.

for $0.1 < t < 1 \mathrm{ps}$ and $\Delta t = 2 \mathrm{fs}$ for times greater than $1 \mathrm{ps}$. The total energy is conserved previous to the damping process, with this choice of the time-step, with fluctuations in the total energy, $\Delta E/E$, not bigger than 0.001 %.

We have to take into account that in the final relaxed structure a residual kinetic energy is always present, e.g. the final temperature equals 10 K. Therefore the final block has a residual kinetic energy equal to $E_k^{gb} = \frac{3}{2}NkT$, where k is the Boltzman's constant. This low residual kinetic energy will not affect the structure of the grain boundaries but it will play a role in the calculation of the grain boundary energy in terms of size effects. The configuration at 0 K of the grain boundary can be considered as the same than at 10 K, because a temperature of 10 K only represents the kinetic energy of the vibrational states of the atoms.

4.2.4 Rigid body translation

The structure generated following the coincident site parametrisation can be used as a starting point of a relaxation procedure. However, the coincidence model, due to its only geometrical basis, will produce structures with overlaps of crowding atoms in the boundary plane giving an unphysical high energy to the system. Generally, for symmetrical boundaries, a more stable initial configuration, less configurational energy, can be obtained by a rigid body translation of one of the crystal respect to the other from the coincident site description. In this way the periodicity of the boundary will be maintained but, generally, there will not be more coincident sites of the bicrystal. Rigid body translations of one grain relative to the other have been experimentally found by HREM studies [69]. Rigid body translations have been applied in this thesis to the initial CSL model of grain boundaries. Several new starting unrelaxed configurations can been obtained in this way. This new starting configurations can be closer to a low-energy configuration state.

In Figure 4.10, a view along the rotation axis, $\hat{n}$, of an [001] 36.87° (210) symmetrical tilt boundary is shown. In Figure 4.10, solid and open circles represent atoms on adjacent planes perpendicular to the rotation axis. The directions of the rotation axis, $\hat{n}$, chosen parallel to the z-axis, is out of the page. The atoms close to the mirror atomic plane, indicated by arrows on Figure 4.10 (a), will make this configuration unstable, this instability being more noticeable in symmetrical models with small interlayer distance between planes perpendicular to the boundary plane. The strong repulsion that these atoms close to the boundary may suffer, can be avoided by a displacement of the upper crystal along the x axis, T_x, parallel to the boundary. A more stable configuration is reached after the displacement, i.e. atoms close to the

boundary plane have a greater separation, see atoms marked with arrows in Figure 4.10 (b). If a displacement, T_x, is equal to the periodicity length of the plane in the x axis, $P.d$, the same configuration is obtained. The periodic unit of the structure in each bicrystal is also shown in Figure 4.10 by the green coloured squares.
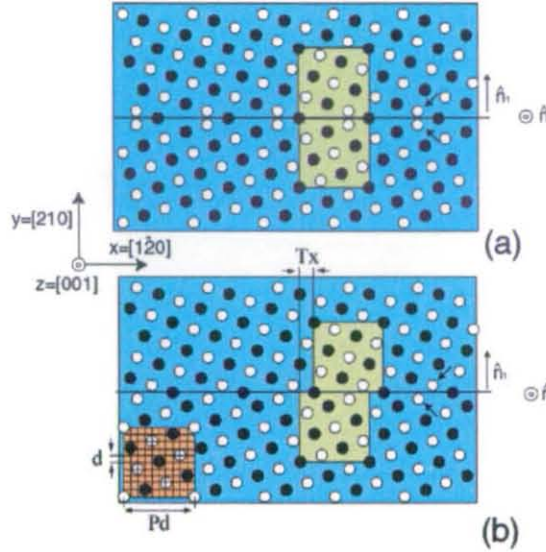

Figure 4.10: Rigid body translation on a dimension parallel to the boundary, T_x, for a (210) symmetrical tilt boundary.

In Figure 4.11 the total potential energy of the atoms in a unrelaxed computational block with a (210) symmetrical tilt boundary as a function of the rigid body translation parallel to the boundary plane, T_x, is shown. In Figure 4.11, energy is given in units relative to the energy of the block without shift and the displacement is given in periodicity units of the structure on the x direction. For this symmetrical boundary, a local minimum of energy on the unrelaxed configuration is obtained by a displacement equal to $T_x = 0.2$. This structure can be used as an initial structure for the relaxation procedure.

A more efficient way to find an initial minimum unrelaxed structure is to examine also rigid body translations on the z direction, T_z. This direction is also parallel to the boundary plane in our coordinate system. For every displacement in x, also displacements in z are taken into account and the configurational energy is calculated. In Figure 4.12 equipotential energy lines, in arbitrary units, are shown as a function of both displacements, T_x and T_z, for a (210) symmetrical tilt boundary. An initial
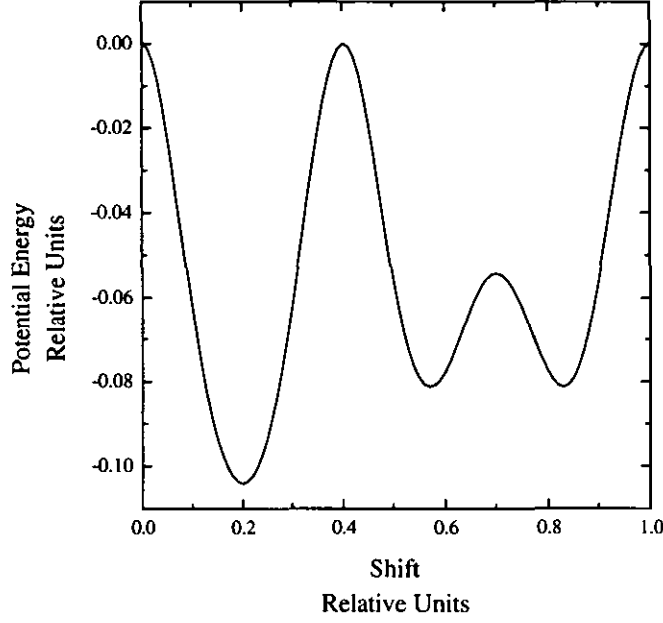
Figure 4.11: Unrelaxed potential energy as a function of a rigid body translation on the x direction parallel to the boundary for a (210) symmetrical tilt boundary.

configuration with no displacement in any of the direction parallel to the boundary plane, $T_x = 0$ and $T_z = 0$, corresponds to the perfect bicrystal built following the coincident site lattice definition. As we see in Figure 4.12, the minimum of energy obtained by this procedure, corresponds to a displacement of $T_x = 0.2$ or $T_z = 0.5$. Also we observe that a displacement of $T_x = 0.2$ and $T_z = 0$ corresponds to a local minimum of the unrelaxed energy. These three different choices of initial structure were relaxed to obtain the final configuration. The unrelaxed energy configuration of all the boundaries studied have been calculated as a function of both displacement x and z parallel to the boundary plane. The local minima of the unrelaxed structures of the [001] symmetrical tilt boundaries usually appear for $T_z = 0$ and $T_z = 0.5$.

In Figure 4.13 equipotential energy lines, in arbitrary units, are shown as a function of rigid body displacements parallel to the boundary plane for a (210) symmetrical twist boundary. In this case, differences between unrelaxed energies after a rigid body displacement are almost negligible though small differences can be found for certain displacements as indicated in Figure 4.13. This is due to that the interlayer distance on the twist boundaries studied, with the rotation axis along the [001] direction, is equals to $a_0/2 = 1.43$Å which is more than twice the interlayer distance between planes in the boundary for the (210) symmetrical tilt, 0.64Å. For this interlayer distance atoms at the interface in a CSL arrangement do not suffer strong repulsions as the case already explained for a (210) tilt boundary in Figure 4.10.
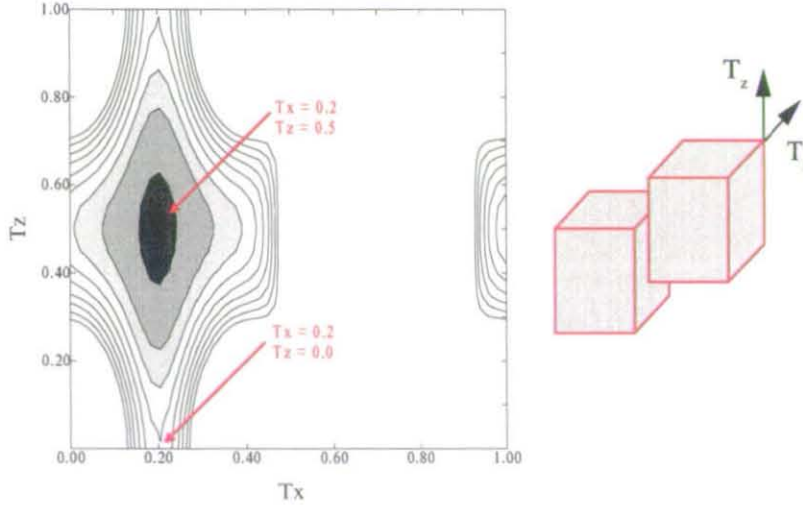
Figure 4.12: Unrelaxed potential energy as a function of a rigid body translation on the x and z dimension parallel to the boundary plane for a (210) symmetrical tilt boundary. The shaded regions corresponds to low potential energy values.

The rigid body displacement of minimum unrelaxed configurational energy will lead to the final relaxed structure faster than the others. Different choices of initial structures can lead to a different final structures after relaxation and all of them will be local minima of energy. In Figure 4.14, the relaxed and unrelaxed configuration energy of a (530) symmetrical tilt boundary is presented as a function of different rigid body translations in the x direction. This brief study shows how local minima of unrelaxed structures will reach minima of relaxed structures.

In this thesis we use structures with local minima in the configurational energy of the unrelaxed structures as a function of the translation vectors, as a starting point for the relaxation procedure, as explained before.

4.3 Atomic structure of grain boundaries

4.3.1 Symmetrical tilt grain boundaries

In this section the atomic structures of several high angle symmetrical tilt grain boundaries in α-iron are described. The geometrical description of the tilt boundaries studied in this thesis is presented in Table 4.1. This table gives the Miller indexes of the boundary planes of each crystal at the interface, $\hat{n}_1$ and $\hat{n}_2$, the misorientation angle, ϕ, the coincidence site lattice parameter, Σ, the periodicity, P, and the interlayer distance between parallel planes, d. The coordinate system is chosen, for convenience, with x and z axes parallel and y axis perpendicular to the boundary
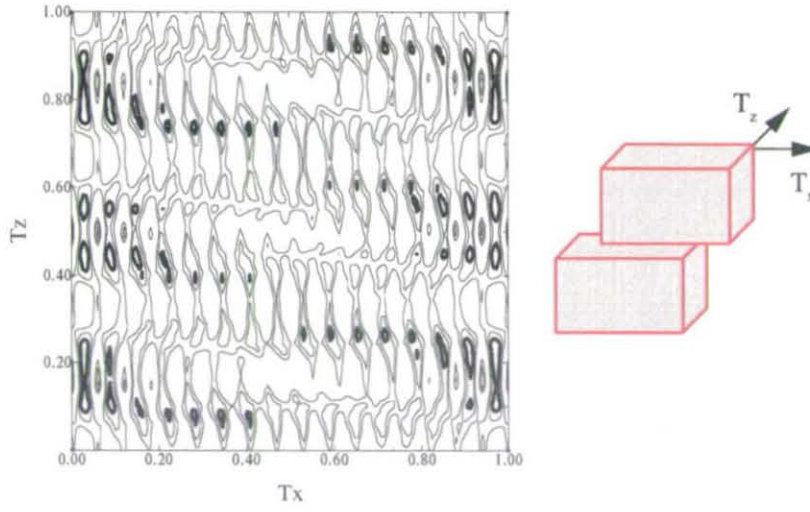
Figure 4.13: Unrelaxed potential energy as a function of a rigid body translation on the x and z dimension parallel to the boundary plane for a (210) symmetrical twist boundary. The shaded regions corresponds to low potential energy values.
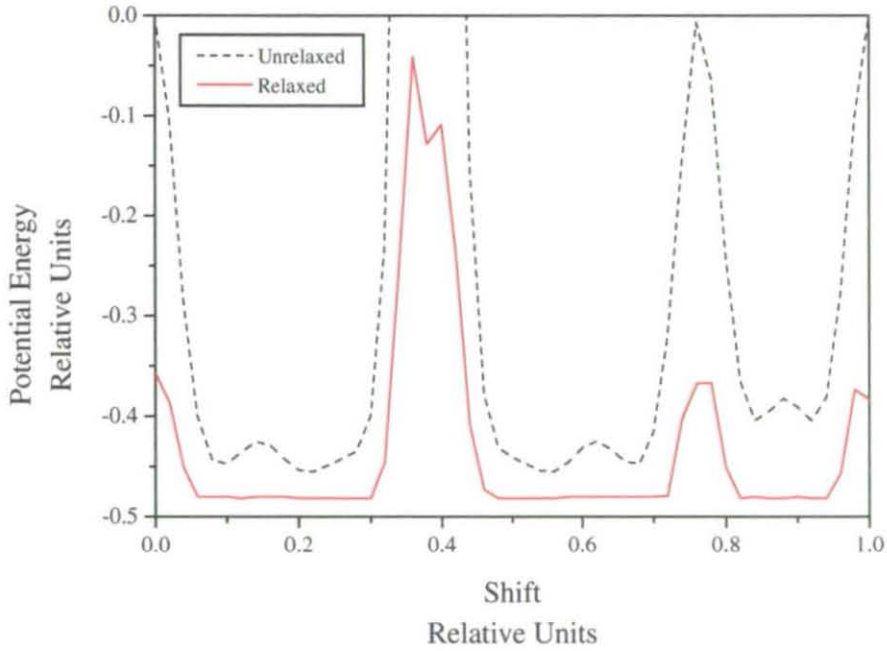

Figure 4.14: Relaxed and unrelaxed potential energy of the structures generated by a shift, T_x, parallel to the boundary, for a [001] 36.87° (530) symmetrical tilt boundary, with $T_z = 0$.

plane respectively. The periodicity and the interlayer distance on the symmetrical tilt models are the same on the x and y directions of our coordinate system. 15 different symmetrical tilt boundaries have been considered, all of them with the rotation axis on the [001] direction, z-axis. These boundaries have been chosen in order to have a homogeneous representation of high angle grain boundaries. In particular, these boundaries have the lowest Miller index combination of the planes normal to the interface.

GB Planes	ϕ (degrees)	$\sum$	$P_{x,y}$	$d_{x,y}$ (Å)
$(540)_1/(450)_2$	12.68	41	82	0.22384
$(430)_1/(340)_2$	16.26	25	50	0.28665
$(320)_1/(230)_2$	22.62	13	26	0.39751
$(530)_1/(350)_2$	28.07	17	34	0.49160
$(740)_1/(470)_2$	30.51	65	130	0.17777
$(210)_1/(120)_2$	36.87	5	10	0.64095
$(520)_1/(250)_2$	46.40	29	58	0.26615
$(830)_1/(380)_2$	48.89	73	146	0.16775
$(310)_1/(130)_2$	53.13	5	10	0.90647
$(720)_1/(270)_2$	58.11	53	106	0.19687
$(410)_1/(140)_2$	61.93	17	34	0.34761
$(920)_1/(290)_2$	64.94	85	170	0.15546
$(510)_1/(150)_2$	67.38	13	26	0.56217
$(710)_1/(170)_2$	73.74	25	50	0.40538
$(910)_1/(190)_2$	77.32	41	82	0.31655

Table 4.1: Geometrical parameters describing the symmetrical tilt grain boundaries studied. The rotation axis is on the [001] direction.

According to the parameters given in Table 4.1 rectangular computational blocks for each model are made. The size and the number of atoms included in each computational block is given in Table 4.2. All the symmetrical tilt grain boundaries studies have the rotation axis, z direction, on the [001] direction. As has been said in previous sections, the computational blocks are chosen large enough in the direction perpendicular to the boundary, the y direction, in order that surface effects do not affect the bulk interface. Sizes of the computational blocks in the x and z directions, i.e. parallel to the interface, are chosen by periodicity considerations. The number of layers in the x direction, along the boundary, is at least four times the periodicity in this direction. The size of the computational block in this direction is big enough to 'observe' the repeated structures of the boundary. The periodicity in the [001] direction of a bcc lattice, which is the z direction in our coordinate system, is equal to two and the interlayer distance is equal to $a_0/2$, where a_0 is the lattice constant

in α−iron which is equal to $a_0 = 2.8665$ Å. Therefore the size of the z dimension does not need to be large compared with the other dimensions, but large enough to build a neighbour list for each atom. The length of the computational block on the z dimension is 42.0 Å for all the models, having in this way a reasonable number of atoms on each computational cell according to the computational resources available. The number of atoms involved in the simulations are in the range of 28000-44000 atoms. Additionally computational blocks with different sizes from those presented in Table 4.2 were also simulated for testing purposes.

GB Planes	Size (Å) (X×Y×Z)	Atoms	T_x	T_z
$(540)_1/(450)_2$	$91.8 \times 128.5 \times 42.0$	43125	0.0	0.5
$(430)_1/(340)_2$	$71.7 \times 129.1 \times 42.0$	33825	0.19	0.0
$(320)_1/(230)_2$	$103.5 \times 103.5 \times 42.0$	39150	0.06	0.5
$(530)_1/(350)_2$	$100.5 \times 100.5 \times 42.0$	36900	0.21	0.0
$(740)_1/(470)_2$	$92.5 \times 115.6 \times 42.0$	39060	0.76	0.5
$(210)_1/(120)_2$	$103.0 \times 103.0 \times 42.0$	38640	0.2	0.5
$(520)_1/(250)_2$	$77.2 \times 139.0 \times 42.0$	39225	0.79	0.0
$(830)_1/(380)_2$	$98.0 \times 122.5 \times 42.0$	43860	0.04	0.5
$(310)_1/(130)_2$	$109.0 \times 109.0 \times 42.0$	43560	0.07	0.0
$(720)_1/(270)_2$	$83.5 \times 104.4 \times 42.0$	31860	0.28	0.0
$(410)_1/(140)_2$	$94.6 \times 94.6 \times 42.0$	32760	0.39	0.0
$(920)_1/(290)_2$	$105.8 \times 105.8 \times 42.0$	40860	0.04	0.5
$(510)_1/(150)_2$	$88.0 \times 88.0 \times 42.0$	28260	0.58	0.0
$(710)_1/(170)_2$	$81.1 \times 101.4 \times 42.0$	30120	0.57	0.0
$(910)_1/(190)_2$	$103.9 \times 103.9 \times 42.0$	39480	0.54	0.0

Table 4.2: Dimension and number of atoms of computational blocks containing the symmetrical tilt grain boundary models studies. The rigid body translations, T_x and T_z, which lead to the minimum energy structure, are also presented

For each model, different initial starting structures were considered. These structures are basically the local minima obtained by the studies of the unrelaxed configurational energy as a function of rigid body displacement of one of the grains in a plane parallel to the interface, as explained in the previous section. The relative stability of the grain boundaries for each grain boundary is based on a comparison of the final relaxed configurational energy of the atoms in the system. The structure with lowest configurational energy for every model, will be the equilibrium configuration whereas the others, will be considered as metastable structures. The rigid body translation parallel to the boundary which gives a minimum of configurational energy after relaxation are also given in Table 4.2 for each model. The displacements T_x and T_z, are given in units of the periodicity length, $P.d$, for each boundary. On

the other hand, in order to compare configuration energies between different grain boundaries, the grain boundary energy will be defined in the next section.

Figures 4.15 and 4.16 show the equilibrium structures for the (530) and (210) symmetrical tilt grain boundaries respectively. Two different close views of the final relaxed grain boundary structure for each model are presented in each figure. Figures 4.15 (a) and 4.16 (a) show the boundary viewed along the rotation axis, i.e. [001] direction, solid and open circles represent atoms in two adjacent layers perpendicular to the rotation axis. Figures 4.15 (b) and 4.16 (b) show a view of the boundary parallel to the boundary plane, i.e. parallel to the $x - z$ plane.

The main features of the equilibrium structures for all the symmetrical tilt boundaries studied can be inferred from the two representative models showed in Figures 4.15 and 4.16. From this figures it can be seen that the regular structure of the crystal is broken in a few layers close to the boundary in a region which can define the width of the interface, being the basic bcc structure of each bicrystal is maintained after relaxation away from the boundary region. A simple definition for the width of a grain boundary will be given later in this chapter. The bicrystal, after relaxation, has generally a specular symmetry across the boundary plane, normally being the 'mirror' plane an atomic layer. The periodicity in directions parallel to the planes at the boundary is maintained. In the [001] direction, i.e. z axis, the structure of the relaxed configuration is repeated every two layers, mantaining the original periodicity of the bcc structure in this direction but with a different structure at the boundary region. The periodicity in the x direction , i.e. $(3\bar{5}0)$ and $(1\bar{2}0)$, is the same as the one in the initial structure, but with a different repeated structure which is characteristic of each boundary; this repeated structure is marked with a solid line in these figures. Also, in Figures 4.16 (b) and 4.15 (b), it can be clearly seen the expansion suffered by atomic layers close to the interface on direction perpendicular to the interface plane. This expansion will be discussed later in this chapter.

In Figures 4.17, 4.18 and 4.19 the final equilibrium structures for the symmetrical tilt boundaries studied, viewed in a projection along the rotation axis, are presented. Open and solid circles represent atoms in adjacent layers perpendicular to the rotation axis. The rigid body translations for the final configurations presented in Figures 4.17, 4.18 and 4.19 which leads to the final relaxed structures with minimum configurational energy are specified in Table 4.2. The most noticeable characteristic of these relaxed structures is that there exist an atomic arrangement, typical of every interface, which is repeated along the boundary. This repeated 'structural units' are marked with a solid line in these figures for each boundary. The structural units have a periodicity
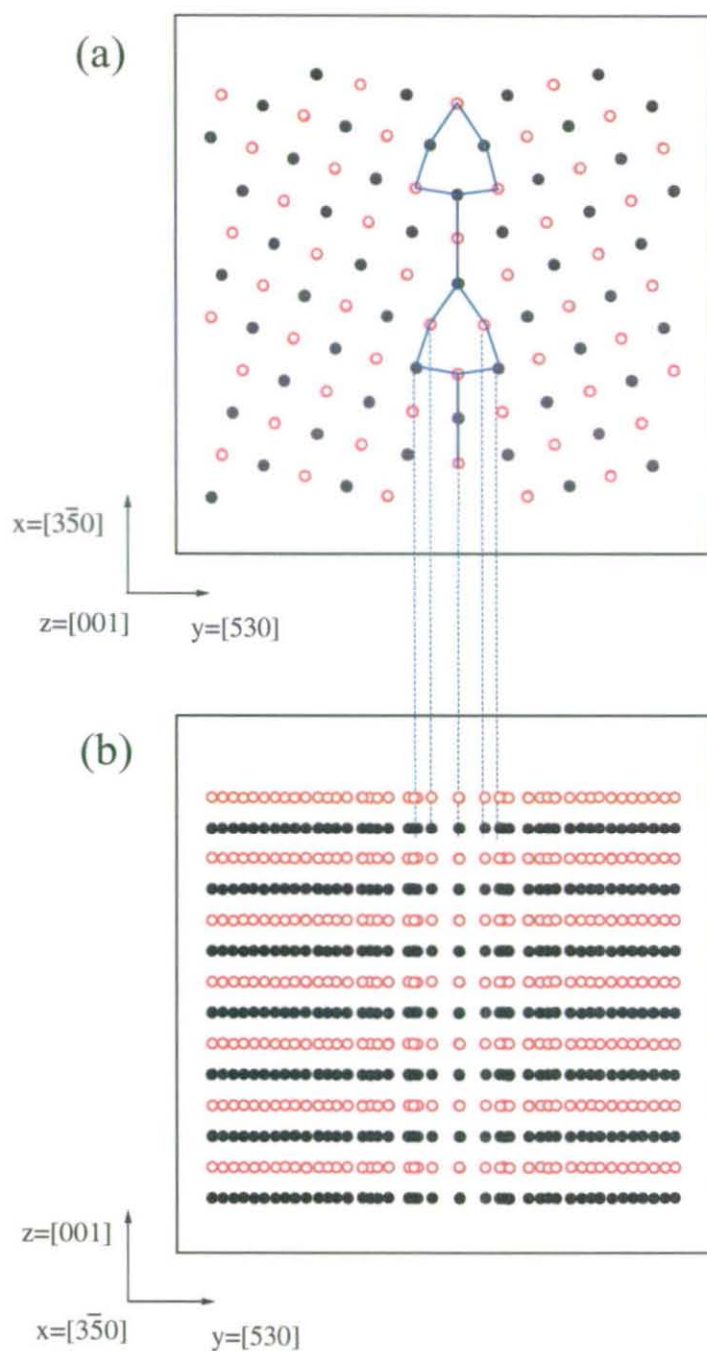
(a)

x=[3$\bar{5}$0]

z=[001]   y=[530]

(b)

z=[001]

x=[3$\bar{5}$0]   y=[530]

Figure 4.15: Relaxed structure of a (530) symmetrical tilt grain boundary. (a) Top view. Atoms projected to a plane perpendicular to the rotation axis. (b) Front view. Atoms projected to a plane perpendicular to the grain boundary and parallel to the rotation axis. Open and solid circles represent atomic sites in two adjacent layers along the rotation axis.

(a)

x=[1$\bar{2}$0]

z=[001]   y=[210]

(b)

z=[001]
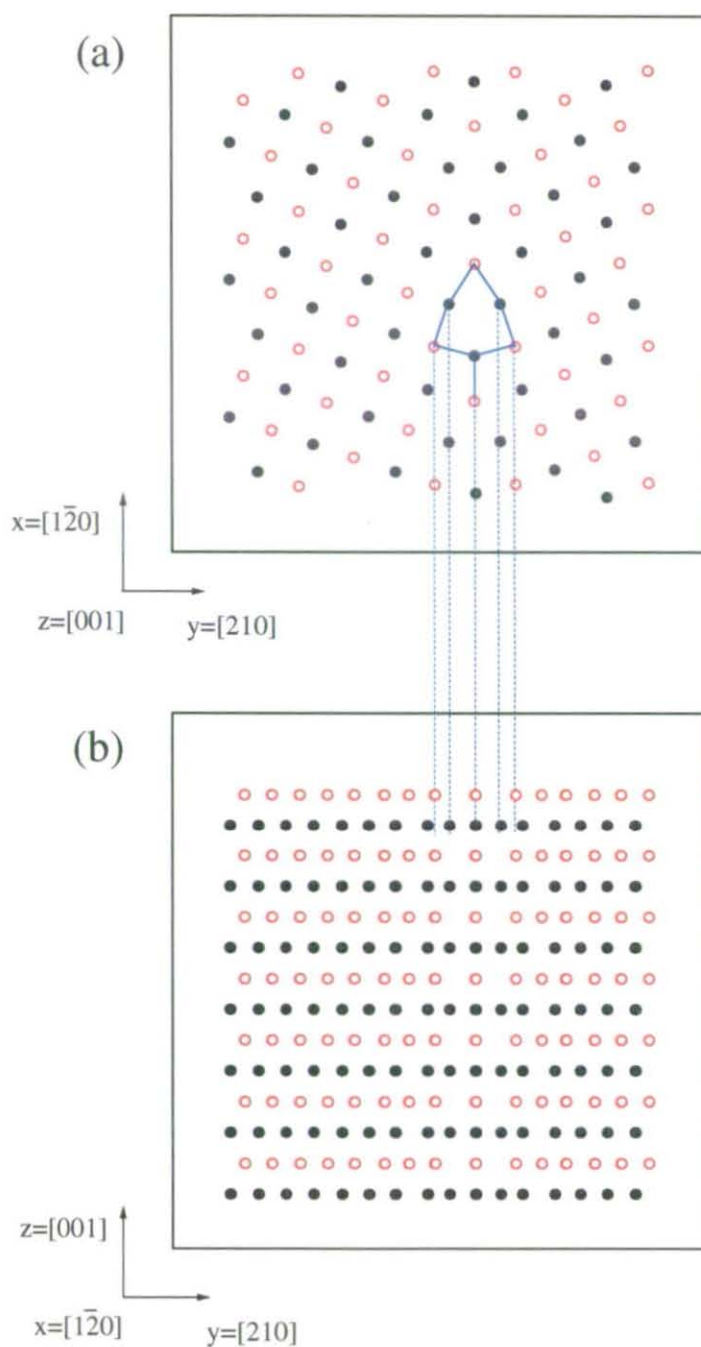
x=[1$\bar{2}$0]   y=[210]

Figure 4.16: Relaxed structure of a (210) symmetrical tilt grain boundary. Top view. Atoms projected to a plane perpendicular to the rotation axis. (b) Front view. Atoms projected to a plane perpendicular to the grain boundary and parallel to the rotation axis. Open and solid circles represent atomic sites in two adjacent layers along the rotation axis.

(a) [001] 12.68°(540)

(b) [001] 16.26°(430)

(c) [001] 22.62°(320)

(d) [001] 28.07°(530)

(e) [001] 30.51°(740)

(f) [001] 36.87°(210)

Figure 4.17: Symmetrical tilt relaxed structures. Open and solid circles represent atomic sites in two adjacent layers along the rotation axis.

(a) [001] 46.40° (520)

(b) [001] 48.89° (830)

(c) [001] 53.13° (310)

(d) [001] 58.11° (720)

(e) [001] 61.93° (410)
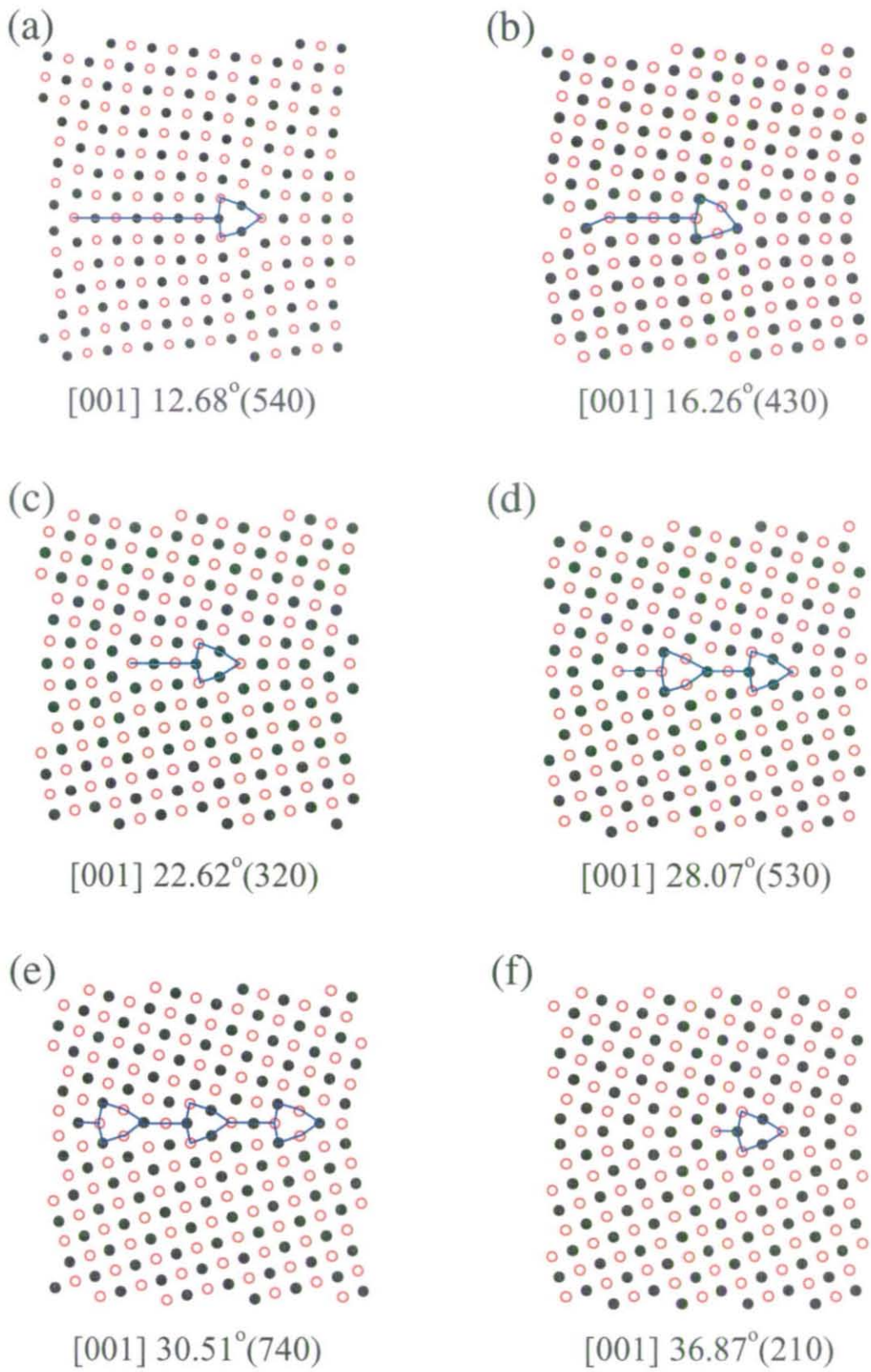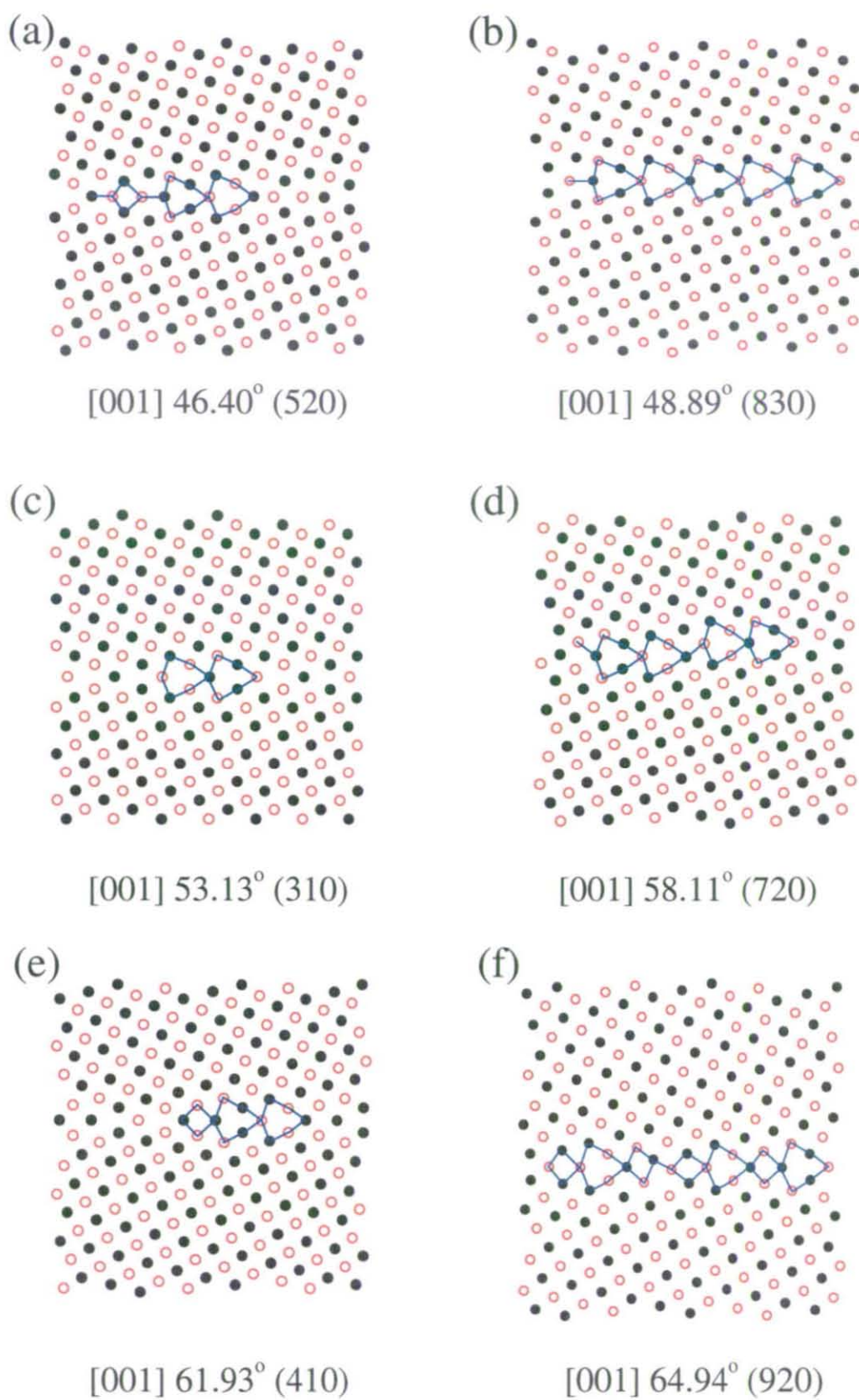
(f) [001] 64.94° (920)

Figure 4.18: Symmetrical tilt relaxed structures. Open and solid circles represent atomic sites in two adjacent layers along the rotation axis.
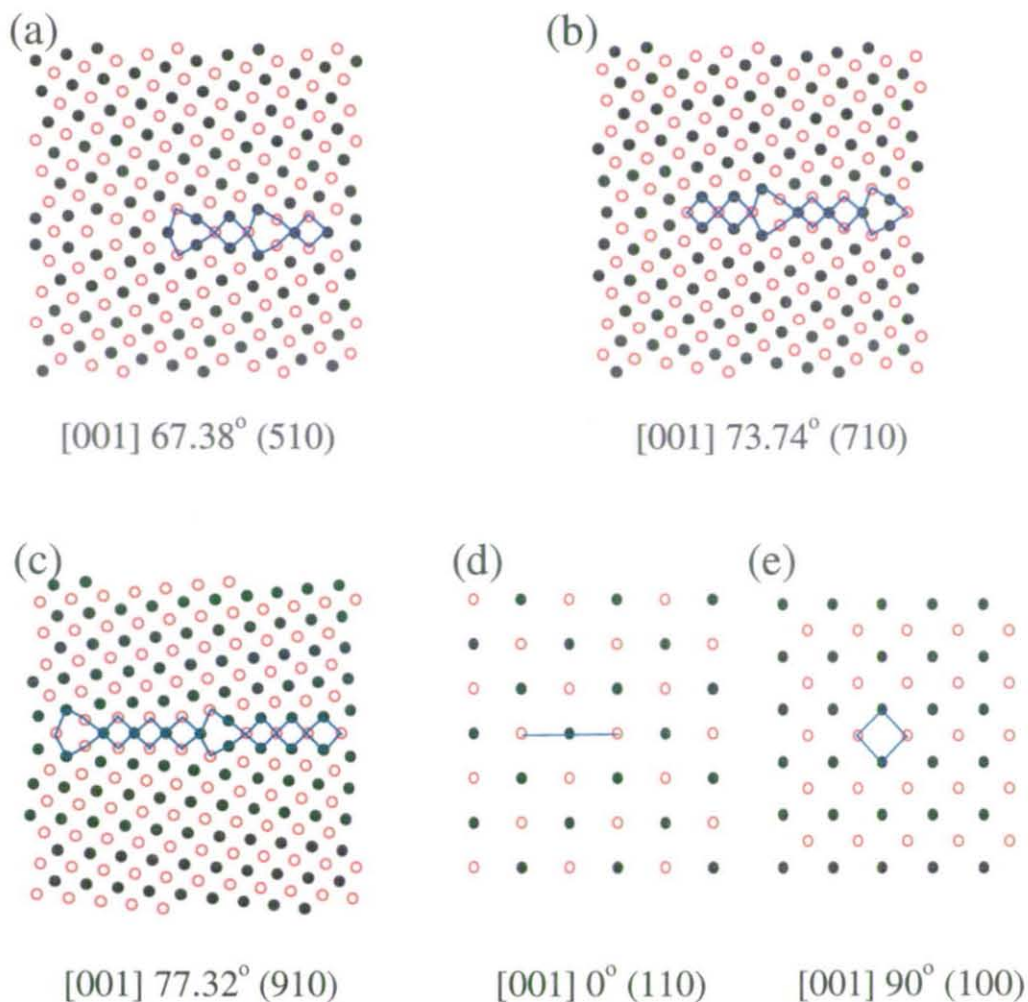
Figure 4.19: Symmetrical tilt relaxed structures. Open and solid circles represent atomic sites in two adjacent layers along the rotation axis.

length equal to the periodicity of the planes normal to the interface in the unrelaxed CSL model.

In Figures 4.20 and 4.21 a magnification of the structural units that appear for each model is presented. The periodicity length of the structural units is also shown in these figures. Basically, the structural units of the symmetrical tilt boundaries are composed of a combination of three 'basic' units. The three basic units are the ones that appear in 'singular' boundaries, i.e. they are composed of only one type of structural unit, which are the (310), (100) and (110) symmetrical tilt models.

As can be seen from Figure 4.21(a), one period of the (310) symmetrical tilt boundary is composed of two capped trigonal prisms. Figure 4.21(h), shows the

GB Plane	ϕ (degrees)	m (BB' units)	n (CC' units)
(310)	53.13	1	0
(830)	48.89	5/2	1/2
(520)	46.40	3/2	1/2
(210)	36.87	1/2	1/2
(740)	30.51	3/2	5/2
(530)	28.07	1	2
(320)	22.62	1/2	3/2
(430)	16.26	1/2	5/2
(540)	12.68	1/2	7/2
(110)	0	0	1

Table 4.3: Number of 'B' and 'C' units for [001] symmetrical tilt boundaries in the misorientation range 0°-53.13°.

GB plane	ϕ (degrees)	m (A units)	n (BB' units)
(100)	90	1	0
(910)	77.32	6	1
(710)	73.74	4	1
(510)	67.38	2	1
(920)	64.94	3	2
(410)	61.93	1	1
(720)	58.11	1	2
(310)	53.13	0	1

Table 4.4: Number of 'A' and 'B' units for [001] symmetrical tilt boundaries in the misorientation range 53.13°-90°.

structural units of the (100) and (110) boundaries, which are a tetrahedron and a plane respectively. Following the structural unit model, these singular boundaries determine two misorientation ranges, which are 0°- 53.13° and 53.13°- 90°, in a way that symmetrical tilt boundaries are composed of a combination of units of the delimiting boundaries [86]. We can call the units of the (310) boundary as 'B' units, being 'A' and 'C' units the ones from (100) and (110) boundaries respectively.

Therefore, following the structural unit model it is possible to classify the structure of the boundaries in two misorientation ranges: $90° < \phi < 53.13°$ and $53.13° < \phi < 0°$, and calculate, after geometrical considerations the number of structural units of the delimiting boundaries which compose a period of a given symmetrical tilt boundary. Given a $(hk0)$ symmetrical tilt boundary with misorientation angle ϕ and $\phi_1 < \phi < \phi_2$, where ϕ_1 and ϕ_2 are the misorientation of the favoured boundaries $(h_1 k_1 0)$ and $(h_2 k_2 0)$ respectively, the period vector of boundary $[\bar{k}h0]$ may be

decomposed as follows [118]

$$[\bar{k}h0] = m[\bar{k}_1h_10] + n[\bar{k}_2h_20] \qquad (4.3)$$

with

$$m = \frac{kh_2 - hk_2}{k_1h_2 - h_1k_2} \text{ and } n = \frac{kh_1 - hk_1}{k_1h_2 - h_1k_2} . \qquad (4.4)$$

The numbers m and n represent the number of units of each type in a given boundary. In Tables 4.3 and 4.4 the values of m and n from Equation 4.4 are presented. We have to take into account that a period in a (310) and the (110) boundary has two units each, therefore a value of n=$\frac{1}{2}$ represents just one unit in the first misorientation range.

The previous description, which predicts the number of structural units present in a given boundary depending on its misorientation angle, corresponds to highly symmetric boundaries with mirror symmetry. The minimum energy configuration structure found for most of the tilt boundaries studied have mirror symmetry, and they are well predicted as it can be seen after a comparison of Tables 4.3 and 4.4 and Figures 4.20 and 4.21. The characteristic lengths of the three structural units are also presented in Figures 4.21(a), and 4.21(h), these lengths vary slightly when forming longer period boundaries. We should notice that in the case of the (520) STGB, a highly symmetrical structure is found but an 'A' unit which had not been predicted appeared. Also we should notice that we do not obtain these highly symmetrical relaxed structures, with an atomic plane as a mirror, on the (430), (720) and (920) STGB, but distortions of them.

A similar molecular dynamics study has been done by Morita in molybdenum [81, 119]. From this work is concluded that [001] symmetric tilt boundaries in molybdenum can be described by the concept of the structure unit model. This is also supported by high-resolution transmission electron microscope images.

In searching for minimum energy configurations for each boundary some metastable structures were found. Metastable configurations have a higher configurational energy than the global minima. These metastable structures are also shown on the right hand corner of some boundaries in Figures 4.20 and 4.21. It can be seen that the metastable configurations determined by the algorithm appear as slight distortions of the minimum energy configurations.
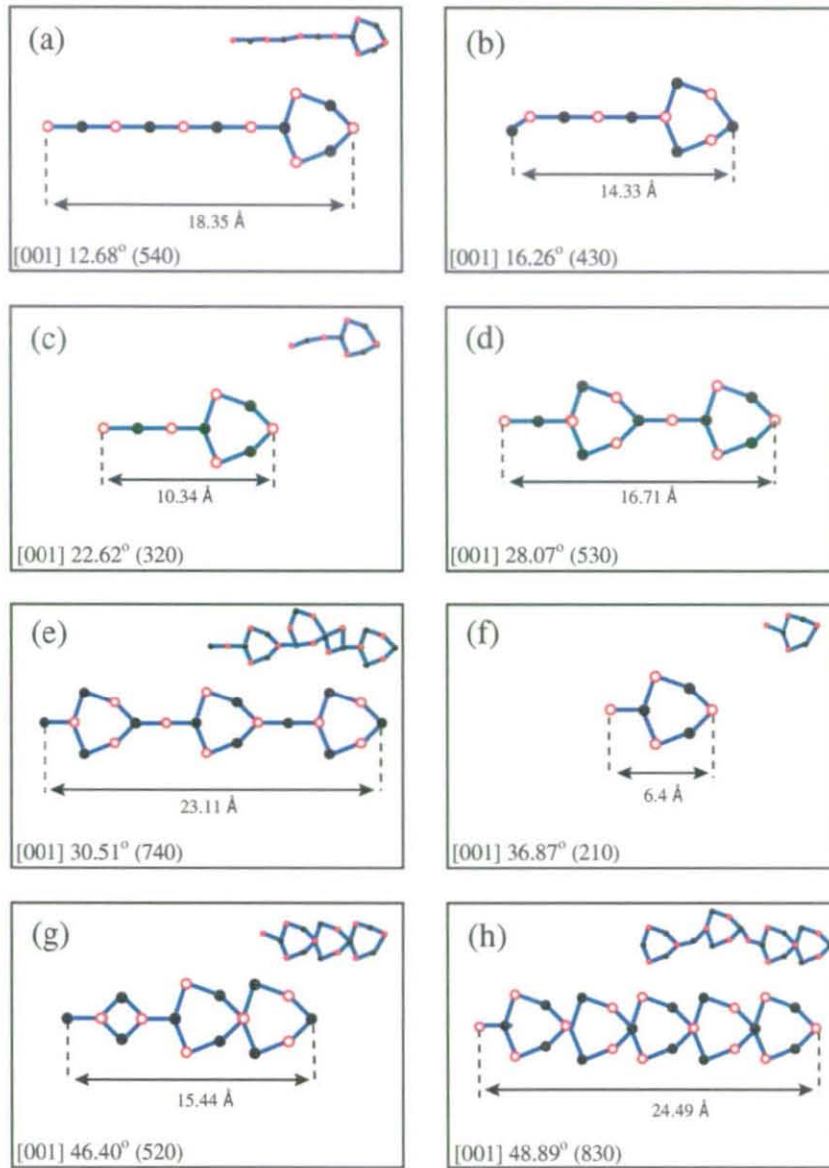
Figure 4.20: Relaxed structures with a minimum configurational energy and some metastable structures (as referred to in the main text), for the symmetrical tilt boundaries studied in the misorientation range 0- 53.13.
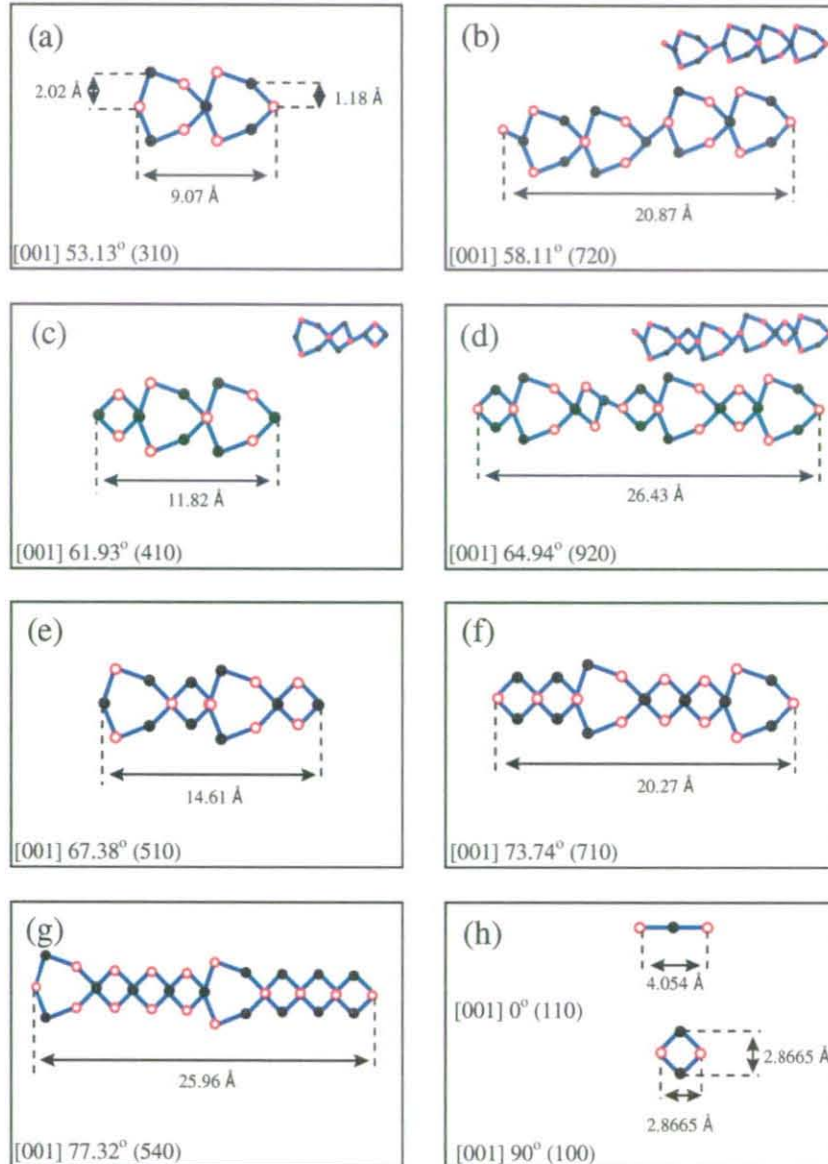
Figure 4.21: Relaxed structures with a minimum configurational energyand some metastable structures (as referred to in the main text), for the symmetrical tilt boundaries studied in the misorientation range 53.13- 90.

4.3.2 Symmetrical twist grain boundaries

The relaxed structures of [001] symmetrical twist boundaries are now presented in this section. In Table 4.5 the misorientation angle, ϕ, the coincidence site lattice parameter, Σ, the periodicity and interlayer distance, P and d, of atomic planes in directions parallel to the boundary, the dimensions and the number of atoms in each computational block is presented for the symmetrical twist boundaries studied. The coordinate system is chosen, for convenience, with x and z axes parallel and y axis perpendicular to the boundary plane respectively. The models studied have the rotation axis in the [001] direction and (001) interfacial planes, i.e. y axis. In the twist models, x and z directions have the same periodicity and the size is chosen following the same considerations as for the symmetrical tilt models. The number of atoms in each model is between 31,000 and 68,000 atoms. The models have the same coincidence site lattice parameter as the tilt models. It should be noticed that a bicrystal with a misorientation angle ϕ and a different one with an angle $90° - \phi$, will lead to the same unrelaxed symmetrical model but with a rotated pattern. Therefore the misorientation angle of the grain boundaries simulated are in the range of 0-45°. The rigid body translation vectors which give a minimum of energy configuration for each model, T_x and T_z, are also presented in Table 4.5.

ϕ (degrees)	Σ	$P_{x,z}$	$d_{x,z}$	Size (Å) (X×Y×Z)	Atoms	T_x	T_z
12.68	41	82	0.22384	91.8 × 71.0 × 91.8	51250	0.1	0.5
16.26	25	50	0.28665	71.7 × 71.0 × 71.7	31250	0.0	0.0
22.62	13	26	0.39751	72.4 × 71.0 × 72.4	31850	0.39	0.0
25.06	85	170	0.15546	105.8 × 71.0 × 105.8	68000	0.0	0.6
28.07	17	34	0.49160	83.7 × 71.0 × 83.7	42500	0.22	0.75
30.51	65	130	0.17777	92.5 × 71.0 × 92.5	52000	0.1	0.7
31.89	53	106	0.19687	83.5 × 71.0 × 83.5	42400	0.34	0.0
36.87	5	10	0.64095	77.0 × 71.0 × 77.0	36000	0.0	0.0
41.11	73	146	0.16775	98.0 × 71.0 × 98.0	58400	0.0	0.0
43.60	29	58	0.26615	77.2 × 71.0 × 77.2	36250	0.16	0.15

Table 4.5: Dimension and number of atoms of the symmetrical twist grain boundary models studies. Also, rigid body translations, T_x and T_z, which lead to the minimum energy structure are specified. The (001) is the boundary plane and the rotation axis the [001] direction for all the models.

The symmetrical twist relaxed structures with the geometrical parameters given in Table 4.5 are shown in Figures 4.22 - 4.31. In these Figures different views of the atomic structure of the interface are shown for each grain boundary: (a) and (c) are side views of the boundary, made by the projection of atomic sites in two different

planes perpendicular to the boundary plane, and; (b) is a top view with projection of the atomic sites in a plane parallel to the boundary plane. The periodic lengths of the structures are also shown in these figures. Projection in a plane parallel to the boundary, (b) top view, reveals that the typical moiré pattern of an unrelaxed twist boundary is maintained but indicates some very small changes in positions of the atoms in directions parallel to the boundary. On the other hand, changes in a perpendicular direction of atoms close to the boundary are more noticeable as can be seen in (a) and (c) side views.
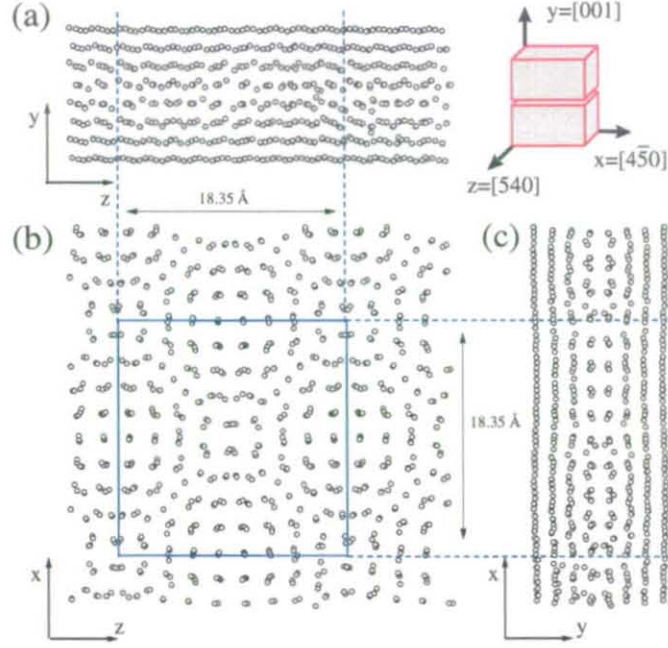

Figure 4.22: Close view of the relaxed atomic grain boundary structure of an initially unrelaxed 12.68°(001) symmetrical twist boundary with rigid body translation parallel to the boundary equal to $T_x = 0.1$ and $T_z = 0.5$.

All the models show a periodic structure along the boundary, which gets more complex as the periodicity of planes perpendicular to the boundary increases. Repeated three-dimensional periodic structures for twist boundaries in the case of fcc metals have been founded experimentally [120].

The new structures generated are periodic along the boundary, but much more complex than the symmetrical tilt boundary structures. Computational simulation studies [95] in the case of fcc metals suggest that [001] twist boundaries can be interpreted in similar terms to those used for the structural unit model in symmetrical tilt boundaries. However this procedure has not been employed in this thesis.
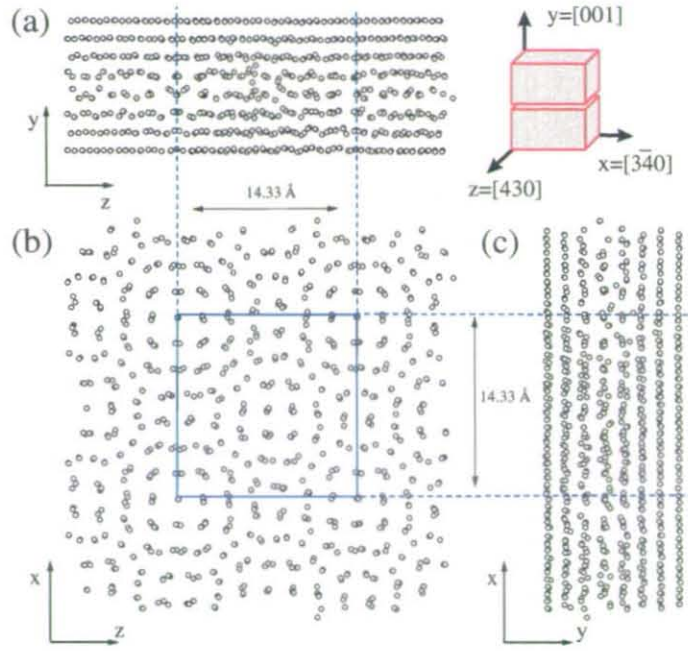
Figure 4.23: Close view of the relaxed atomic grain boundary structure of an initially unrelaxed 16.26°(001) symmetrical twist boundary.

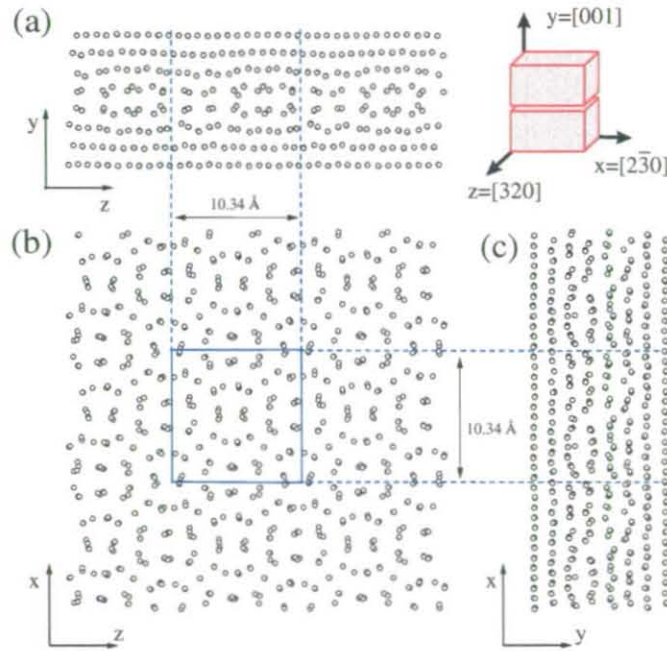Figure 4.24: Close view of the relaxed atomic grain boundary structure of an initially unrelaxed 22.62°(001) symmetrical twist boundary with rigid body translation parallel to the boundary equal to $T_x = 0.39$ and $T_z = 0.0$.

Figure 4.25: Close view of the relaxed atomic grain boundary structure of an initially unrelaxed 25.06°(001) symmetrical twist boundary with rigid body translation parallel to the boundary equal to $T_x = 0.0$ and $T_z = 0.6$.

Figure 4.26: Close view of the relaxed atomic grain boundary structure of an initially unrelaxed 28.07°(001) symmetrical twist boundary with rigid body translation parallel to the boundary equal to $T_x = 0.22$ and $T_z = 0.75$.
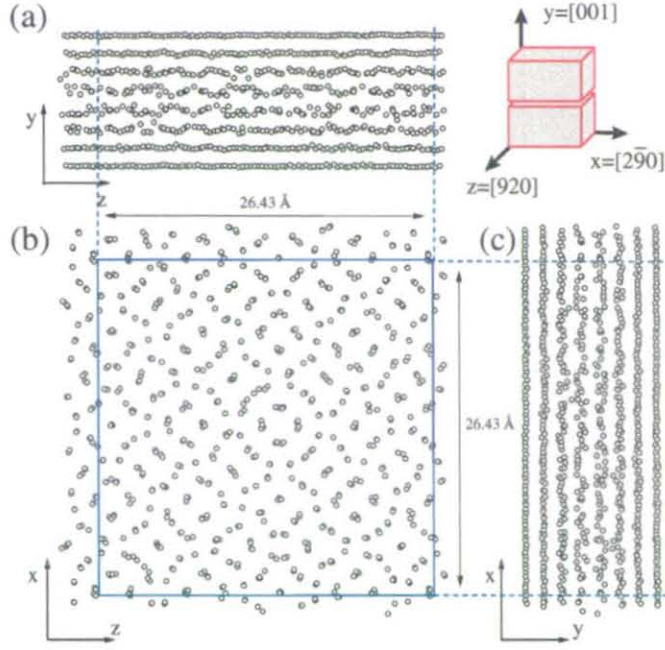
Figure 4.27: Close view of the relaxed atomic grain boundary structure of an initially unrelaxed 30.51°(001) symmetrical twist boundary with rigid body translation parallel to the boundary equal to $T_x = 0.1$ and $T_z = 0.7$.
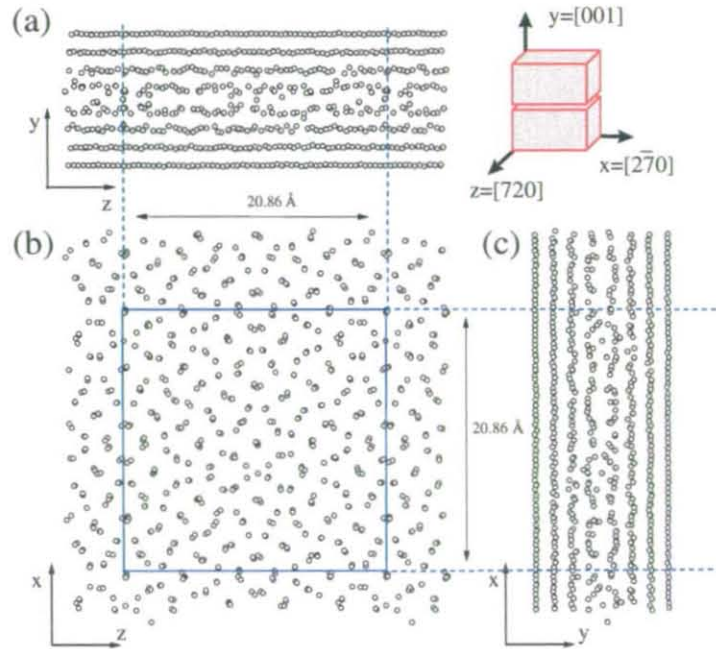
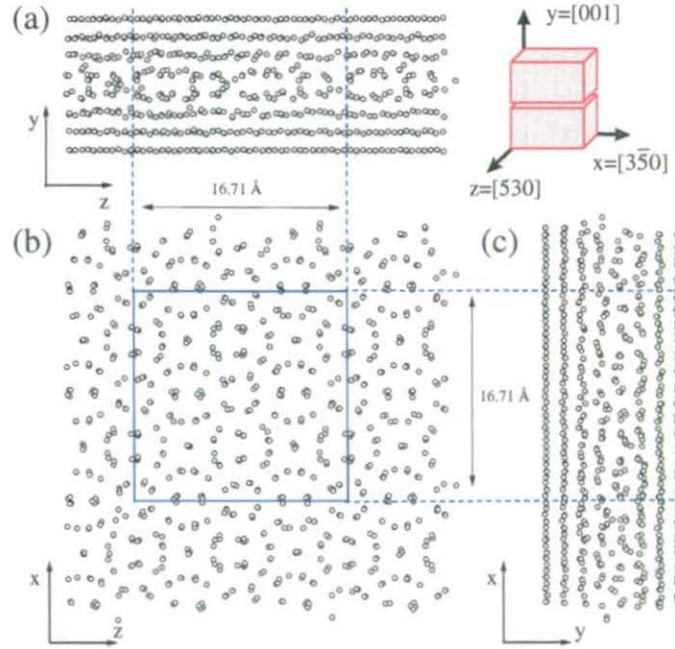Figure 4.28: Close view of the relaxed atomic grain boundary structure of an initially unrelaxed 31.89°(001) symmetrical twist boundary with rigid body translation parallel to the boundary equal to $T_x = 0.34$ and $T_z = 0.0$.

Figure 4.29: Close view of the relaxed atomic grain boundary structure of an initially unrelaxed 36.87°(001) symmetrical twist boundary.
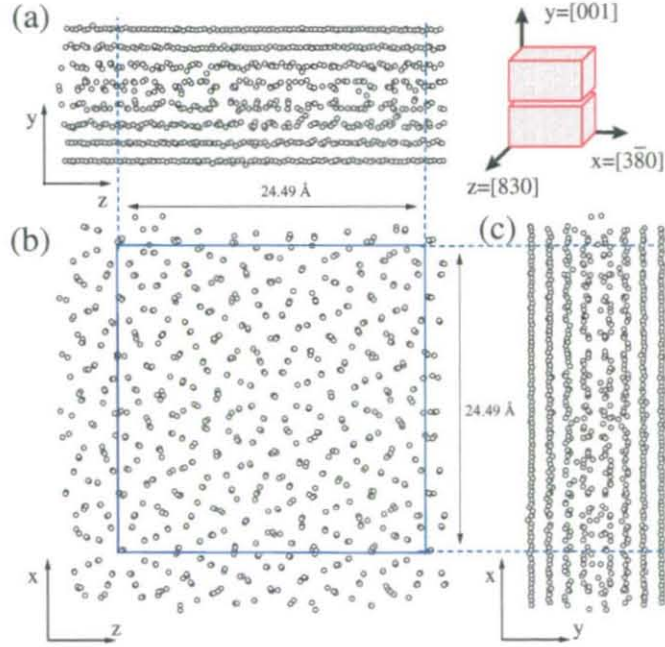
Figure 4.30: Close view of the relaxed atomic grain boundary structure of an initially unrelaxed 41.11°(001) symmetrical twist boundary.
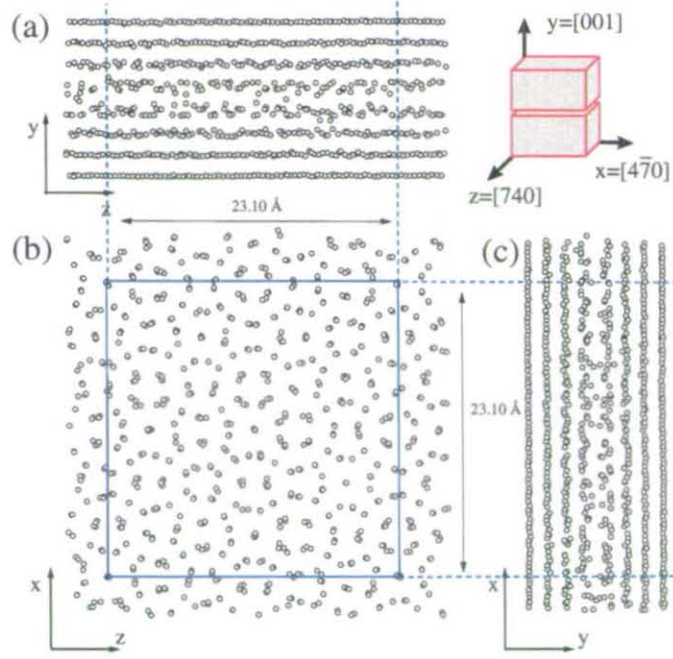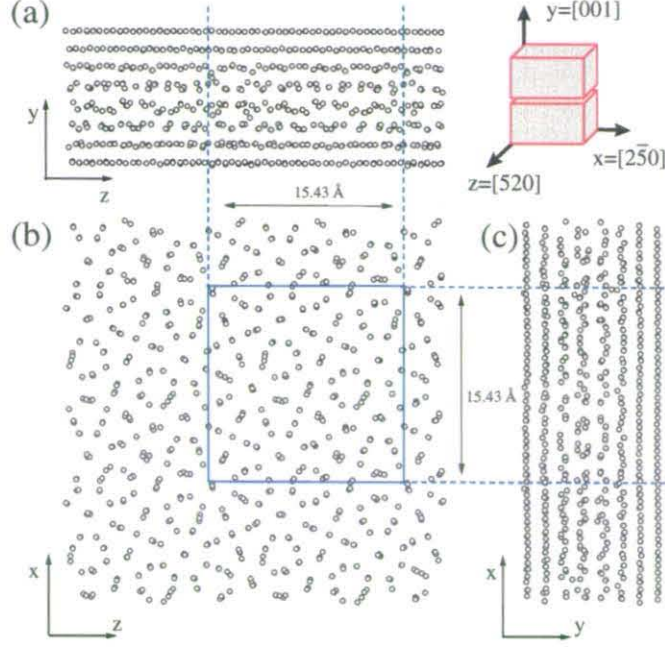
Figure 4.31: Close view of the relaxed atomic grain boundary structure of an initially unrelaxed $43.60°(001)$ symmetrical twist boundary with rigid body translation parallel to the boundary equal to $T_x = 0.16$ and $T_z = 0.5$.
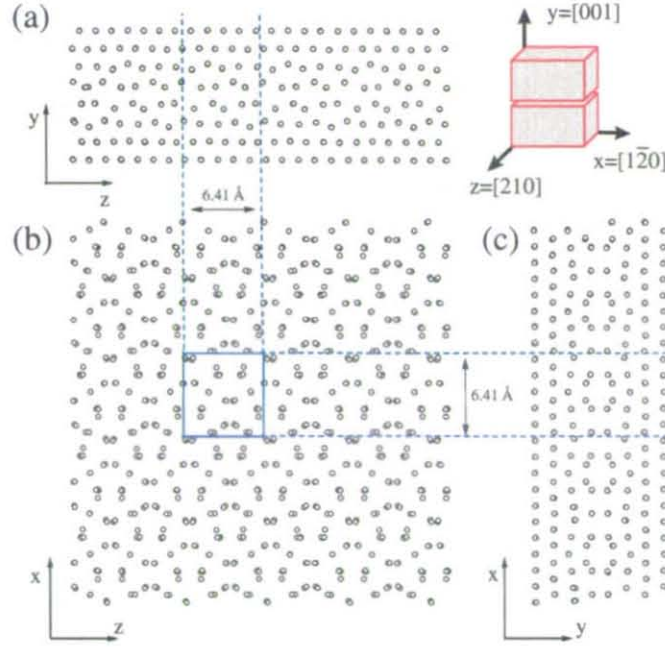
Most of the models with no rigid body translation give relaxed structures which are highly symmetric across the boundary, although these may have higher configurational energy than a model with displacement. Comparison between structures can be made with Figures 4.32 and 4.26. Figure 4.32 is the relaxed structure of a $(001)(530)[001]$ symmetrical twist boundary with no rigid body translation. These structure shows a clear repeated structure along the boundary if compared with the same model but with rigid body translation shown in Figure 4.26, however the model presented in Figure 4.32 has a higher energy than the one obtained by the relaxation of the model with rigid body translation.

4.3.3 Grain boundary energy

In order to compare stability of the structures between grain boundaries, the concept of grain boundary energy is introduced. The grain boundary energy per unit area, γ, is defined as the difference between the potential (configurational) energy of n atoms of the system including the boundary, E_p^{gb}, and the potential energy of a computational cell with the same number of atoms in a perfect crystal, E_p^0, divided by the cross-sectional area of the grain boundary plane, $Area$.

Figure 4.32: Close view of the relaxed atomic grain boundary structure of an initially unrelaxed 28.07°(001) symmetrical twist boundary.

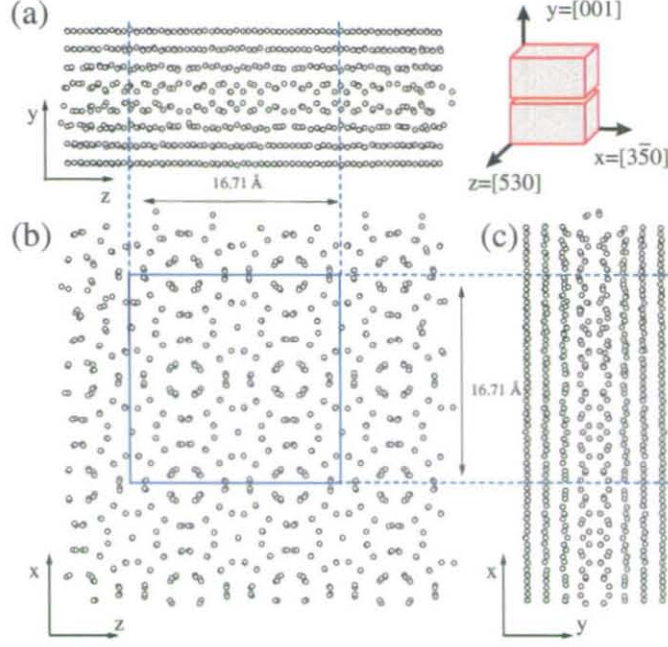$$\gamma = \frac{E_p^{gb} - E_p^0}{Area} \tag{4.5}$$

The zero energy is attributed to the perfect single crystal configuration which is the reference state, therefore $E_p^0 = -4.28n$ eV.

This definition of the grain boundary energy is to a small degree size dependent in our model due to the residual kinetic energy of the system. Size dependence effects appear on the grain boundary energy definition by choosing regions with different widths, including the boundary, where the energy of the atoms is counted. This region is a slab which is centred in the grain boundary and contain atoms with distance to the boundary less than L_y'. In Figure 4.33, the grain boundary energy as a function of the size of the slab, L_y', for a (210) symmetrical tilt boundary is illustrated. For small slab sizes not all the atomic layers affected by the boundary are included in the slab. When the slab is big enough to include the whole distorted region the grain boundary energy reaches a 'plateau', see Figure 4.33, giving an indication of the width of the grain boundary studied. For bigger slab sizes,(the enlarged scale in Figure 4.33) a linear dependence of the grain boundary energy can be observed. This drift in the energy is due to the residual kinetic energy of the system which gets bigger as we increase the size of the slab. A rough estimation give us for a system at

10 K a value of approximately 1.3×10^{-3} eV per atom of residual energy. If this value is divided by the area of the interface $\sim$ 4000 Å, and multiplied by $\sim$ 40000 atoms a value of approximately 0.01 eV/Å^2 is found as an excess of the grain boundary energy value if we consider all the atoms in the computational block. It can be seen in Figure 4.33, that the grain boundary energy will increase by approximately 0.01 eV/Å^2 if the whole computational block is considered in the definition, i.e. a slab of $\sim$ 50 Å. Different values of grain boundary energy will be obtained for different choices of the slab width, because of the drift in energy of the system. To avoid that, the grain boundary energy can be measured from the extrapolation of a line at the origin, zero width, as is shown in Figure 4.33. A equivalent way to obtain the grain boundary energy, is to calculate the energy just considering atoms inside the width of the boundary enough to include the most disturbed region. A practical definition for the width of a grain boundary is given in the next section.
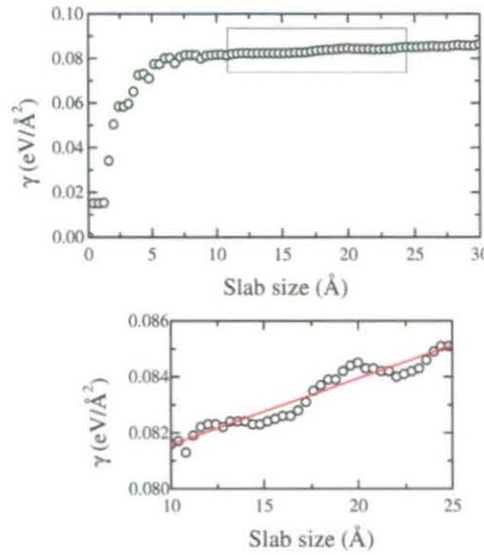
Figure 4.33: Grain boundary energy value as a function of the slab size considered. The blue region in the top figure has been magnified in the bottom figure. Values are presented for the (530) symmetrical tilt model.

The values of the grain boundary energy as a function of the misorientation angle are presented in Figures 4.34 and 4.35, for the symmetrical tilt and symmetrical twist grain boundaries studied respectively. These values are also given in Tables 4.6 and 4.7.

The grain boundary energy values for the [001] symmetrical twist boundaries are the order of 0.03 eV/Å^2 bigger than the values for the [001] symmetrical tilt
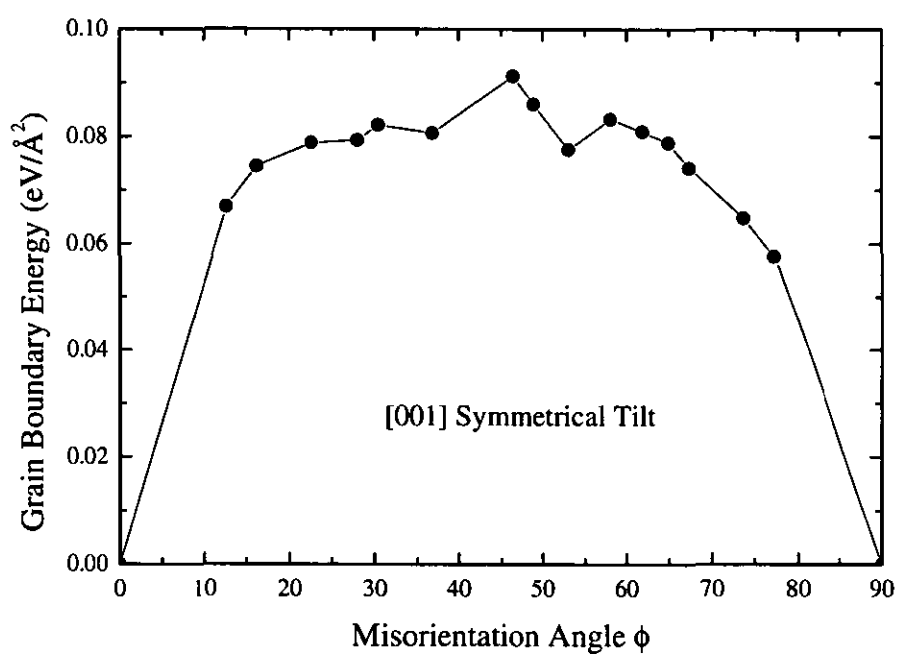
Figure 4.34: Symmetrical tilt grain boundary energies
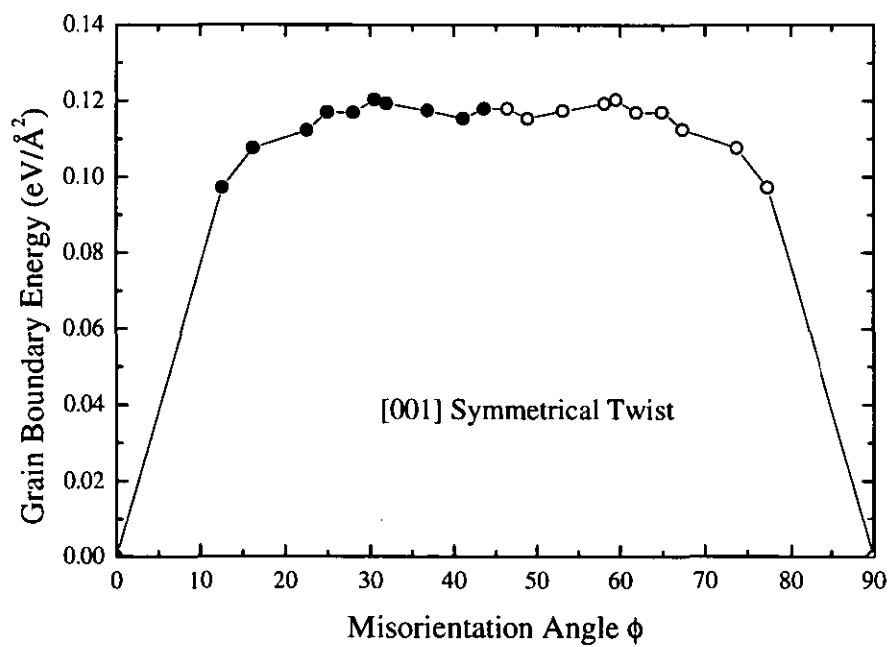
Figure 4.35: Symmetrical twist grain boundary energies. Open circles are just plotted for guidance.

boundaries in α-iron. These values are 20-30% bigger than the values for the same grain boundary energies calculated by using a Johnson's pair potential in symmetrical tilt and twist boundaries [106, 107, 121, 104]. This fact is also noticed by Watanabe et al.[112], after structural calculations of a few symmetrical tilt boundaries in bcc iron using a many-body potential of the Finnis-Sinclair form.

Many-body potentials of the Finnis-Sinclair form do not include the magnetic properties of iron therefore an approximation is made when we calculate the energy of the grain boundaries. The magnetic moment at the grain boundaries is different from the one in the bulk, as inferred from ab initio calculations [74]. Calculations on grain boundaries in iron based on a local spin density functional description for ferromagnetic materials, reveal that intergranular cohesion along symmetric tilt boundaries in iron depends strongly upon the enhanced magnetic polarization in the grain boundary region [122]. The increase in magnetic moments along the boundary considerably reduces the energy of the boundary, i.e. enhances cohesion, playing an important role stabilizing the boundary [122]. The grain boundary energy of a (310) symmetrical tilt grain boundary including the magnetic moment of iron is equal to 0.560 J/m² (0.035 eV/Å²) [122]. These values differ significantly from the value of the grain boundary energy using a many-body potential of the Finnis-Sinclair form, having a value of 1.240 J/m² (0.077 eV/Å²).

There are no experimental values of grain boundary energies to be directly comparable with the ones obtained from the atomistic simulations in this thesis, e.g. [001] symmetrical tilt and twist in α-iron. However, there exists experimental values for the grain boundary energy of δ−iron, i.e. bcc structure as α−iron, at a temperatures of $\sim$ 1200 K. This values are approximately equal to 0.770 J/m²(0.048 eV/Å²) [123, 124, 125], and can give us an idea of the order of magnitude in energy.

From our calculations special boundaries can be identified as small cusps in the grain boundary energy-misorientation plots for the symmetrical tilt models; being the (530), (210), (310) and (510) models. Three [001] symmetrical tilt boundaries have been identified experimentally as 'special' in α-iron. The symmetrical boundaries founded experimentally were the (210), (310) and (510) symmetrical tilt, after a segregation study of P, Si and C in [001] symmetrical bicrystals in α-iron. The absolute values of the enthalpy of solute segregation for these special boundaries are lower than those of typical general boundaries [126]. When the enthalpy of segregation is plotted as a function of the misorientation angle, these special boundaries show local minima, or cusps.

ϕ_{tilt} (degrees)	$\gamma(\text{eV}/\text{Å}^2)$	Width(Å)	$\Delta y(\text{Å})$
12.68	0.067	23	0.1
16.26	0.075	19	0.2
22.62	0.079	17	0.3
28.07	0.079	17	0.4
30.51	0.082	17	0.3
36.87	0.081	12	0.3
46.40	0.091	14	0.4
48.89	0.086	12	0.6
53.13	0.078	7	0.4
58.11	0.083	11	0.5
61.93	0.081	12	0.5
64.94	0.079	12	0.3
67.38	0.074	9	0.4
73.74	0.065	11	0.2
77.32	0.058	12	0.1

Table 4.6: Grain boundary energy, width and expansion of planes perpendicullar to the boundary for each symmetrical tilt model studied.

ϕ_{twist} (degrees)	$\gamma(\text{eV}/\text{Å}^2)$	Width(Å)	$\Delta y(\text{Å})$
12.68	0.097	10	0.2
16.26	0.108	10	0.2
22.62	0.112	10	0.2
25.06	0.117	10	0.3
28.07	0.117	10	0.4
30.51	0.120	10	0.4
31.89	0.119	10	0.4
36.87	0.117	10	0.2
41.11	0.115	12	0.4
43.60	0.118	10	0.4

Table 4.7: Grain boundary energy, width and expansion of planes perpendicullar to the boundary for each symmetrical twist model studied.
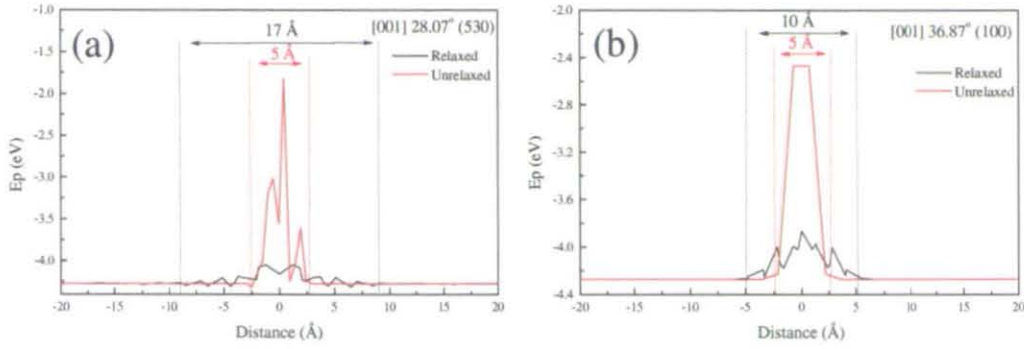
Figure 4.36: Relaxed and unrelaxed width of:(a) (530) symmetrical tilt, (b) 28.07°(001) symmetrical twist

4.3.4 Grain boundary width

As has been shown in the previous sections, the regular crystal structure is broken by a disordered region of only a few atomic layers near the boundary. The physical properties, i.e. thermal expansion, electrical resistivity, elastic response, in the vicinity of the interface can differ substantially from those of the rest of the bulk and can be highly anisotropic, because of this disordered region. These differences can change over a few atomic layers in different ways, depending on the physical property, and therefore, the definition of a width for a grain boundary is not an easy task.

A definition of the width of a grain boundary can be made, based on our atomistic model using the potential energy of the atoms close to the boundary. Atoms close to the boundary will have a potential energy which clearly differs from those atoms within the bulk. The cohesive energy of an iron atom in a bcc crystal is equal to -4.28 eV. The calculations predict a potential energy per atom equal to this cohesive energy in the undisturbed bulk. We define the width of the grain boundary as the region near the diving interface which includes atomic layers with an averaged potential energy not in the interval -4.28±0.01 eV. Similar width definitions based on the energy of atomic layers as a function of their distance to the boundary can be taken [99].

By cutting slabs of atoms parallel to the grain boundary and plotting their averaged potential energy, it is quite straightforward to 'see' the width of the grain boundary. In Figure 4.36 the averaged potential energy of atomic layers as a function to the distance to the boundary for a symmetrical tilt, (a), and twist, (b), boundary is presented. Potential energy averaged values have been obtained every 0.2 Å. The values obtained for both relaxed and the unrelaxed configurations are presented in this figures. The unrelaxed structures configurations before relaxation present high

Figure 4.37: Average potential energy of atomic layers parallel to the boundary as a function to their distance to the interface for the symmetrical tilt boundaries studied: (a) 12.68°(540), (b) 16.26°(430), (c) 22.62°(320), (d) 28.07°(530), (e) 30.51°(740), (f) 36.87°(210), (g) 46.40°(520) and (h) 48.89°(830). Boundary widths are also specified for each model.

Figure 4.38: Average potential energy of atomic layers parallel to the boundary as a function to their distance to the interface for the symmetrical tilt boundaries studied: (a) 53.13°(310), (b) 58.11°(720), (c) 61.93°(410), (d) 64.94°(920), (e) 67.38°(510), (f) 73.74°(710), and (g) 77.32°(540). Boundary widths are also specified for each model.
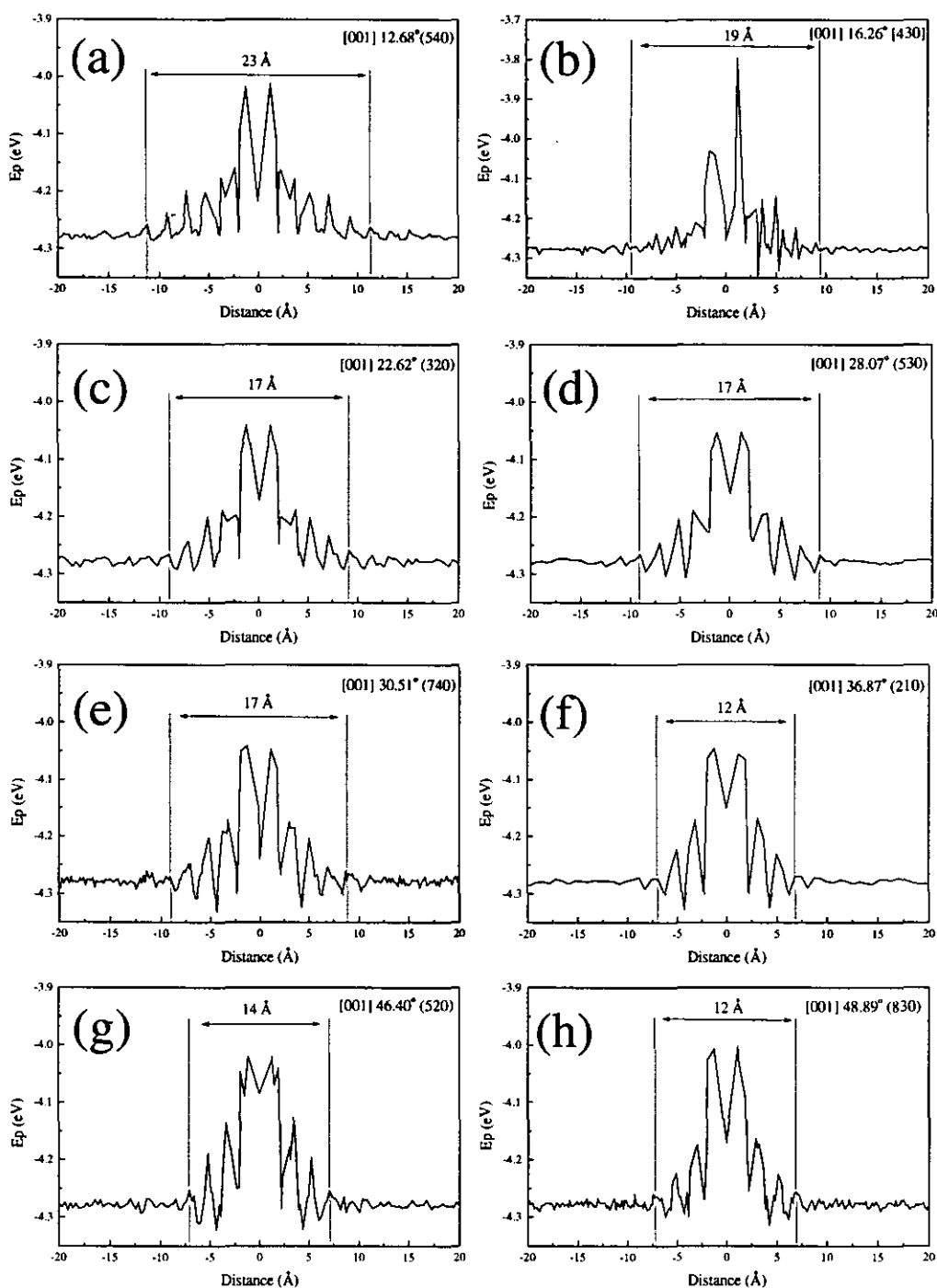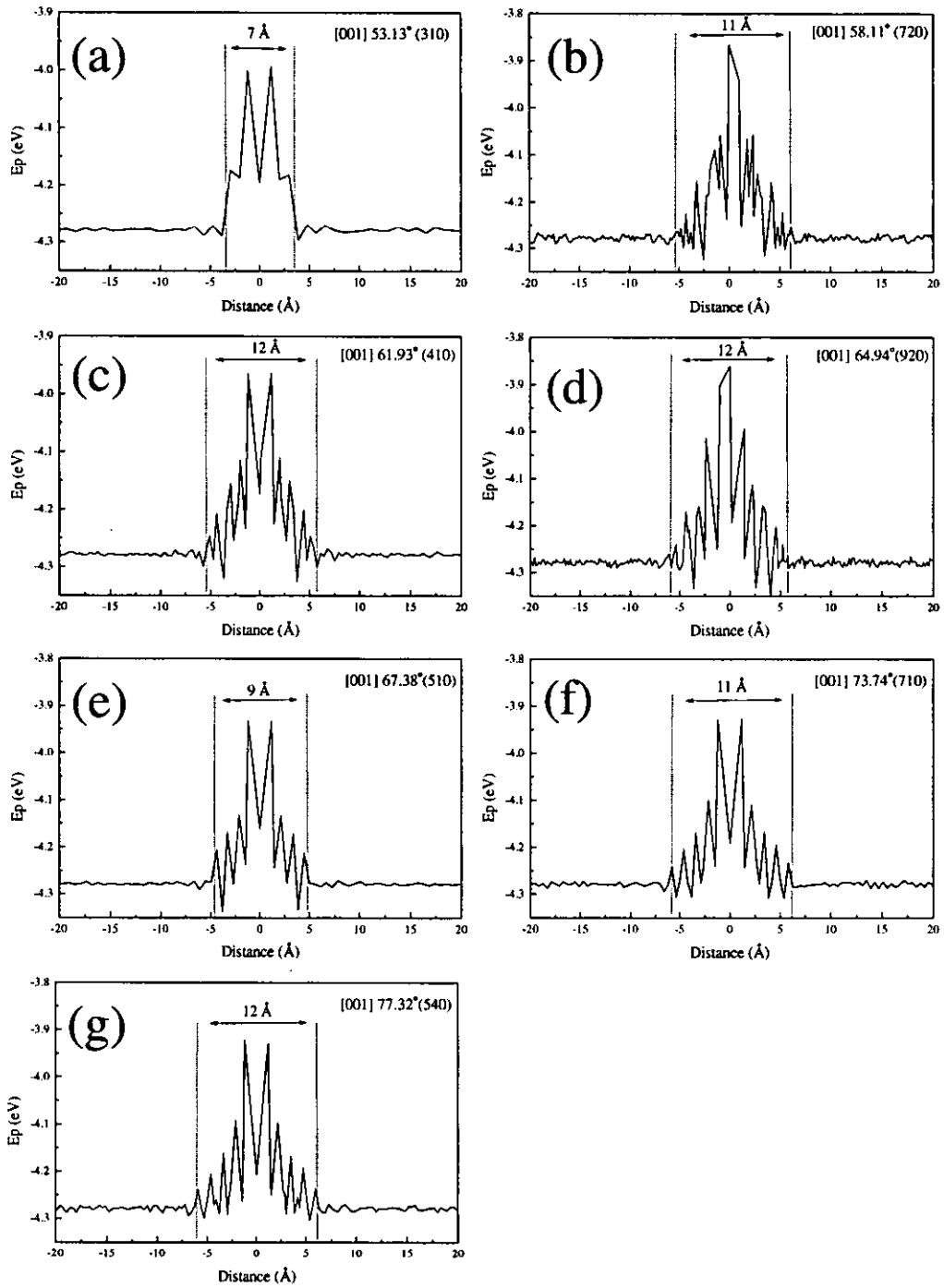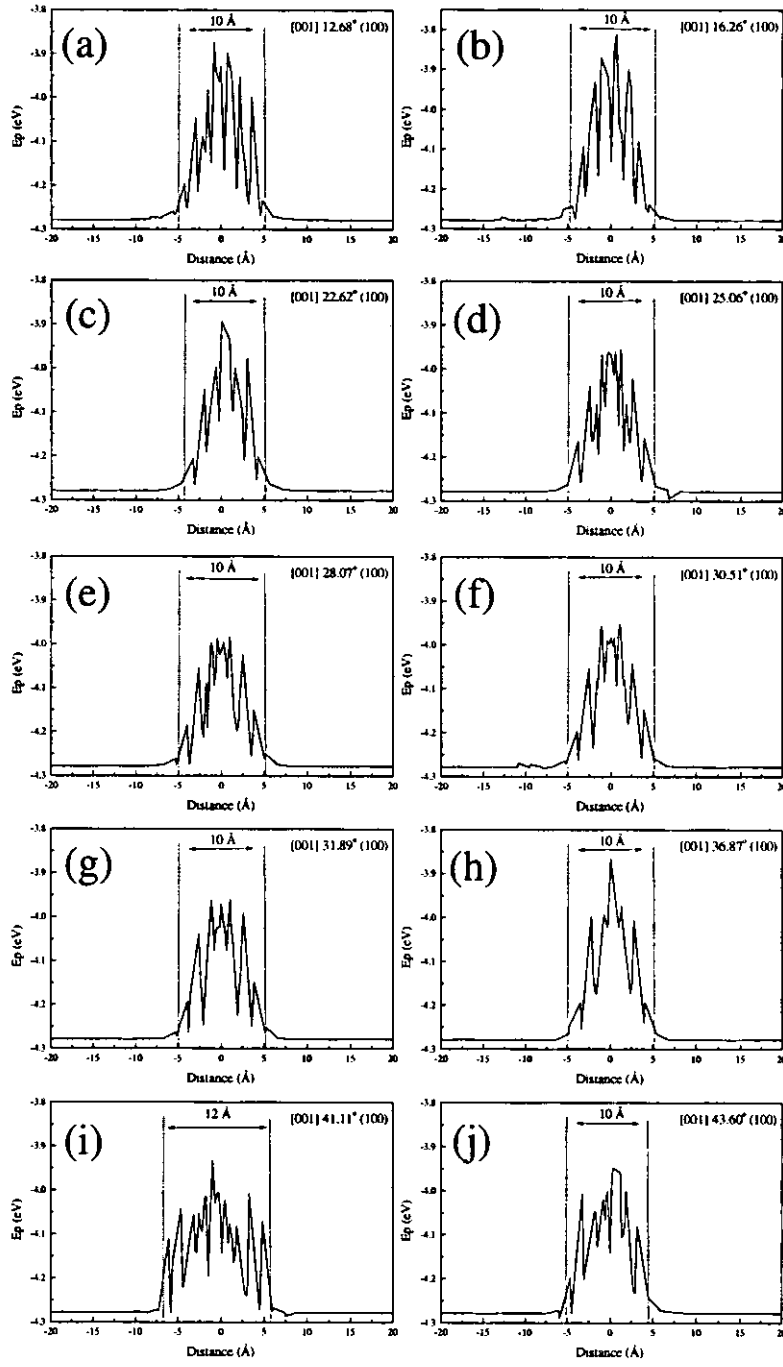
Figure 4.39: Average potential energy of atomic layers parallel to the boundary as a function to their distance to the interface for the symmetrical twist boundaries studied: (a) 12.68°, (b) 16.26°, (c) 22.62°, (d) 25.06°, (e) 28.07°, (f) 30.51°, (g) 31.89°, (h) 36.87°, (i) 41.11° and (j) 43.60°. Boundary widths are also specified for each model.

energy values in a few layers near the interface. After relaxation a new configuration near the interface appear reducing the potential energy values.

Following our width definition, the unrelaxed configurations presented as a example for the twist model in Figure 4.36(b) has a width equal to 5 Å and it includes 4 unrelaxed atomic layers. After relaxation the width of the boundary is equal to 10 Å and it includes 8 atomic layers. The grain boundary width and the potential average plots for the symmetrical tilt studied are presented in Figures 4.37 and 4.38; the same study for the symmetrical twist models is shown in Figure 4.39. These values are also given in Tables 4.6 and 4.7. Symmetry across the interface of the relaxed structures can be inferred from these plots.

The width of the grain boundary is different for different grain boundaries. The width of the tilt boundaries studied are in the range of 7-23 Å. For the twist boundary the widths are all approximately equal to 10 Å. The interlayer distance parallel to the interface is always the same for all the twist models and equal to $a_0/2$; for the tilt models the interlayer distance varies approximately between $a_0/20$ and $a_0/3$, and therefore the planes are much closer to the discontinuity in the crystal and more layers will be involved in the relaxation process for the tilt boundaries. Figure 4.40 presents the grain boundary widths of the symmetrical tilt models as a function of (a) the interlayer distance and (b) the misorientation angle. These graphs suggest a decreasing linear dependence of the grain boundary width for the [001] symmetrical tilt models with both interlayer distance of planes parallel to the boundary and misorientation angle.
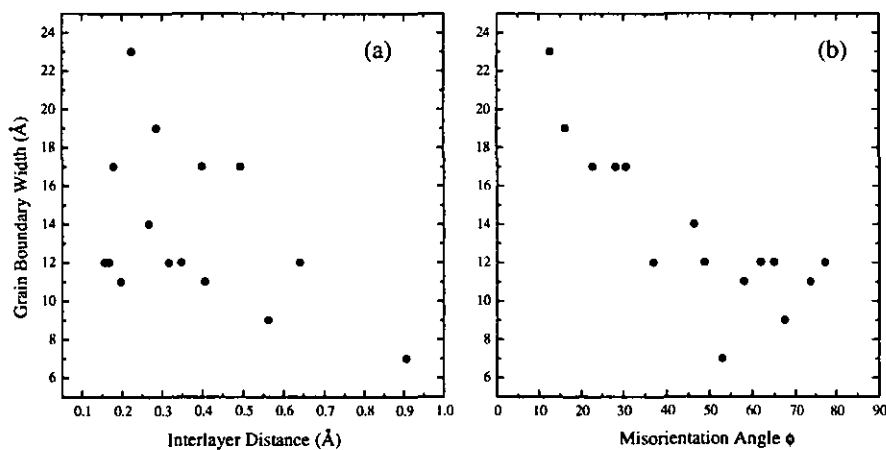

Figure 4.40: Grain boundary width as a function of:(a) the interlayer distance and, (b) the misorientation angle of [001] symmetrical tilt bondaries in α-iron.

4.3.5 Volume expansion

An important characteristic of grain boundaries is the outwards expansion suffered by atomic layers parallel to the boundary. Atomic layers expand in order to accommodate the new atomic configuration at the boundary. This expansion introduces a 'free volume', compared with a perfect crystal, which can control process such as segregation of impurities towards grain boundaries. Local volume expansion in direction perpendicular to the boundary have been experimentally founded by HREM studies[127, 128].

In Figure 4.41 the averaged displacement of each atomic layer according to their distance to the boundary is presented for a (530) symmetrical tilt boundary. It can be inferred from Figure 4.41, that the layers in both sides of the interface are displaced away from it. This displacement is symmetrical at both sides of the boundary.
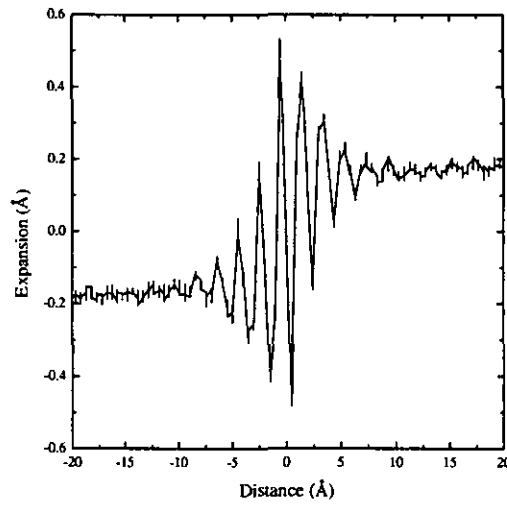
Figure 4.41: Average perpendicullar displacement of atomic layers as a function of their initial distance to the boundary before relaxation. Values for the (530) symmetrical tilt boundary model are presented.

Oscillations in the interplanar spacing close to the boundary can be inferred from Figure 4.41. These oscillations decay exponentially away from the boundary as it can be described by simple analytical models for the study of relationship between structure and energies in grain boundaries [36]. The total expansion is given by the displacement of atomic layers far away from the boundary. Therefore in the example shown in Figure 4.41, the expansion is approximately 0.4 Å . Expansion values for the symmetrical tilt and twist boundaries studied are given in Tables 4.6 and 4.7.

In Figure 4.42 the volume expansion as a function of the grain boundary energy for the symmetrical tilt models is presented. These results suggest that volume expansion increases linearly with the grain boundary energy. Previous computer simulations have also suggested a certain degree of correlation between the grain boundary energy and the volume expansion [121].
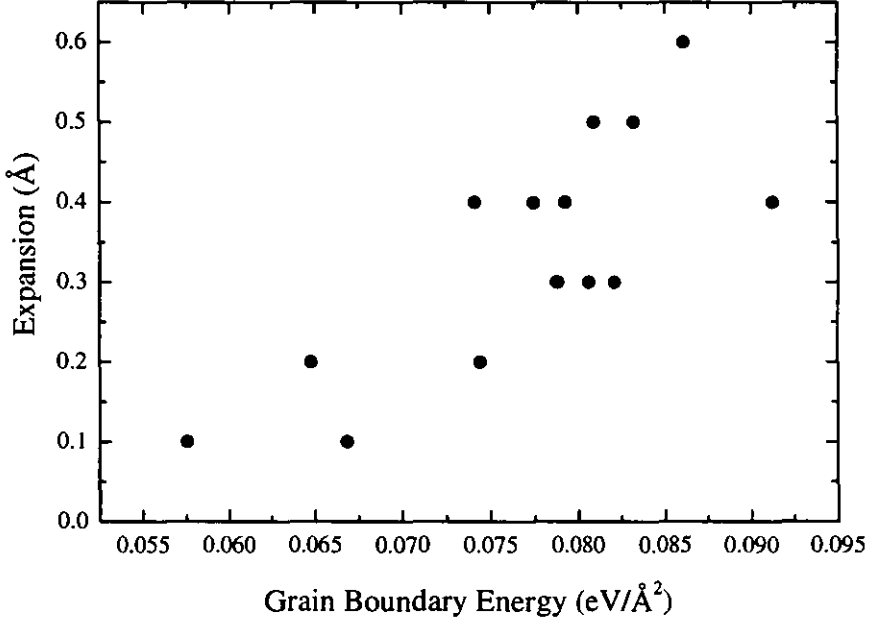
Figure 4.42: Expansion of atomic layers perpendicullar to the boundary as a function of the grain boundary energy for [001] symmetrical tilt boundaries in α-iron.

4.3.6 Adding atoms

The twist boundary has a higher relaxed energy than the tilt boundary and the density of atoms is smaller there. There is possibly a reasons why the twist boundary has this higher energy. The reason could be that there are insufficient atoms at the interface to form the 'best' minimum energy structure. This aspect could be studied further by adding atoms to the interface region and relaxing until a lower energy is reached. This possibility has been studied by a simple test in this thesis.

The atomic structure of symmetrical twist grain boundaries present periodic atomic arrangements with enough free volume to accept particles. That can be observed, for example, in Figures 4.32 and 4.29, where configurations with gaps appeared. Using the relaxed model with no translations for the 28.07°[001] symmetrical

twist boundary, Figure 4.32, particles were added to the interface region. This new configuration was further relaxed.

The grain boundary energy of the relaxed structure without additional atoms, which is shown in Figure 4.32, is equal to 0.123 eV/Å². New configurations with 12, 24 and 100 additional particles were added in a plane parallel to the centre of the boundary and placed at the various periodic gaps. The final grain boundary energy configuration for the three previous structures were equal to 0.121, 0.120 and 0.110 eV/Å² respectively. These grain boundary energy are smaller than the model without additional atoms and without rigid body translation. In addition, the model with 100 extra-atoms, gives a grain boundary energy value which is smaller than the minimum configuration of the 28.07° (001) obtained by a translation of the original CSL description.
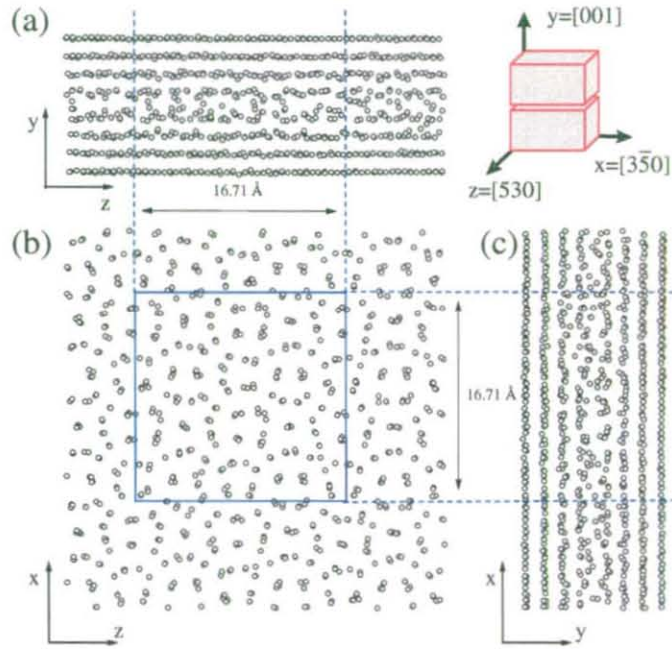
Figure 4.43: Close view of the relaxed atomic grain boundary structure for the 28.07° (001) symmetrical twist with 100 additional atoms.

In Figure 4.43 top and side views of the grain boundary structure for the model with 100 additional atoms is presented. The atomic arrangement which has been shown to be more stable for the previous models of the same twist boundaries is different to those presented in Figures 4.32 and 4.26. Differences are perhaps more clearly seen from the averaged potential energy plot of atomic layers presented in Figure 4.44. The width of the grain boundary has increased by 1 Å after the addition of the additional particles.
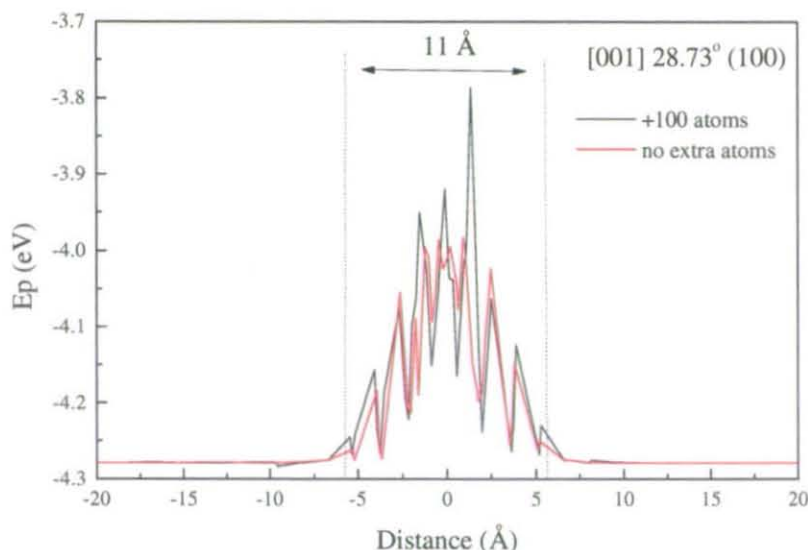
Figure 4.44: Comparison of the average potential energy of atomic layers parallel to the boundary as a function to their distance to the interface for the model with no translation for the

4.4 Conclusions

In this chapter the atomic structure of symmetrical grain boundaries in $\alpha-$iron has been obtained by computer simulation. A total of 15 symmetrical tilt and 10 symmetrical twist boundaries, all of them with the rotation axis along the [001] direction of the bcc structure, have been studied. The misorientation angle between grains ranges from 12.7°-77.3° and 12.7°-43.6° for the tilt and twist boundaries respectively, providing a good sampling of 'high-angle' grain boundaries.

A computational methodology for obtaining the equilibrium relaxed atomic configuration at the boundary has been presented. Computational blocks of atoms containing the desired interface are implemented following a coincident site lattice (CSL) geometrical description of a bicrystal and including also rigid body translations of one grain respect to the other. These computational blocks were relaxed to their minimum energy configuration following a standard molecular dynamics procedure using a many-body potential of the Finnis-Sinclair form for α-iron. The size of the computational blocks depend on the interface to be modelled, the smaller and the larger systems containing 28260 and 68000 atoms respectively, which are limited by computational resources available.

The minimum energy configurations found for the symmetrical tilt boundaries present a clear periodic atomic structure along the boundary, this structure being

different for different boundaries. The atomic structure obtained can be thought as a sequence of basic structural units. Most of the tilt boundary configurations found are well described as a combination of basically three structural units. These structural units are the ones which form the (100), (110) and (310) symmetrical tilt boundaries. Most of the symmetrical relaxed twist boundaries show present a periodic structure, however they do not contain such clear configurations based on a structural unit model.

The final grain boundary structures have been classified in terms of energy, width and expansion of the distorted region. The grain boundary energy is defined as the difference of the configurational energy of the system with respect to one with the same number of atoms in a perfect crystal, per unit area. The grain boundary energy values follow the same pattern as previous simulations in α-iron with pair-potentials when they are presented as a function of the misorientation angle, showing cusps of energy for some 'special' boundaries. In this work these boundaries are the (530), (210), (310) and (510) symmetrical tilt models. Values for the grain boundary energies are smaller in the tilt boundaries i.e. 0.058-0.091 eV/Å^2, compared with those in the twist boundaries i.e. 0.097-0.120 eV/Å^2.

A definition of grain boundary width has been proposed. This definition is based on the averaged potential energy of atomic layers parallel to the boundary. We define the width of the grain boundary as the region near the diving interface which includes atomic layers with an averaged potential energy not in the interval -4.28±0.01 eV. The width, definied in this way, is different for different boundaries, showing a dependence on the interlayer distance of planes parallel to the boundary and the expansion of these planes away from the boundary. The width of the tilt boundaries studied are in the range 7-23 Å, being for all the twist models approximately the same and equal to 10 Å. The width of a grain boundary shows a dependence on the interlayer distance of planes parallel to the boundary and also with the expansion of these planes away from the boundary after relaxation. The expansion values have been shown to vary, depending on the grain boundary, in a range 0.1-0.6 Å.

A brief study was made for the 28.07° symmetrical twist boundary in which particles were added in a middle plane of the boundary in positions where gaps appeared. Final configurations with smaller grain boundary energy values were obtained. This suggested that more stable twist boundaries can be obtained by adding additional particles to the CSL initial structure.

This chapter has provided a formalism for the study of the atomic structure of symmetrical boundaries. Next chapter utilises this for the study of the interaction of collision cascades with such boundaries.

Chapter 5

Radiation damage at grain boundaries

5.1   Introduction

The interaction of radiation with matter is one of the most exciting parts of physics in addition to being a basic pillar of the development of new technologies. Nowadays, the understanding of the effects of radiation interactions with matter has made possible the use of particle beams for developing, for example, new semiconductor devices and new tools for diagnostics in medicine. In particular, the interaction of radiation with solids is an area which has applications, not only for the semiconductor industry but also for space and nuclear energy programmes.

Fission and fusion reactor technology are, perhaps, one of the most important fields where studies of radiation effects play a key role [129]. In 1943, E. P. Wigner predicted the existence of displaced atoms in those parts of nuclear reactors which are irradiated by an intense neutron flux [130]. Fast neutrons from nuclear reactors produced as a result of a fission reaction can carry energies up to several MeV; such quantities of energy are more than sufficient to produce structural damage in any material. These neutrons, or any other particles with enough energy, will produce damage in a target when losing all or part of their energy. Radiation starts a cascade process with production of point defects which have a profound impact on the microstructure of the material [131]. The tremendous technological importance, in addition to the safety implications of radiation damage on the structural materials of nuclear reactors, has resulted in a vast amount of work on the subject since the early 1940's. In particular, because all nuclear reactors have steel components, there has been much research activity concerning the ageing of steel components under irradiation.

The radiation effects on materials used in the nuclear industry include: the embrittlement of the material, swelling and the erosion of wall surfaces. The structural

materials, e.g. steels, forming the pressure vessels that contain the fission reactor cores, are damaged by the fast neutron radiation coming from the fission chain. The most important effect of this radiation is the increasing of the ductile-brittle transition temperature, i.e. the temperature below which failure would be by brittle fracture. Above this temperature, typically ≥ 300 K above, the energy required to cause a crack to grow has a stable value called the 'upper shelf' value. Above this temperature, steels maintain their optimum strength. A pressure vessel can become brittle at room temperature or even at the operating temperatures of the reactor because of the increasing of the ductile-brittle transition temperature[129], this will provoke the failure of the vessel.

Swelling has serious effects on the efficiency nuclear reactors. At high neutron fluxes a large amount of interstitials and vacancies are formed. At the working temperature of the reactors, most of these point defects recombine, however some clusters of interstitials can be formed and subsequently collapse to form dislocation loops and vacancies nucleate forming voids, as a result of void formation the metal swells, increasing its volume, for a review see [132].

Energetic particles produced in fusion reactions have an important role on the development and design of nuclear fusion reactors. The main effect of this radiation is to damage the first wall and as a consequence of erosion cause the release of atoms from the wall into the plasma, contaminating the fusion process.

5.1.1 The collision cascade theory

The basic defects which can be produced at the atomic level in metals have been well known since early studies of the radiation theory. When a crystal is bombarded with energetic radiation, defects and imperfections appear in the initially perfect crystalline structure.

Vacancies and interstitials are the basic structural defects produced in a crystal as a result of radiation. When an atom receives enough energy to move from its lattice site to another place which is not a site within the perfect crystallographic structure, it is said that this atom has become an interstitial, and the site which this atom has left behind is called a vacancy. The combination of vacancy plus interstitial is known as a Frenkel pair. Imperfections which remain after the energetic radiation has ceased are called radiation damage and any physical property change which may result is called a radiation effect [133].

The energy lost by a projectile during its track through a solid is mainly transferred to the atoms within the material as elastic energy loss, and to the electrons of

the material as inelastic energy loss. In metals, the displacement of atoms by direct collisions, i.e. elastic energy loss, is the most important cause of damage. The cross-sections for the transfer of momentum to a single atom from bombarding particles, ions or neutrons, have been sufficiently well known for a number of years. However, a major concern for the study of radiation damage in metals is to understand the processes and the damage caused after this single 'recoil' atom has been struck by a projectile and has been endowed with an excess of kinetic energy. An atom of the lattice which is struck by radiation receiving enough energy to move is called primary knock-on atom, PKA. The PKA can undergo collisions with its neighbours to an extent which will depend on the amount of energy received. A cascade of displaced atoms will therefore build up. If this collision cascade intersects with a free surface sputtered atoms away from the surface are produced.

The basic ideas which were developed during the first years of the study of radiation damage, in the 1950's, remain today. Seitz built the first blocks of a theory which tried to describe the imperfections produced in solids by radiation [134, 135]. This theory said the effects of radiation on metals were based on Frenkel defects and effects resulting from thermal spikes. This theory was refined by several authors in subsequent years, including Brinkman who gave the most important contribution when he introduced the concept of a displacement spike [136, 137].

Fundamental to the first radiation theory was the notion of threshold energy, which is the energy required to move an atom from its site lattice and form a Frenkel pair. After some simple and very general considerations this energy was fixed by Seitz at a value of 25 eV for any metal [134]. Therefore, there was a step function which related the displacement probability of an atom with the transferred energy. Very soon, it was realised that this threshold energy was directionally-dependent.

Another key term in radiation theory is the number of displaced atoms, $N(E)$, resulting from a primary energy E. Kinchin and Pease [138] presented the first estimation for this value after a statistical treatment based on several assumptions [139]:

- it was assumed, as has been said, that the displacement threshold was fixed, E_d;

- collisions were purely elastic;

- only two-body interactions were assumed;

- energy losses less than the threshold energy were not considered;

- annealing of damage, i.e. interstitial and vacancy recombination was assumed to be negligible;

- it was considered that in each collision the energy was equally shared between the two atoms.

Taking into account all of these assumptions, the number of displaced atoms can be expressed as [138]:

$$N(E) = E/(2E_d), \quad E > 2E_d \tag{5.1}$$
$$N(E) = 1, \quad E_d < E < 2E_d$$
$$N(E) = 0, \quad E < E_d$$

Following these requirements and based on the work of Seitz and Koehler [140], Yoshida used the Monte-Carlo method to calculate the number of Frenkel pairs in germanium, which was one of the first computer simulations in this area [141]. Yoshida's work predicted a value for the number of Frenkel pairs in good agreement with the one predicted by Equation 5.1. Also in Yoshida's work explicit graphical results of the path of the primary knock-on atom and the branching 'tree-like' structure created by vacancies and interstitials were shown.

However, there was experimental evidence that the number of defects predicted by cascade theory overestimated the number of defects at least in a factor of 10. The most obvious simplification of this theory was to consider collisions as isolated events. This fact was the first evidence that the displacement cascade was a complicated, many-body process.

The Kinchin-Pease formula was later refined following a binary collision model by Norgett, Robinson and Torrens (NRT) [142]. The number of Frenkel pairs given by the NRT formula, $N_{NRT}(E)$, follows:

$$N_{NRT}(E) = 0.8E_{dam}/(2E_d) \tag{5.2}$$

where E_d is the threshold energy averaged over all crystallographic directions and E_{dam} is the energy available for elastic collisions. If the inelastic interactions are considered negligible E_{dam} can be considered to be equal to the initial kinetic energy of the PKA.

Another question arose related to the fate of the energy which is delivered to the lattice and is not followed by displacement, for example in glancing collisions. This provokes collective excitations in form of vibrations of atoms which can be

transferred to neighbours and finally damped out to the surrounding crystal. The energy transferred in this way was regarded as a sudden delivery of heat to a restricted volume of the lattice and that the primary collision event was the origin of a spherical thermal spike [140]. Thermal diffusion equations in a homogeneous medium were applied to this idea. As a result, few Frenkel pairs were expected to be formed by this method compared to the number produced by direct collision events.

A new view of the radiation damage process was given by Brinkman [136] when he introduced the concept of a displacement spike. Brinkman studied the relationship between the mean free path for displacement collisions and the energy of the primary knock-on atom, concluding that the mean free path for displacement collisions of a primary knock-on atom with enough energy, can fall below an interatomic distance. In this situation, the primary knock-on atom will create a large number of vacancies in a short time, forcing atoms away from its track. These atoms can also displace other atoms in a chain sequence. The final picture, after the primary knock-on atom has lost all of its energy heating the lattice, was seen to consist of a shell of interstitial atoms which are separated from a core of vacancies, the so-called displacement spike. It was expected that few Frenkel pairs remained and most of interstitials and vacancies created annealed, i.e. recombined.

A new contribution to the theory was made by Silcox and Hirsch [143] to explain the presence of dislocation loops on fast neutron irradiated metals. Basically, the region damaged for the displacement spike was visualized as containing vacancies at the centre which were able to nucleate dislocation loops and an outer shell of vacancies and interstitials which recombined. The main contribution to the previous displacement spike theory of Brinkman was that the excess of interstitials diffused until they reached other dislocations, grain boundaries or free surfaces, i.e. sinks for defects.

Later, Seeger included focusing and channelling as mechanisms to explain the probable existence of long range transport of matter, i.e. interstitials away from the vacancy core, in addition to energy losses by displacements and glancing collisions [144]. Focusing was first suggested by Silsbee and, is produced when an atom cannot penetrate the surrounding lattice and transfers the energy and momentum to one of its neighbours, which will subsequently do the same with its neighbour [145]. In particular, if there is a close packed row of atoms in the crystal, a sequence of collisions and a transfer of energy is expected, the so-called focuson, i.e. focused collision sequence. Not only transfer of energy can occur, but also a replacement collision sequence occurs, this being the atoms propagated as dynamic crowdion, leaving a vacancy at one end of the line. A crowdion is formed when an interstitial is

packed into a close packed line of atoms which already had enough atoms to occupy the available lattice sites. Replacement collision sequences appear when an atom comes to rest, after collision, occupying the lattice site of the other atom. On the other hand, there exist open directions within a crystal structure, bordered by close packed directions, where an atom can enter and move down this channel long distances because the interaction with the lattice is small and, in an ideal case, is not going to suffer any collision, the so-called 'chanellon'.

The final picture of ideas collected until the early 1960's can be summarized in the schematic two-dimensional representation of a primary knock-on atom impinging on a part of a face centred cubic lattice presented by Seeger [144], Figure 5.1, quite similar to the one given by Brinkman. A primary knock-on atom, in its wake, leaves isolated vacancies and Frenkel pairs behind, before coming to rest. Energy and momentum are propagated down close-packed crystallographic directions leaving an interstitial at the end. The final result is a concentrated zone of vacancies, a depletion zone, with interstitials formed away from it, often in form of stable dumbells, i.e. two interstitials sharing a vacancy site. Immediately afterwards, most of these defects rearrange and recombine in a phase which will lead the material to thermal equilibrium, which requires longer times compared with the ballistic phase of the collision cascade.
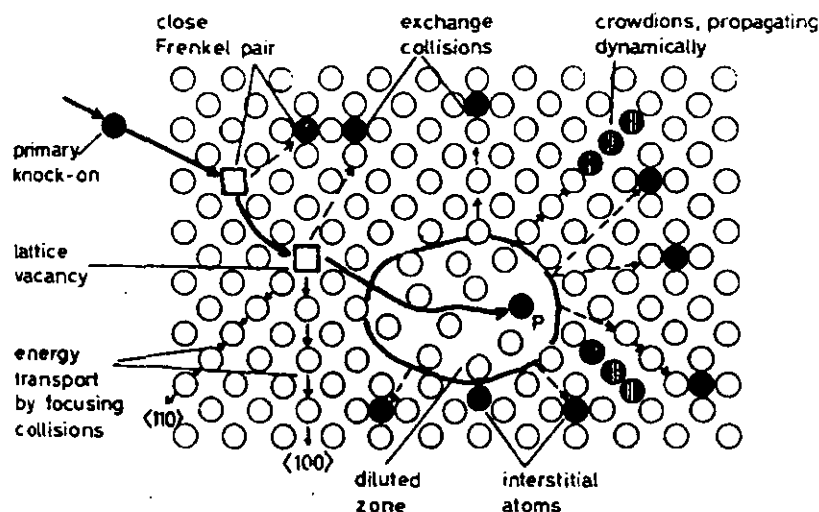

Figure 5.1: Schematic two-dimensioanal picture of the radiation damage by fast neutrons in a face centrd cubic metal, after [144].

125

5.1.2 Early atomistic simulations

Due to the many-body nature of collision cascades it was difficult to develop a single cascade theory covering the collisional events produced in time scales approximately less than 0.1 ps, and the longer thermal rearrangement produced after the collisional phase. The improvement in understanding of the processes that occurred in collision cascades came from the development of atomistic computer simulations.

In 1960, Gibson, Goland, Milgram and Vineyard published the results of the first molecular dynamics computer atomic simulation on radiation damage [146]. Vineyard and co-workers faced the study of radiation damage with a new and revolutionary approach using computer resources available to them ('high-speed' digital computer as they called it) to simulate the evolution and effects of a primary knock-on atom in a crystal lattice. Basically, they implemented the classical equations of motion for a set of atoms in a computer in order to solve for the dynamics of the system. The crystal they simulated was copper, a fcc lattice with 500 atoms at rest, 1000 atoms in some cases, and with a primary knock-on atom which was endowed with energies between 25 and 400 eV and different velocity directions. The total time simulated was approximately 2 ps depending on the particular case. The Born-Mayer pair repulsive potential was used for these calculations. The main results of these simulations were:

- damage at low energies consisted of vacancies and interstitials;

- interstitials reside in dumbell configurations;

- focusing was observed, collision sequences occurred in both <110> and <100> directions;

- sequences evolving as a dynamic crowdion producing an interstitial near its end were also observed;

- the threshold energy was lowest near to the <100> directions;

- agitations following damage resembled thermal spikes but the transport of energy is far from isotropic as predicted by thermal spikes models;

- the vibrational mode associated with interstitials retained their energy longer than other modes [146].

126

These computer simulations confirmed the basic ideas of the cascade theory, however the calculations did not lead to the depleted zone described by Seeger [144]. The possibility of the creation of an amorphous zone was postulated for larger sets of atoms and higher energies of the collision cascade [147].

These molecular dynamics simulations were extended to body centred cubic metals in particular to α-iron [148] and in general supported the main results of the simulations in copper. It was found that the key mechanism of displacement at low energies was a dynamic replacement where the knock-on atom replaces one of its neighbours. This replacement by the knock-on atom causes an extended sequence of correlated replacements. Focusons were observed to propagate in the <111> directions at large velocities compared with other directions. Also stable interstitials with a dumbell configuration oriented along the <110> directions were found. In the bcc lattice, the direction of easiest displacement is close to <100> with an estimated threshold energy of 17 eV for the Born-Mayer potential used. These simulations [146, 148] proved the feasibility of simulating radiation damage events on computers which is now indispensable tool for the study of radiation damage.

5.1.3 Modern picture of collision cascades

The collision cascade process occurs on length scales of the order of nm and time scales of the order of ps, which are in the range of affordable atomistic simulations with the computer power available nowadays. The study of radiation damage by computer simulations to date has been basically based on two classes of atomistic numerical models: molecular dynamics and binary collision approximations.

Computer simulations of collision cascades have contributed to the way we understand radiation damage in metals, for reviews see [149, 150, 151, 152, 4]. The actual picture is based on the fact that radiation effects are determined, at the atomic scale, by the number of Frenkel defects, their distribution in clusters and their mobility. A general description of the actual picture of collision cascades and also how the cascades relax, based mainly on the information generated by computer simulations is presented below.

Prior to the creation of a collision cascade is the generation of PKA's, a recoil atom produced by the incident radiation, i.e. neutrons, ion beams, which typically occurs in less than 1 fs. After the creation of a PKA a collision cascade is started where two important stages can be identified: the collisional (or ballistic) phase and the thermal-spike (or cooling) phase.

During the collisional phase the primary knock-on atom loses most of its energy by elastic collisions with the atoms of the crystal during its track along its path. Only a small part of the PKA energy is lost in electronic excitations, which can therefore be ignored in collision dynamics. These collisions provoke a branching 'tree-like' structure of successive collisions which will last for ~ 0.1-0.2 ps. At high energies, distinct regions of damage with identifiable cascades can be identified [153], they are called subcascades. The collisional phase produces a large number of defects creating a hot disordered central region with liquid characteristics surrounded by point defects. Additionally a few interstitials are formed by focused replacement collisions. After approximately 0.1 ps, depending on the energy of the PKA, the number of Frenkel pairs reaches a maximum [154] giving a kinetic energy spectrum far from equilibrium.

Following this collisional phase is the thermal-spike phase, where interstitials, mainly outside the core of the cascade, rearrange by thermal relaxation, in approximately less than 1 ps, returning to a lattice site. During this phase, the energy is partitioned amongst the atoms in the crystal until thermal equilibrium is reached and the spike is dissipated. The disorder on the core may last for several picoseconds, during which time atoms will be seeking for stable configurations by returning to lattice sites or clustering. The thermal spike phase may last between ~ 1 ps until to ~ tens of ps, producing at the end, the final damaged microstructure [155].

The evolution of the final stable defect structure after the collision cascade will change the physical properties of the irradiated material. This evolution occurs over a larger scale of time and length, which is therefore better modelled using continuum and Monte Carlo models [156] because of the longer timescales. However, the starting point for these models is the quantitative knowledge of the number and distribution of the final defects produced by collision cascades provided by molecular dynamics simulations [4].

Molecular dynamics simulations have revealed that defect production is overestimated by analytical models based on binary collisions like the Kinchin-Pease [138] and NRT [142] formulas, Equations 5.1 and 5.2 respectively. The number of Frenkel pairs for a given cascade is 20-40 % of the number predicted by the NRT formula [4]. The number of Frenkel defects created just after the collisional phase, which can be defined as the time at which the kinetic energies of all atoms have fallen below 5 eV, are in a good agreement with the Kinchin-Pease formula [154]. The binary collision models cannot predict the recombinations which are produced during the thermal spike phase due to their many-body interaction nature. Molecular dynamics simulations show that during the thermal spike phase most of the interstitials at the

periphery of the disordered core recombine with vacancies, therefore reducing the number of Frenkel pairs.

Bacon and co-workers have obtained an empirical relationship, between the number of Frenkel pairs remaining after a collision cascade, N, and the energy of the PKA, E_{pka}, which generates the cascade [150, 157, 4]. This empirical relationship is a power law which provides a good fit to molecular dynamics simulations data in several metals such as Ti, Zr, Cu, Zr and Fe (also for the Ni_3Al alloy), as follows:

$$N = A(E_{pka})^m \tag{5.3}$$

where A and m are constants which weakly depend on the particular metal and material temperature. For α-iron these constants have a value of $A = 5.57$ and $m = 0.83$, with a range of validity which has been proven up to energies of the PKA of 40 keV. These values are approximately one quarter of the value predicted by the NRT formula, see Equation 5.2.

Molecular dynamics simulations also reveal the production of clusters of interstitials during the thermal spike phase and by subsequent diffusion driven by the interaction between smaller interstitial clusters. Recent atomistic simulations reveal that the probability of clustering and the size of the clusters tend to increase with increasing PKA energy [4]. These clusters of interstitials can migrate away from the original cascade and be absorbed at sinks of defects, such as bulk interfaces. The mobility of such clusters has been studied in several metals, mainly considering crowdion configurations along close packed directions [158, 159, 160]. Collision cascades simulations in α-iron reveals the presence of large clusters with more than ten members for energies greater than 10 keV [158, 152, 159, 160]. On the other hand, there is no clear evidence, until the date, for the presence of large clusters of vacancies from cascade simulations in α-iron [152, 156, 4].

5.1.4 Radiation damage and grain boundaries

The performance of steel components in nuclear reactors is significantly influenced by the presence of interfaces within the material such grain boundaries. Grain boundaries in polycrystalline materials, i.e. ferritic steels (based on bcc iron) used in nuclear reactors, affect a large variety of physical properties [161, 36]. The analysis of the role that interfaces play in respect of the damage produced by radiation is quite difficult experimentally. Atomistic simulations are therefore an ideal alternative to provide an insight into the structure, changes and damage mechanisms near to grain boundaries under irradiation.

Changes in microstructure due to radiation may result in the segregation of impurities to grain boundaries, which may in turn degrade the structural properties. This segregation can affect many metallurgical processes including fracture, corrosion, recrystallization, grain growth, creep, environmental embrittlement and grain boundary diffusion [162, 163, 161].

Most of the research to the date has studied collision cascades, using computer simulations, in perfect crystals, investigating the type and energy of defects and the way in which the defects are formed. However, it is known that bulk interfaces such as grain boundaries in the material play an important role in the degradation of structural properties.

The natural step to improve the understanding of the role of grain boundaries in defect production is the study of collision cascades near these interfaces. Recently such simulations of radiation damage near interfaces in iron [164, 165] and silver [166] have been reported.

5.1.5 Chapter description

The object of this part of the thesis is to gain an insight into how radiation damage affects grain boundaries. The initial step in the modelling of radiation damage near these grain boundaries is to model the static microstructure for a better understanding of the atomic structure at the interface of two matching crystals, which has been discussed in the previous chapter. The second step involves the simulation of collision cascades in bicrystals containing theses interfaces, which is the objective of this chapter.

In this chapter atomistic simulations of collision cascades near grain boundaries in α-iron are presented. The dynamics and effects of the collision cascades have been studied via molecular dynamics. The effects of collision cascades with PKA's of 1keV of initial energy, in symmetrical tilt and twist boundaries are analysed. A description of the molecular dynamics procedure applied to perform the calculations is presented, including a description of the computational blocks used and the choice of the primary knock-on atom. Results are presented for both, a (530) symmetrical tilt boundary and a [001] 28.073° (001) twist boundary. Analysis of the statistics generated by the calculations including the evolution of the number of defects within grain boundaries and changes in configurational energies are presented.

5.2 Modelling radiation damage near grain boundaries

5.2.1 Molecular dynamics procedure

In this research molecular dynamics simulations have been employed to study the evolution of a collision cascade generated by a single PKA near symmetrical grain boundaries.

In order to generate a collision cascade near an interface, an excess of kinetic energy is imparted to an atom, i.e. a PKA, chosen from a relaxed computational block containing such an interface. The procedure to obtain relaxed structures containing symmetrical grain boundaries has been explained in the previous chapter. The energy of the PKA has to be chosen according to the computational resources available. For larger energies of the PKA, larger computational blocks are required to contain the whole cascade. The initial temperature of the relaxed computational block is 10 K. Therefore, the atom chosen to be the PKA, and indeed all atoms in the lattice, maintain a little vibrational energy. This small vibrational energy is increased by the excess of kinetic energy added. In this thesis PKA's with 1keV have been considered.

The choice of the PKA gains more importance in simulations of collision cascades near interfaces compared to simulations in a perfect crystal. When the crystal contains an interface, the effects produced by a cascade originated at different distances from it will be different. The initial velocity direction of the PKA plays a major role for cascades near interfaces as well as in perfect crystal simulations. Different choices of velocity directions and distances of the original PKA from the interfaces provide the statistics necessary to draw conclusions from the simulations.

The interatomic potential used to describe the interactions between Fe atoms has been used also to obtain the relaxed structures of the computational blocks containing the grain boundary. This potential is the original Finnis-Sinclair potential for α-iron, but modified to properly describe the close interactions produced during the collision cascade [37], as described in Chapter 2.

Periodic boundary conditions are applied in directions parallel to the boundary plane during the simulation time. Free boundary conditions are used in the direction perpendicular to the boundary.

The simulation is allowed to evolve until reaching a stable state with no significant evolution in the number of point defects created by the collision cascade, i.e. typically 5 ps with 1 keV imparted to the PKA. Major changes in the kinetic and configurational energy of the system will be produced during the first picosecond when the

maximum number of interactions occurs, i.e. the collisional phase. Then, the kinetic energy of the system is reduced by introducing a damping proportional to the velocity of the atoms until the temperature of the system drops to the initial temperature of the relaxed computational block which was 10 K, during approximately 2 ps more.

A variable time-step is used to integrate the equations of movement, being smaller during the collisional phase where abrupt changes on kinetic energies are produced, and being subsequently increased in order to increase the speed of the simulation. The time-step, Δt, has been chosen according to the simulation time, t, in the following way:

$$
\begin{aligned}
\Delta t &= 0.1 \text{ fs}, \quad 0 < t \leq 0.05 \text{ ps} \\
\Delta t &= 0.2 \text{ fs}, \ 0.05 < t \leq 0.2 \text{ ps} \\
\Delta t &= 0.4 \text{ fs}, \quad 0.2 < t \leq 0.5 \text{ ps} \\
\Delta t &= 0.6 \text{ fs}, \quad 0.5 < t \leq 1 \text{ ps} \\
\Delta t &= 1 \text{ fs}, \quad\quad 1 < t \leq 5 \text{ ps} \\
\Delta t &= 2 \text{ fs}, \quad\quad\quad t > 5 \text{ ps}
\end{aligned}
\tag{5.4}
$$

Total energy is conserved during the whole event, prior to the damping process, with this choice of the time-step. Negligible fluctuations in the total energy, $\Delta E / E$, are not allowed to be bigger than 0.001 %.

5.2.2 Interstitials and vacancies

Point defect production is the immediate effect of a collision cascade, and therefore the way in which they are quantitatively defined plays a key role in data analysis. A vacancy is defined as a lattice site with no atoms inside a certain radius centred at the lattice site. An interstitial is an atom which is placed away from a lattice site by a distance bigger than this radius.

An important question arises when we consider whether it makes sense to define a vacancy or an interstitial at the interface using the same definition that the one employed in a perfect crystal. The atomic arrangement at the grain boundary is different from that of the bulk and also different between different grain boundaries. The first neighbour distances are not the same as at the bulk. In a perfect crystal every atom has a first neighbour at the same distance however in the boundary the first neighbour distance is dependent on the position at the boundary. However, despite all the above facts it seems more plausible to have a single definition for both in the bulk and at interfaces, instead having one definition for the bulk and a different one which will be dependent on the specific interface.

In this thesis vacancies and interstitials are defined at the interface following the same criteria as that used in the bulk of bcc iron. Here, we define a vacancy as a site in the undisturbed relaxed lattice which has no atom within a sphere of radius of 0.3 a_0 [37], where a_0 is the lattice constant, and interstitials being atoms placed outside these spheres centred in each site lattice. The lattices sites are defined as those of the relaxed structure before the collision cascade [164].

The study of clusters of interstitials is also based on the usual definition employed for collision cascades in perfect crystals [37]. An interstitial atom is considered to be in a cluster of interstitials if its distance to any of the atoms belonging to the cluster is less than the first neighbour distance of the crystal; i.e. the first neighbour distance equals 0.866 a_0 in a bcc lattice.

5.3 Radiation damage near tilt grain boundaries

In this section results of collision cascade simulations near a symmetrical tilt grain boundary are presented.

5.3.1 Collision cascade details

A rectangular computational cell has been chosen to study the radiation effects produced by single collision cascades near a tilt boundary. This computational block is a bicrystal which forms a (530) symmetrical tilt boundary placed on the centre of the block. The x-z plane is chosen to be parallel to the boundary planes in both crystals, i.e. (530) and (350). Following the coincident site lattice model, a (530) symmetrical tilt boundary is characterised by a misorientation angle equal to 28.073°, and a rotation axis parallel to the [001] direction, i.e. y axis. Also a rigid body translation of one of the halves equal to $T_x = 0.21$ was applied, the block was relaxes as explained in the previous chapter.

The dimensions of the computational block are equal to $100.5 \times 100.5 \times 42.0$ Å which contains 36900 atoms. This size of the computational block is big enough to contain collision cascade simulations produced by PKA with an excess of kinetic energy equal to 1 keV.

In order to generate statistics, various velocity orientations for the PKA are chosen and applied to PKA's at different distances from the grain boundary. Table 5.1 shows the collision cascades considered near the tilt boundary. In this table the distance to the grain boundary plane and the velocity directions of the PKA are specified. Seven different PKA directions are considered, including PKA's moving perpendicular to the

133

interface, i.e. [530] direction, and parallel, i.e. [001] direction. An excess of kinetic energy of 1 keV is considered for the PKA's in all cases. At least four different collision cascade for each velocity direction were simulated by choosing PKA's at different distance from the boundary resulting in a total of 28 collision cascades. The distances from different PKA's to the boundary are between 6-40 Å. At this energy, 1 keV, a collision cascade initiated at distances of the boundary bigger than approximately 40 Å will hardly affect the grain boundary.

PKA Directions	PKA distance from the interface (Å)	PKA Energy(keV)
[530]	9.5 17.9 26.3 31.7 38.0 43.0	1
[350]	7.6 9.5 13.5 17.9	1
[001]	6.1 9.5 13.0 18.4	1
[100]	7.6 10.5 13.5 20.8	1
[210]	8.0 9.5 13.5 14.9	1
[110]	6.5 7.6 9.5 9.5	1
[111]	14.5 17.4 19.9 22.8	1

Table 5.1: Collision cascades considered near the symmetrical tilt boundary

5.3.2 Cascade evolution

Before analysing the final damaged configuration of the grain boundary structure as effect of the collision cascade, this section deals with the evolution of the cascade through the simulation time.

In Figure 5.2 the typical kinetic and potential energy evolution of the computational block during the simulation time is showed. The collision cascade simulation starts when an excess of 1 keV of kinetic energy is imparted to the primary knock-on atom increasing the total energy of the system by this amount. The behaviour of the kinetic and potential energy through the collision cascade process is similar to those in a perfect crystal. The biggest change of energies is produced during the first half picosecond, where the kinetic energy excess of the PKA is transmitted to the system by the collision events. The kinetic energy is reduced during this first stage of the collisional phase to approximately 500 eV, half of the initial available energy. Meanwhile, the potential energy abruptly increases to reach a more stable value after 1-2 ps of the simulation, see Figure 5.2 (a) and (b). After this time the system does not suffer large energy fluctuations. After 5 ps of simulation, a damping term proportional to the velocity was introduced to reduce the kinetic energy of the
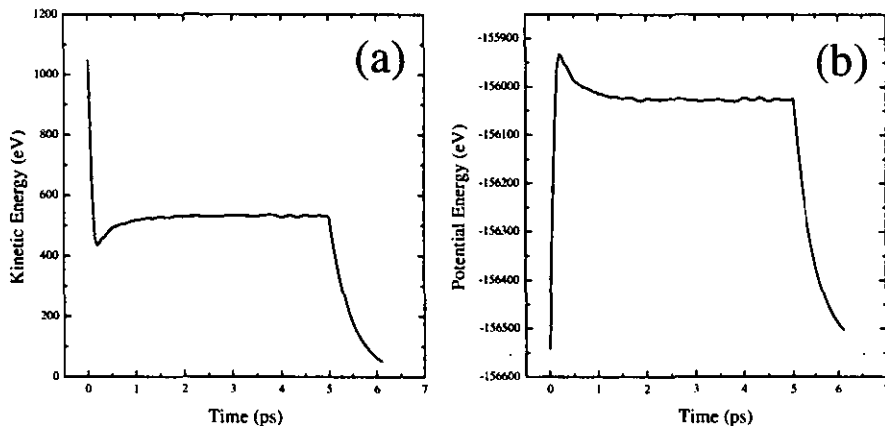
Figure 5.2: Kinetic (a) and potential (b) energy evolution for a typical collision cascade near a (530) symmetrical til boundary.

system until the system reaches 10 K of temperature; the initial temperature of the computational block. This damping stage last approximately 1-2 ps more.

The number of defects created during the collision cascade has been obtained at different intervals of the simulation time. In Figure 5.3, the number of Frenkel pairs, i.e. number of interstitial-vacancy pairs, created by the collision cascades studied, as a function of the simulation time is presented for the (530) symmetrical tilt boundary. It is clearly shown that the maximum number of defects is produced during the first half picosecond, as in a perfect crystal. After the first picosecond most of the defects relaxed and we consider that we have stable defects after about 6 picoseconds of the simulation time. For comparison, it should be mentioned that Bacon's power law, see Equation 5.3, predicts approximately 6 Frenkel pairs in perfect crystal of α-iron as a result of a cascade energy of 1 keV. The presence of interfaces clearly increases the damage of the system.

Data visualisation is an important tool to qualitatively analyse the results provided by molecular dynamics simulations and follow the evolution of the system. With the help of data visualization the mechanisms happening at the atomic scale can be more easily studied. The collision cascade simulations studied in this work have been tracked by mainly saving the positions of interstitials and vacancies at regular intervals depending on the stage of the simulations. These data have been typically saved every 5 fs during the first two picosecond of the simulation when more collisions occur and then every 10 fs and 20 fs once the system is relaxing and less events occur. With these data it is possible to make snapshots at the required simulation time by plotting vacancies and interstitials in a three dimensional like
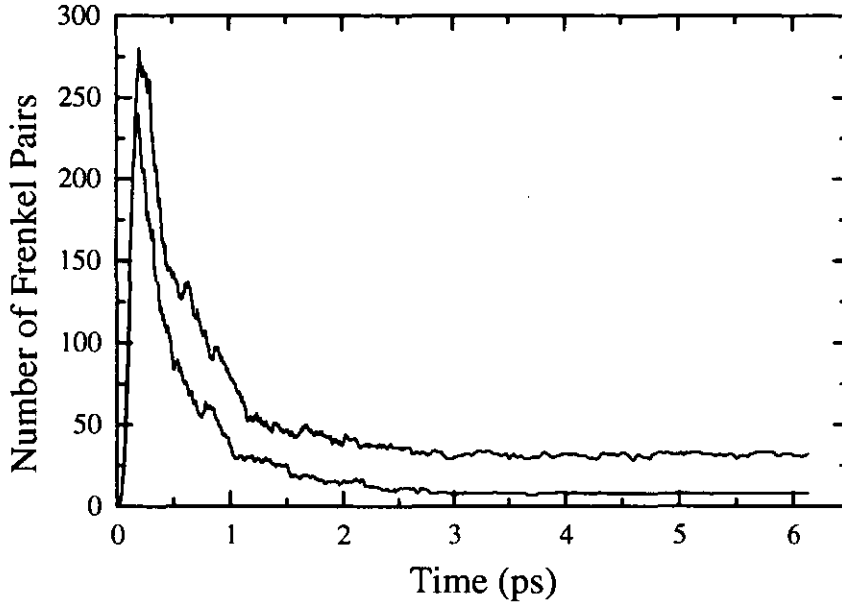
135

Figure 5.3: Number of Frenkel pairs, generated for 1 keV collision cascades as a function of the simulation time in the (530) symmetrical tilt boundary model. The two curves represent the upper and lower limits for the number defects from the simulations carried out.

representation. Also, movies of the simulation have been made by sequencing the snapshots at different times.

Figures 5.4 and 5.5, show three-dimensional pictures at different stages of the simulation for two different collision cascades. Figures 5.4 and 5.5 are samples of collision cascades near the symmetrical tilt boundary considered for normal and parallel incidence, respectively, of the initial velocity direction of the PKA with respect to the interface. In these pictures interstitials and vacancies are represented as green and red spheres respectively. The position of the interface in the computational block is drawn as a transparent gray plane. Also the limits of the rectangular computational block are drawn as a black lines.

Data visualitation shows that the cascade develops typical features observed in perfect crystal lattices by previous studies in metals with this energy. Vacancies form along the way of the PKA and replacement collision sequences emanate out from this track. After the maximum number of defects is reached during the first half picosecond, recombinations take place leaving a number of stable defects such as dumbells at the end of the replacement collision sequences and the vacancies along the track of the PKA.
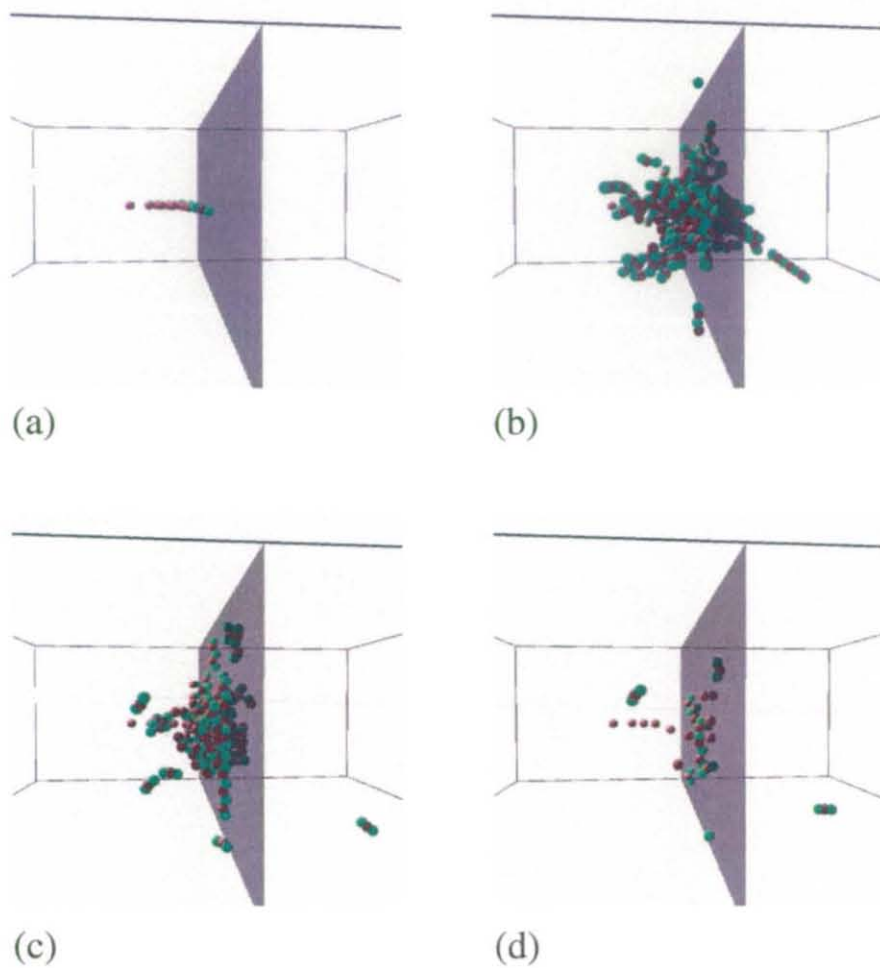
Figure 5.4: Various stages in the development of a typical 1 keV collision cascade near the [001] 28.073° (530) symmetrical tilt boundary at normal incidence to the boundary. The PKA was chosen to be at a distance of 18.4 Å from the boundary. The red circles represent vacancies and the green circles interstitials. a) 0.05 ps; b) 0.225 ps; c) 0.5 ps; d) 6 ps.
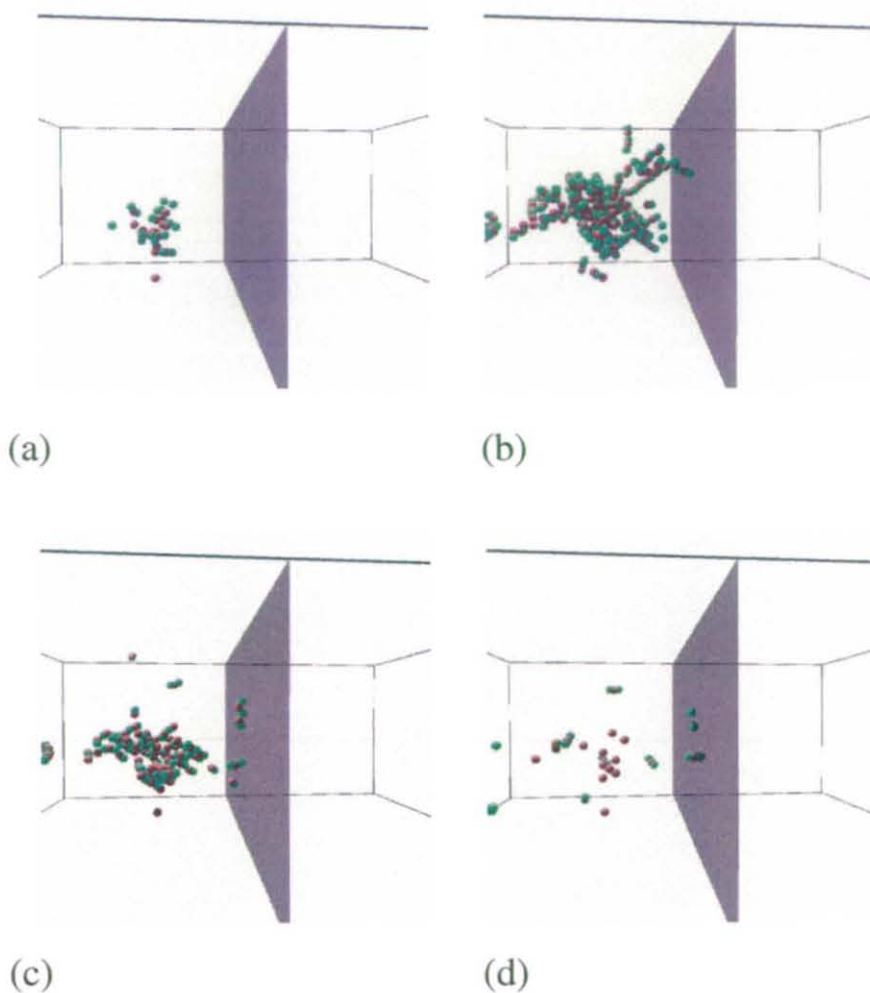
Figure 5.5: Various stages in the development of a typical 1 keV collision cascade near the [001] 28.073° (530) symmetrical tilt boundary at parallel incidence to the boundary. The PKA was chosen to be at a distance of 18.4 Å from the boundary. The red circles represent vacancies and the green circles interstitials. a) 0.05 ps; b) 0.225 ps; c) 0.5 ps; d) 6 ps.

The usual evolution of the collision cascade changes when the collision cascade spreads reaching the vicinity of the boundary. The main difference between cascades initiated in perfect crystals is that in this case the grain boundary acts as a partial barrier to the collision cascade. Few focused collisions cross the boundary at this PKA energy and an accumulation of defects occurs in the boundary region. This is easily understood considering that focused collisions follow close packed directions in the crystal, such as the [111] direction. Focused collision cannot continue its evolution across the boundary, because this direction is not a close packed direction in the other half of the bicrystal.

The conclusion to be drawn from the qualitative analysis provided by data visualisation is that the grain boundaries do act as a region where collision cascade damage can accumulate. Generally the boundary region acts as a region where defects build-up. These occur either as a result of rearrangement of existing interface atoms or as a build-up of interstitials arising from outside the boundary region. The final damaged accumulation of defects occurs in the boundary region changing the atomic structure of the boundary. A more detailed analysis of the final atomic structure is the subject of the next section.

5.3.3   Preferential sites in the boundary region

The damage produced in the grain boundary region as an effect of the collision cascade is much bigger than the one produced in a perfect crystal lattice. A question of great interest is to know whether this damage is randomly distributed along the boundary or by contrast, if it is accumulated in special regions at the grain boundary.

In Figure 5.6, the position of all the defects which end up at the grain boundary after the radiation process is shown in a magnified region of the interface. This figure presents two different views of the initial structure of the grain boundary, open circles, plus the positions of all the interstitials, solid red circles, and vacancies, solid black circles, generated for all the simulations. Since this picture consists of position of the defects averaged aver all simulations we can see that there are specific sites in the boundary which are preferred.

The majority of interstitials produced as a effect of radiation at the grain boundary are in a region which is very localised in the centre of the structure, see Figure 5.6 (b). If we consider only defects inside the width of the boundary, defined in the previous chapter, i.e. 17Å , 85 % of them are in a region of 3.8 Å which is defined by the distance cc' of the 'kite' shape in the periodic structure of the boundary, see diagram
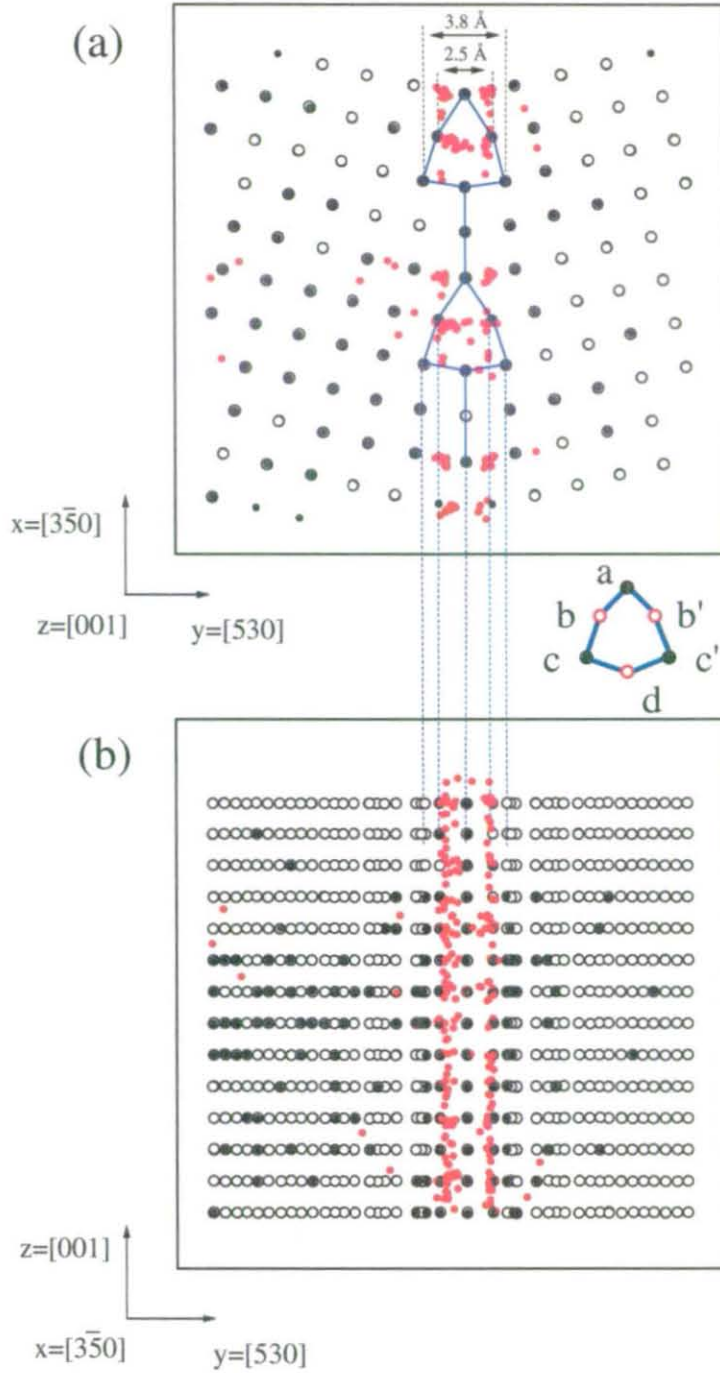
Figure 5.6: Open circles are the projection of atomic sites of the (530) symmetrical tilt before the collision cascade process in different views: (a) top view, (b) front view. Black and red solid cicles are the projections of vacancies and interstitials respectively, plotted for all the simulations.

in Figure 5.6. This percentage being of 75% for interstitials inside the width defined by the bb' distance, which is equal to 2.5 Å.

One of the most important result from this simulations is that there are 'preferential' sites in the periodic structure where interstitials stay after radiation, changing the local atomic structure of the interface. These 'preferential' sites are identified in Figure 5.6(a) as and accumulation of red solid circles near the vertexes a and b (b') of the 'kite' shape. Interstitials are hardly found between the 'kite' shapes along the grain boundary structure.

The preferential formation of defects at grain boundaries compared with those produced in the bulk crystal is known since the 1960's after experimental studies of irradiated platinum foils [167]. Preferential damage at specific sites have been recently observed in selected atomic columns of tilt grain boundaries in silicon [168].

5.3.4 Defects at the boundary

An important issue is the appearance of clusters of interstitials after radiation in the grain boundary region. The definition of clusters of interstitials is the usual one used in a perfect crystal. Therefore, an interstitial atom is considered to be in a cluster of interstitials if its distance to any of the atoms belonging to the cluster is less than the first neighbour distance of the bcc structure.
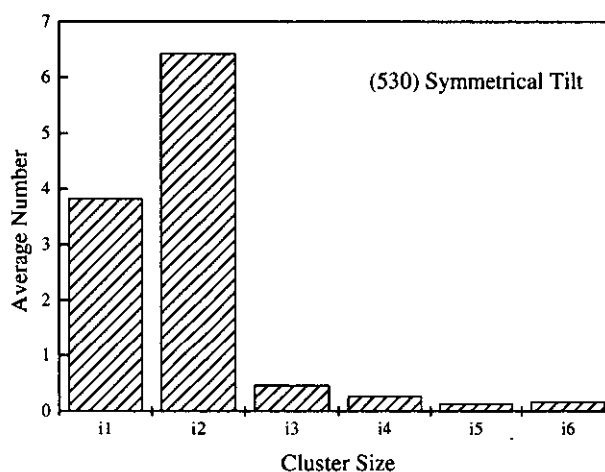

Figure 5.7: Cluster frequency of interstitials after collision cascades near a (530) symmetrical tilt boundary
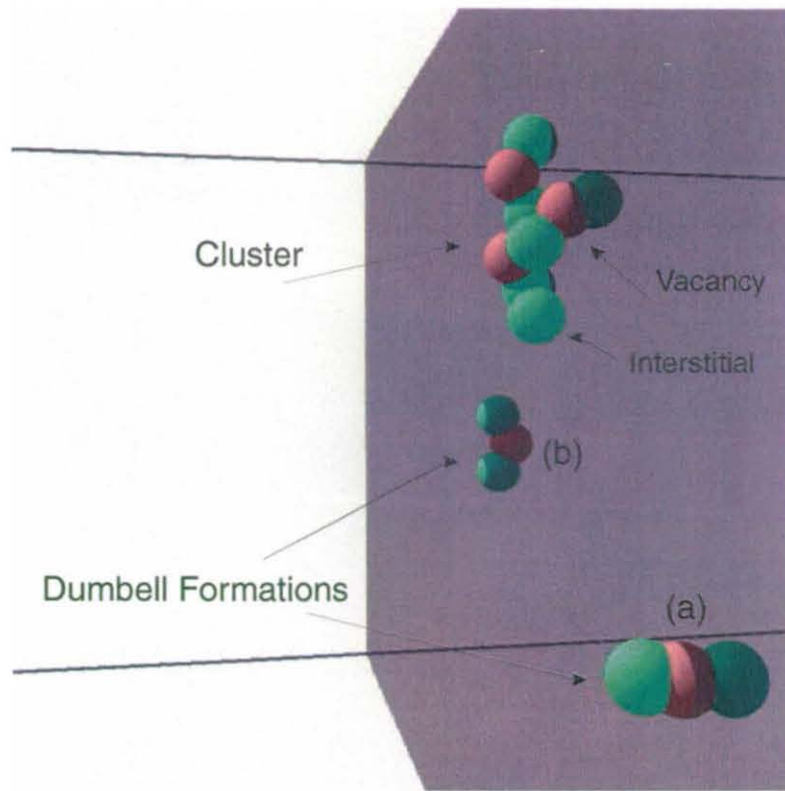
Figure 5.8: Typical defects at the boundary

In Figure 5.7 the frequency of interstitial cluster sizes in collision cascades near a (530) symmetrical tilt boundary is presented. The results have been averaged over the 28 collision cascades studied. As it can be inferred from this graph, the most frequent clusters remaining after the collision cascades are composed of two interstitials. Single interstitials are also frequent and even clusters with 6 interstitials have been found in the boundary region.

After a detailed study, the most frequent clusters of interstitials, which are composed of two interstitials, have been observed to form in the 'preferential' sites of the atomic structure described in the previous section. These, are kind of dumbells with two interstitials sharing a vacancy site. More specifically two types of dumbells have been observed: one consisting in a vacancy on the middle of the interface and interstitials symmetrically placed in both sides perpendicular to the boundary plane and straddling it, type 'a', as is shown in Figure 5.8; the other kind of dumbell consisting in a vacancy on the boundary plane and interstitials placed symmetrically placed respect to the vacancy parallel to the boundary plane, type 'b', see Figure 5.8. Defects type 'a' and 'b' (or b') are in the preferential sites near the 'a' and 'b' vertexes respectively of the 'kite' shape, see Figure 5.6.

5.3.5 Two mechanisms

Two mechanisms which may lead to the production of the dumbells configuration found, have been identified to be replacement collisions along the boundary region. Figures 5.9 and 5.10, show schematically the last stage of two replacement collisions giving as a result a dumbell of type 'a' and another one of type 'b', respectively.

In Figure 5.9 (a) a top view along the rotation axis of the (530) symmetrical boundary region after a collision cascade is presented. Solid black circles and open red circles represent adjacent layers along the rotation axis where the dumbell type 'a' is formed. In this figure squares represent the original configuration before the collision cascade forming the structural unit in the form of a kite is indicated by a blue dotted line. Figure 5.9 (b) is a magnification of the front view where the dumbell type 'a' is formed. Circles in different colours indicate different adjacent atomic layers along the rotation axis. A sequence of collisions, a0...a4, can be follow in Figure 5.9. This example shows a series of collisions which arrives to the grain boundary region following a [111] direction. The first parts of the sequence, a0, a1 and a2, consist of a replacement collision where an atom is knocked by another one coming from a top layer, following a [111] direction, then the knocked atom goes to the bottom layer being its site replaced by the previous one. The final result is an interstitial atom, a2, which provokes one atom on the atomic mirror plane to move away creating a vacancy and an interstitial, now forming the dumbell type (a). Some minor reorderings are produced in neighbouring sites, a4. These type a dumbells are always produced with a vacancy in the 'a' vertex of the structural unit with 'kite' shape.

In Figure 5.10, a collision sequence leading to a dumbell type 'b' is shown. Figures 5.10(a) and (b), represent projections of atoms in a plane perpendicular to the rotation axis and parallel, respectively. In this case the sequence of replacement collision is moving in the boundary and parallel to it. The final result is the dumbell formed by two interstitials, b7 and b8, and a vacancy which are aligned parallel to the boundary. This formation is produced in the first adjacent layer parallel to the atomic mirror plane, being the vacancy in the 'b' vertex of the 'kite' shape. This mechanisms show how defects can be conducted easily along the boundary.

Movies and data visualisation reveals that many of the replacement collision sequences generated outside the boundary stop at the boundary. When the sequence arrives at the symmetrical tilt boundary region this is absorbed by another replacement collision but parallel to the boundary and inside the boundary region. The defects created by this collision will recombine leaving defects as the dumbell configurations previously explained or in form of clusters, see Figure 5.9. The second
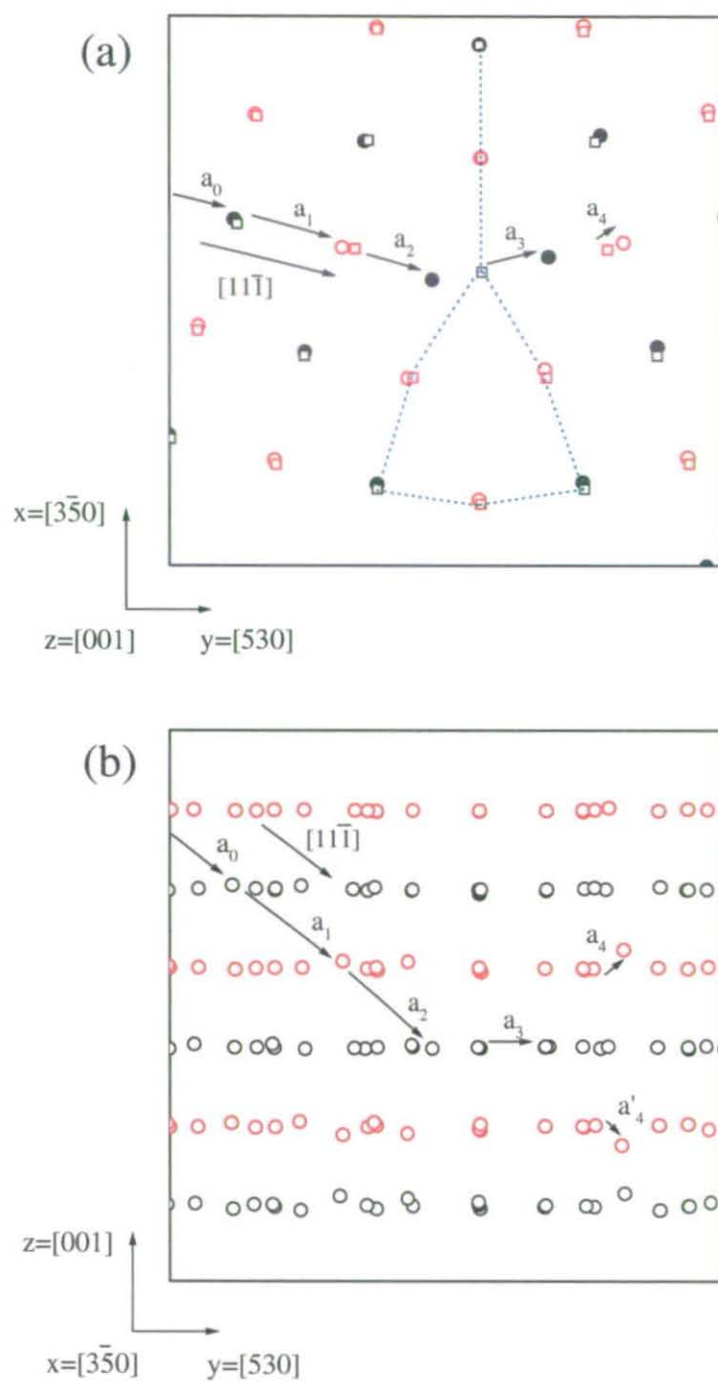
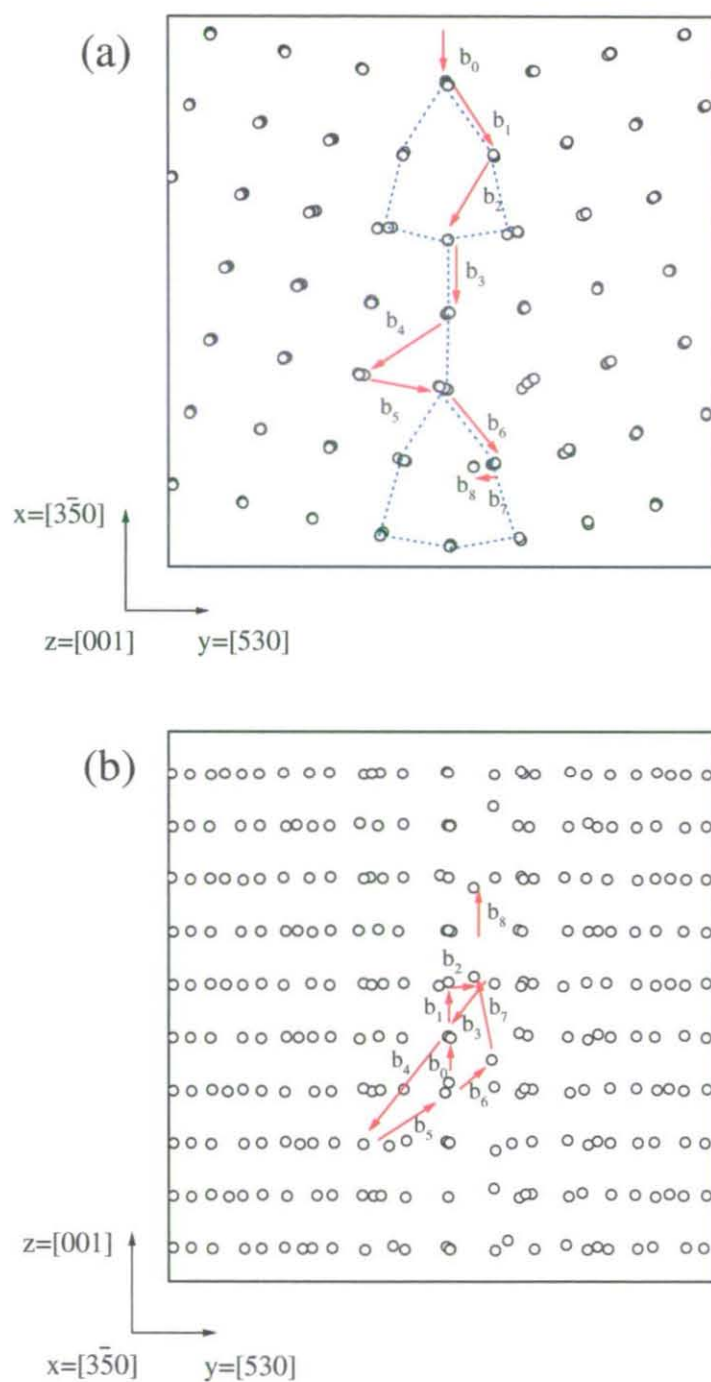Figure 5.9: Collision sequence with a defect type 'a' as a result

144

Figure 5.10: Collision sequence with a defect type 'b' as a result

145

mechanism presents the grain boundary as a region where a sequence of replacement collision can easily travel, see Figure 5.10. The fact that grain boundaries can 'conduct' vacancies in a way which is highly directional, along the boundary, was envisaged in the 1960's after a bombarding study of alpha-particles in metals [169].

5.3.6 Grain boundary energy

The new local rearrangement of atoms produced in some parts of the boundary changes the configurational energy. Effects produced by radiation damage at the boundary can be analysed via the study of these changes. In the previous chapter analysis of the configurational energy was made by computing the average potential energy of the atoms including in slabs parallel to the boundary. The same procedure is now used but with the final configuration energy after the collision cascade.
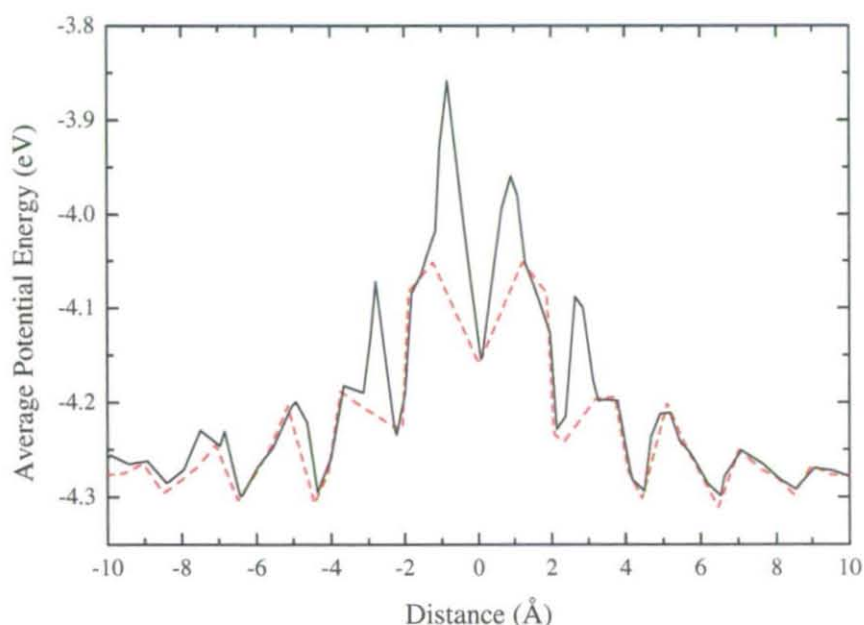

Figure 5.11: Average potential energy of slabs of atoms at the grain boundary region: the dotted line represents the relaxed (530) simmetrical tilt configuration, and the solid line the damaged configuration averaged over all the collision cascade studied.

In Figure 5.11, the averaged potential energy of atomic layers in the grain boundary region is presented, before and after the collision cascade. The values for the energy profile after radiation damage have been averaged over all the simulations performed on the symmetrical tilt model. As can be seen in Figure 5.11, the changes

produced at the boundary maintain an almost symmetrical shape on the energy profile. Bigger changes with respect to the relaxed configuration are in a central region of approximately 7 Å with major changes produced in the positions of the atomic planes adjacent to the mirror atomic plane, where the preferential sites are. Changes outside this region are negligible. These small changes observed to the left of the boundary is due to that the collision cascades which were initiated from this side and some damage in form of vacancies and interstitials in the bulk remained. Also, the width of this boundary after radiation damage can be inferred from the previous study, showing a slightly increase with the original width equal to 17 Å, in about 1 Å.
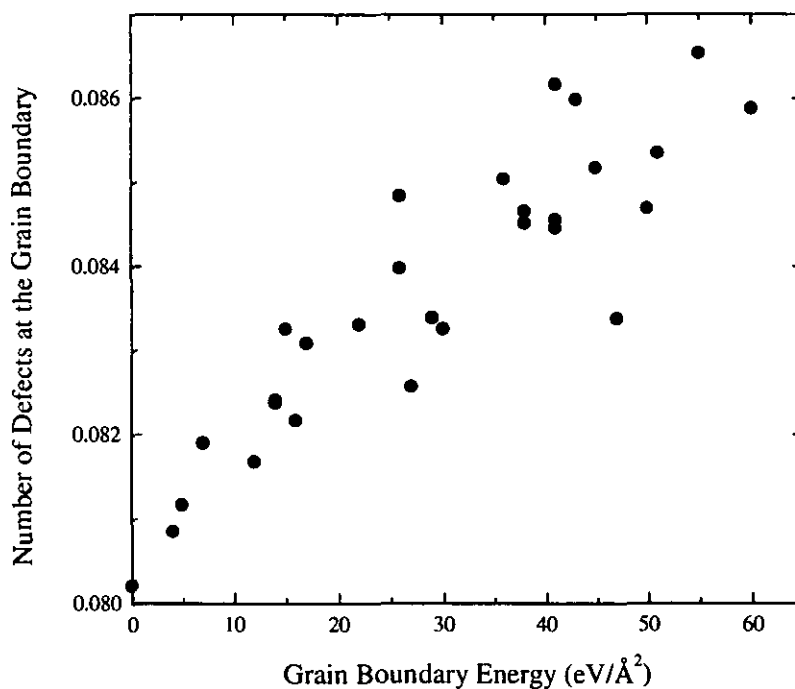

Figure 5.12: Grain boundary energy as a function of the final number of defects inside the grain boundary width for all the collision cascades simulated near a (530) symmetrical tilt boundary.

The grain boundary energy of the interface after radiation damage has been also calculated considering the configurational energy of the atoms inside the width of the grain boundary a the end of the simulation, as explained in the previous chapter. Results shows that the configurational energy is increased in the damaged boundary, because of the defects introduced in its structure

In Figure 5.12 the number of final defects inside the width of the grain boundary, is plotted against the grain boundary energy for all the simulations performed in this

boundary. The grain boundary energy shows a clear increase with the number of defects at the boundary following an almost linear tendency.

5.4 Radiation damage near twist grain boundaries

In the following section results arising from collision cascades simulations near a symmetrical twist boundary are presented.

5.4.1 Collision cascade details

Collision cascades have been simulated near two different models of a (001) 28.073°; one of them with the relaxed structure of the boundary without rigid body translation and the other with a rigid body translation in a plane parallel to the boundary given by $T_x = 0.22$ and $T_z = 0.75$. Both relaxed structures are described in the previous chapter of this thesis.

The interface between both crystals making the bicrystal is placed on the middle of the computational cell, with the plane parallel to the x-z plane. The dimensions of the computational block are equal to $83.7 \times 71.0 \times 83.7$Å containing 42500 atoms. This size of the computational block is big enough to contain collision cascade simulations produced by PKA with an excess of kinetic energy equal to 1 keV.

Table 5.2 shows all the collision cascades considered for the twist boundary. In this table the distance to the grain boundary plane and the velocity directions of the PKA are specified. Five different PKA directions are considered, including PKA's moving perpendicular to the interface, i.e. [530] direction, and parallel, i.e. [001] direction. An excess of kinetic energy of 1 keV is considered for the PKA's in all cases. At least three different collision cascade for each velocity direction were simulated by choosing PKA's at different distance from the boundary resulting in a total of 15 collision cascades.

PKA Directions	PKA distance from the interface (Å)	PKA Energy (keV)
[010]	14.2 8.5 25.7	1
[001]	2.0 8.4 17.1	1
[210]	5.6 11.3 15.7	1
[110]	8.4 15.6 22.8	1
[111]	7.0 11.3 17.1	1

Table 5.2: Collision cascades considered near the symmetrical twist boundary

5.4.2 Cascade evolution

The evolution of the collision cascades near the twist boundaries has the same characteristics as those in the tilt boundary simulations. A similar study based on the evolution of the number of defects with the aid of data visualisation has been performed.

In Figure 5.13 the number of final Frenkel pairs as a function of the simulation time is presented for both models of the twist boundary considered. This graph shows that the final number of defects for both models is very similar, being slightly smaller for the model with rigid body translation. However, a comparison of Figures 5.13 and Figure 5.3, reveals that the number of defects at the end of the simulation time is always bigger for collision cascades near twist boundaries compared with those in tilt boundaries. The number of final point defects in the symmetrical twist boundaries produced by a 1 keV collision cascades is approximately four times the number of point defects of the same kind of collision cascades in the symmetrical tilt boundary considered.
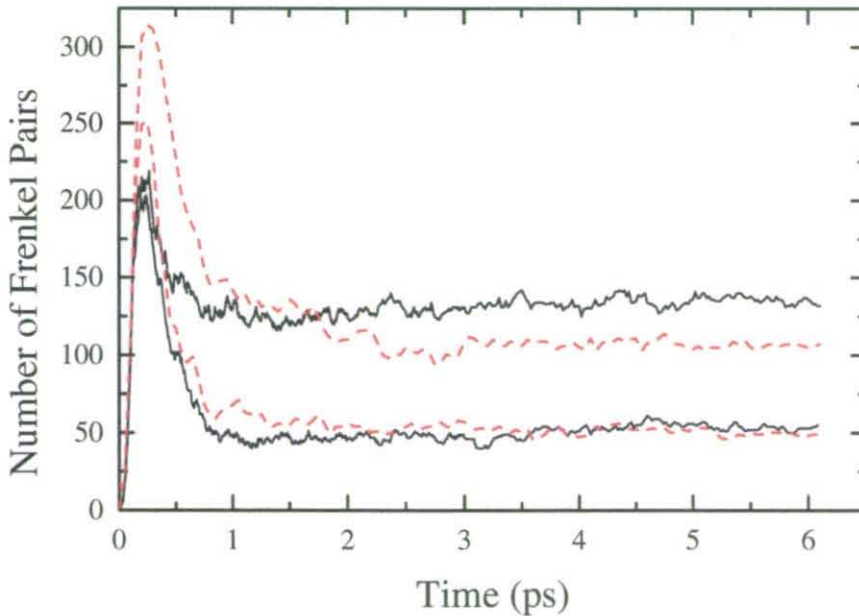
Figure 5.13: Number of Frenkel pairs, generated for 1 keV collision cascades as a function of the simulation time near the [001] 28.073° [001] symmetrical twist boundary model. Solid line and dashed are the values of the cascade near the model with and withouth rigid body translations respectively. The two curves for each model represent the upper and lower limits for the number defects from the different simulations carried out.

As in the case of symmetrical tilt simulations, sequences of snapshots at different stages of the simulations are presented in a couple of examples for the twist boundaries. Figures 5.14 and 5.15, present three-dimensional pictures of four different stages for a collision cascade with normal incidence to the boundary and a parallel one, respectively.

Again, data visualisation shows how the grain boundary acts as a barrier for the collision cascade, however, in some cases like the one presented in Figure 5.14, some focused collisions can produced stable defects such as dumbells on the other side of the interface. Final snapshot of the sequence, from the previous figures, show a clear increasing of defects placed at the boundary compared with the collision cascades simulations in the tilt model.

5.4.3 Grain boundary energy and final configuration

The initial grain boundary energy of both models before being damaged by the collision cascade was equal to 0.123 eV/Å and 0.117 eV/Å for the symmetrical models without and with translation respectively. This energy was expected to increase as a effect of radiation like it did in the case of the symmetrical tilt boundary. However, results arising from collision cascade simulations near the model without rigid body translations, revealed that the grain boundary energy decreased after radiation. In some cases the grain boundary energy decreases by about 2.5% of the initial value. Simulations applied to the second model also decrease the grain boundary energy of the initial configuration however, this changes are less noticeable than with the first model.

The configurational energy profile is presented in Figure 5.17 for the grain boundary region in the [001] 28.073° (001) after radiation damage. The resultant profile has been averaged over the 15 cascades studied. As it can be seen no major changes are produced with respect to the profile of the relaxed configuration.

This results suggest that the atomic configuration of the twist boundaries employed for the simulations, might not be optimal as we would expect an increase in energy after radiation. This is also supported with the fact that after the collision cascades, the configurational energy profile has no big changes, see Figure 5.16 in both models studied, compared with the tilt model where big changes on energy appeared in the closest atomic layers to the middle of the boundary.

In Figure 5.17 the averaged number of interstitials as a part of clusters are presented, for the two twist model studied. A big amount of defect clustering occurs in

Figure 5.14: Various stages in the development of a typical 1 keV collision cascade near the [001] 28.073° (001) symmetrical twist boundary at normal incidence to the boundary. The PKA was chosen to be at a distance of 14 Å from the boundary. The red circles represent vacancies and the green circles interstitials. a) 0.05 ps; b) 0.225 ps; c) 0.5 ps; d) 6 ps.
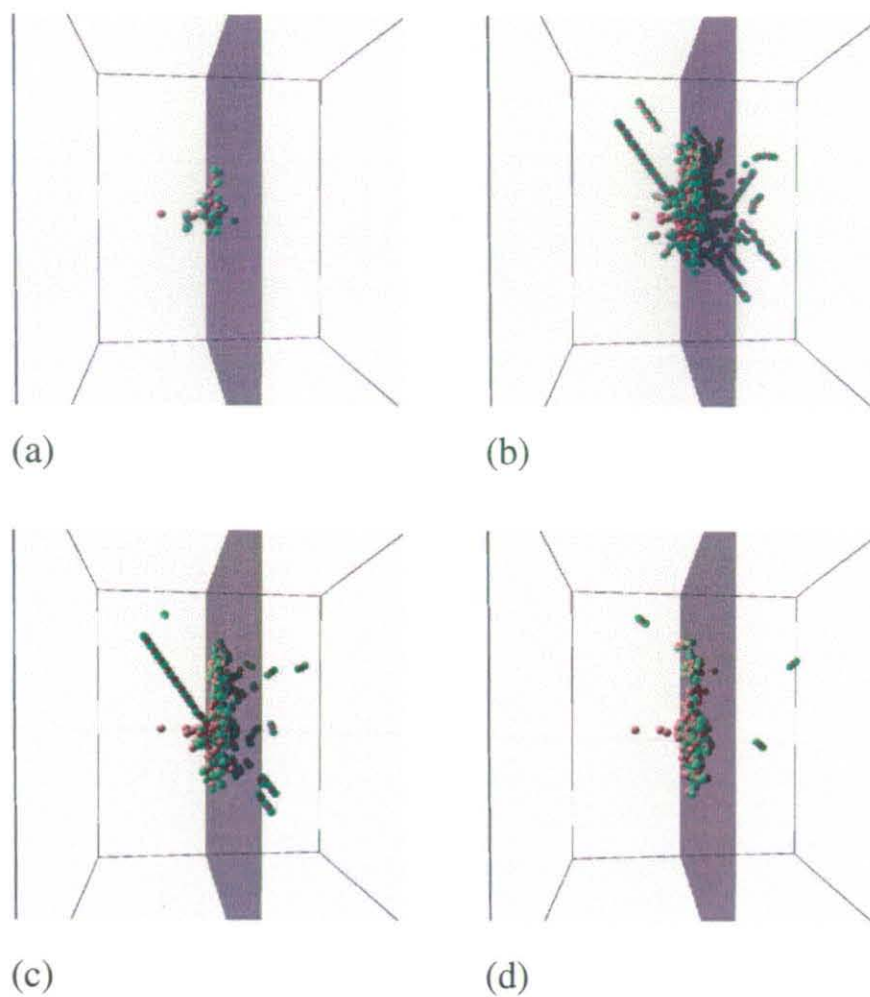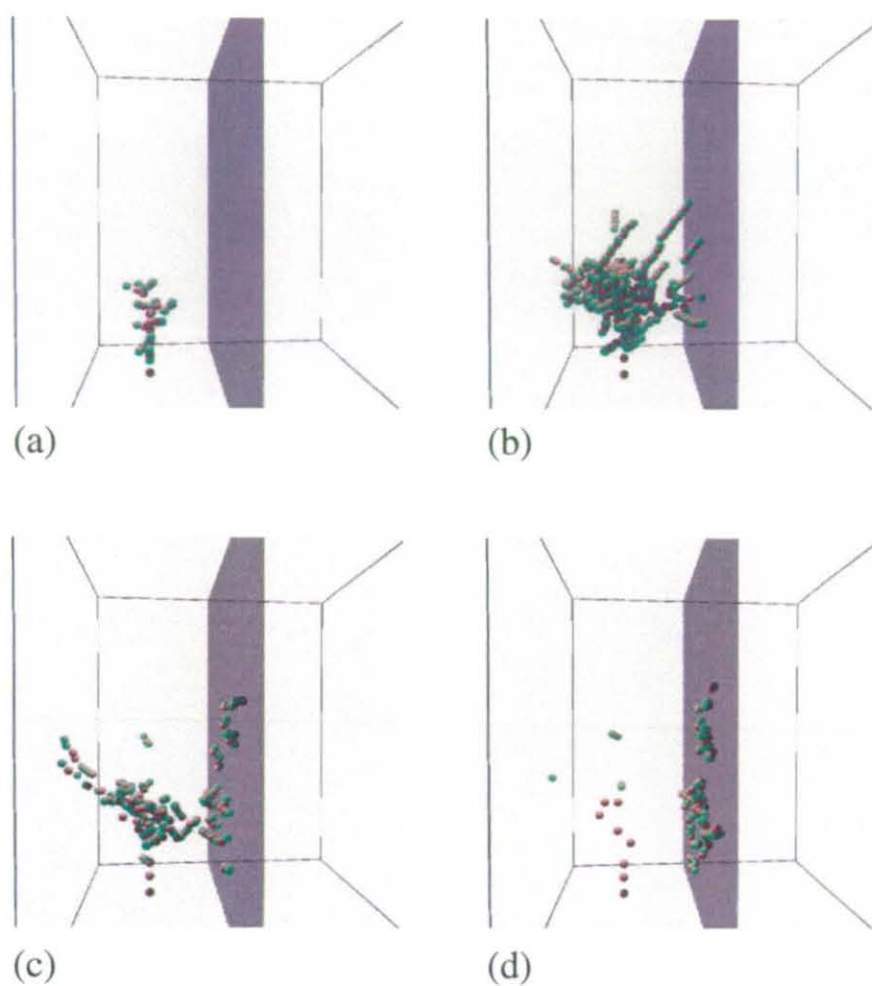
Figure 5.15: Various stages in the development of a typical 1 keV collision cascade near the [001] 28.073° (001) symmetrical twist boundary at parallel incidence to the boundary. The PKA was chosen to be at a distance of 17 Å from the boundary. The red circles represent vacancies and the green circles interstitials. a) 0.05 ps; b) 0.225 ps; c) 0.5 ps; d) 6 ps.
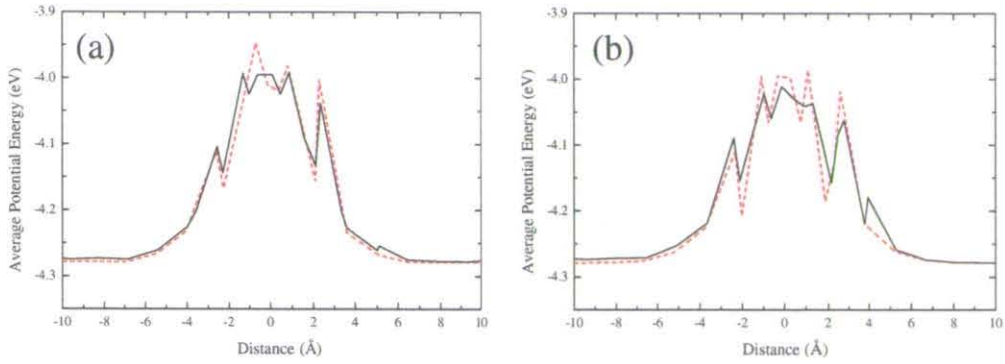
Figure 5.16: Average potential energy of atomic layers parallel to the grain boundary plane: relaxed configuration, dotted line, and damaged configuration after collision cascade, solid line. (a) 28.07° twist boundary without rigid body translation; (b) with rigid body translation

the grain boundary region. Clusters of up to 9 interstitials are found at the boundary after collision cascades of 1 keV. However, single interstitials are more frequently observed. This suggest the idea that the atomic structure is reordering as a effect of the radiation in a more stable configuration.
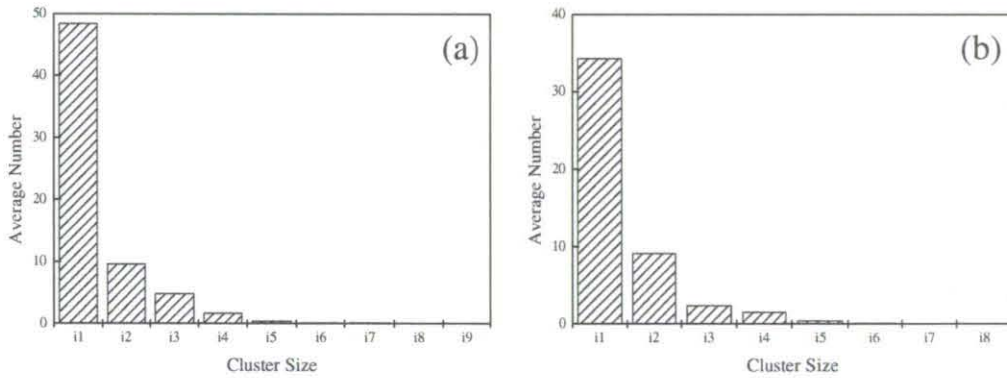
Figure 5.17: Cluster frequency of interstitials after collision cascades near the [001] 28.073° (001): (a) without, and (b) with rigid body translation.

To study in more detail what kind of reordering is taking place in the atomic structure of the boundary a similar study to the one employed to find 'preferential' sites in the tilt boundary model after radiation was used. In Figures 5.18 and 5.19, the position of all the defects which end up at the grain boundary generated for all the simulations is shown in a magnified region of the interface.

This pictures show that the major density of defects is well localized in the grain boundary region. In the case of the first model without translation, approximately
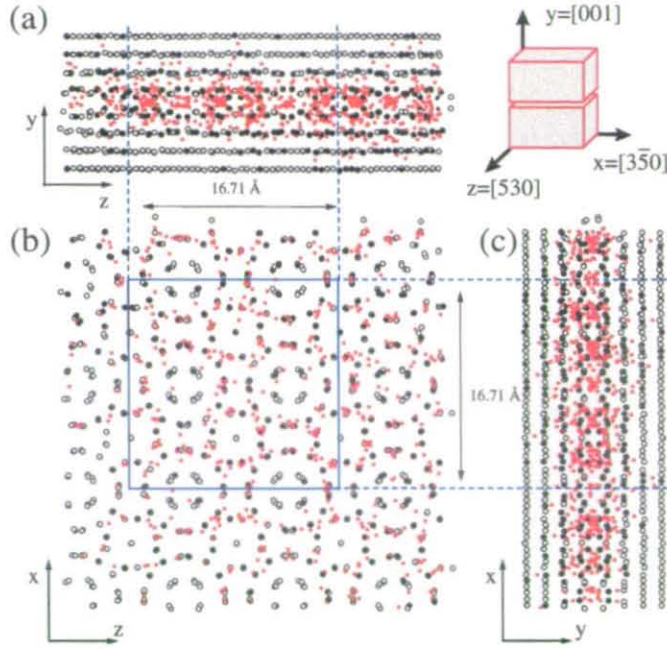
Figure 5.18: Open circles are the projection of atomic sites of the [001] 28.07°(001) symmetrical twist boundary before the collision cascades in different views: (a) top view, (b) front view. Black and red solid cicles are the projections of vacancies and interstitials respectively, plotted for all the simulations.
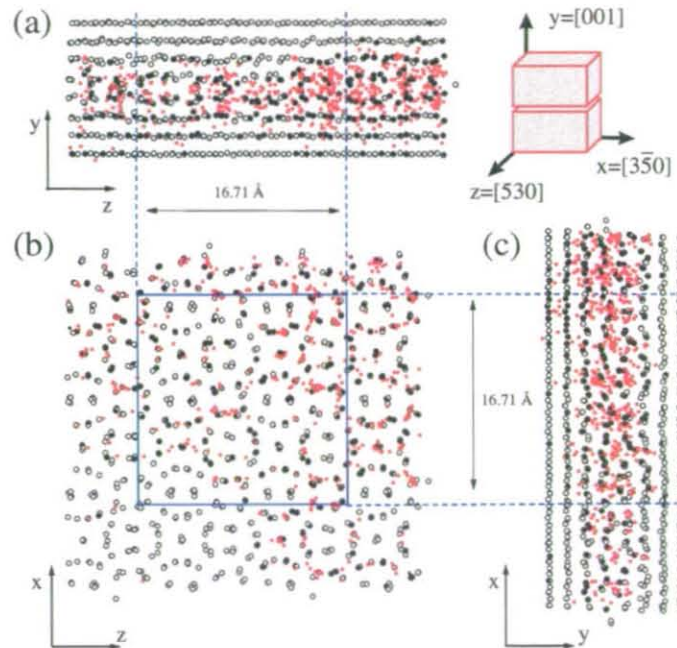

Figure 5.19: Initial [001] 28.07°(001) symmetrical twist boundary with rigid body translation. See caption in Figure 5.18.

75% of the defects inside the width of the boundary are in a region of approximately 2.5 Å . The second model, present similar results, being a region of 3 Å in length including the boundary which contains 75 % of defects in average produced by all the collision cascades.

The results seems to suggest that a new structure appears with major changes in the middle plane of the previous structures. Collision cascade simulations on this structures have favoured a further rearrangement of atomic sites resulting in structures with smaller grain boundary energies. In the previous chapter, a brief study of structure of this symmetrical twist boundary with additional atoms was made. This study showed that the grain boundary energy of this twist boundary models is reduced by adding atoms at the interface.

5.5   Conclusions

In this chapter the interaction of collision cascades with grain boundaries have been studied, using molecular dynamics simulations. The study has been performed for two different symmetrical boundaries of α-iron: a (530) symmetrical tilt and a [001] 28.07° (001) symmetrical twist grain boundary. Collision cascades generated by a PKA of 1 keV at various distances from the boundary and with different velocity directions were simulated.

The first stages of the collision cascade evolution demonstrated the same features as in a perfect crystal. However, the main differences appeared when the collision cascade spreads and reaches the boundary. When that happens, the grain boundary region acts as a barrier allowing, at this energy, i.e. 1 keV, only a few focused collisions to cross it. The final number of defects produced by the collision cascades shows that the boundary suffers a lot of damage in its structure compared with one produced by a collision cascade of 1 keV in a perfect crystal. This damage has been analysed for the two boundaries studied.

The majority of the defects produced after the collision cascades in the symmetrical tilt boundary have been shown to be very localised in a region defined by the closest atomic layers to the interface. In particular, this region is defined by the perpendicular length to the boundary of the repeated structural unit of this boundary.

Results show that there exist preferential sites in the (530) symmetrical tilt where defects are formed. These sites have been identified and also the atomic rearrangements produced in the grain boundary atomic structure have been analysed. In these

preferential sites, two different kind of dumbells, type 'a' and 'b', have been observed to be repeated in most of the simulations. In fact, a study of the clusters of interstitials in the final configuration shows that those composed of two interstitials are the most frequent.

Two mechanisms have been found to produce the type 'a' and 'b' defects. These two mechanisms are basically replacement collisions at the boundary region which end forming either of these two defects. The two mechanisms reflect how the grain boundary acts as a barrier and presents the grain boundary as a region where defects can be easily conducted along the boundary plane.

The grain boundary energy of the (530) symmetrical tilt boundary after radiation increases. It has been shown that the grain boundary energy is related to the number of defects at the grain boundary. An increasing number of defects placed between the width of the boundary region therefore represents an increase in the grain boundary energy.

Chapter 6

Conclusions and further work

This chapter provides a general overview of this research, discussing the main conclusions and highlighting those points where further work is required.

In this thesis, different modelling techniques, including physically based molecular dynamics simulations and empirical models using neural network architectures have been used to address particular problems in the understanding of microstructural development in iron-based systems.

The first part of the thesis was concerned with the application of neural network techniques to the prediction of final properties of submerged arc welds. Extensive analyses have been carried out concerned particularly with the prediction of weld metal chemistry, and also complex mechanical properties such as toughness, using neural network techniques and a database developed for one pass per side submerged arc welds typical of those used in the manufacture of linepipe. The neural network techniques used were based on a Bayesian framework, implemented using Markov chain Monte Carlo methods.

When predicting the final weld composition from known initial parameters the best neural network models are quite simple (for example, weld metal chemistry for a limited range of fluxes and 'simple' geometries). These models are basically composed of 5 input units, 1 output unit, being the final composition of the element, and a hidden layer composed of a 2 hidden units for most of the elements to be predicted. This relatively small number of hidden units indicates that a complex model is not required in this case for the prediction of the final weld composition. From this study, the initial plate and wire compositions of the element to be predicted have been shown to be the most influential parameters on the final output. In this case, where an intrinsically simple physical relationship exists between input variables (weld metal chemistry, in the case of welds which are designed to be at process equilibrium) the neural network does not provide a significant advantage over linear

regression techniques. However, for special cases, for example, the welds made with a NiMo flux, the neural network is able to provide 'fine tuning'.

However, in this thesis, the usefulness of neural network models for the prediction of complex mechanical properties, such as toughness, has been demonstrated. The optimal neural network architecture obtained to predict toughness is very complex, i.e. 13 input and 7 hidden units, indicating the highly non-linear nature of this mechanical property. Final weld composition and microstructural characteristics are mainly used as input parameters for the model. The model indicates that test temperature and the percentage of acicular ferrite are the most influent parameters when predicting toughness.

An important point in the use of neural networks is not only the quantity of data available for meaningful predictions but also the pre-handling of this data. It is therefore imperative to carefully consider the structure of the data and the choice of parameters to be involved in the neural network model, i.e. input and output units, before time is expended in creating complex neural network models.

The ability to predict the mechanical properties of a weld is of great commercial significance, with large potential savings if the need for experimental test weld programs can be eliminated. The main aim of future work, would be to deliver a piece of stand-alone software which could be thought of as an 'expert system' to enable predictions of weld metal chemistry and weld metal properties from a knowledge of plate and wire type and welding parameters.

This thesis deals with only a couple of examples where neural network techniques can be applied on the welding industry. They can already provide valuable information from the engineering point of view for the prediction and control of final products. However, the application of neural network techniques is a relatively new field of research in continuous evolution. Future work in the development of new algorithms has to focus on the way input parameters are relevant to the prediction of the final output when using such highly non-linear models. This is an important point which clearly will increase the usefulness of neural network models in industry.

The second part of this thesis has been devoted to the study, on the atomic scale, of radiation damage near grain boundaries using molecular dynamics simulations. The study has been performed in α-iron because of its importance in the nuclear and power generation industries.

A total of 15 symmetrical tilt and 10 symmetrical twist boundaries with different misorientation angles, all of them with the rotation axis along the [001] direction of the bcc structure, have been studied. The relaxed atomic structures of the symmetrical

tilt boundaries were found to be periodic along the boundary. Each boundary has a different atomic structure characterised by different combinations of three basic 'units'. These units are three different groups of atoms which are combined in different numbers to form the grain boundary. These structural units are the ones which form the (100), (110) and (310) symmetrical tilt boundaries, which are the boundaries with shortest periodicity along the boundary of this [001] symmetrical tilt.

Most of relaxed structures found for the symmetrical twist boundaries also present a clear periodic structure, however basic units could not be identified for these models, as was the case for the tilt boundaries, because they relax to less symmetric structures.

In all cases, the final grain boundary structures have been classified in terms of energy, width and expansion of the distorted region. The grain boundary energy values have been obtained considering a perfect crystal as a reference. The grain boundary energy, when plotted as a function of the misorientation angle for the tilt models, shows small 'cusps' for certain 'special' boundaries. The grain boundary energy values, obtained with the many-body potential of the Finnis-Sinclair form, are slightly bigger for the [001] twist than for the tilt boundaries. A definition of the width of the grain boundary has been given and this definition has been applied to all the models studied.

In the case of one particular twist boundary, i.e. [001] 28.07° (001), an additional approach was also used in which particles were added to the interface region after rotation because gaps appeared along the interface at various periodic sites. Final configurations with smaller grain boundary energy values were obtained. This brief study suggested that more stable twist boundaries can be obtained by adding additional particles to the CSL initial structure.

Following the structural study of symmetrical boundaries, the effects of radiation damage in two particular symmetrical boundaries have been analysed. Simulations of collision cascades near a (530) symmetrical tilt boundary and also near a [001] 28.07° (001) symmetrical twist boundary have been performed. The damage has been analysed in terms of vacancies and interstitials using the same definition as those used in a perfect crystal.

The main differences observed for collision cascade near a grain boundary with respect to those in a perfect crystal, appeared when the collision cascade spreads and reaches the boundary. When that happens, the grain boundary region acts as a barrier allowing, at this energy, i.e. 1 keV, only a few focused collisions to cross it. Also, the final number of defects produced by the collision cascades shows that the boundary suffers a lot of damage in its structure compared with the one produced by a collision cascade of 1 keV in a perfect crystal.

The results of the simulations in a bicrystal forming a (530) symmetrical tilt boundary show that most of the defects are very localised in a region of approximately 2.5 Å in the middle of the boundary, and which is determined by the vertices of the repeated structural unit forming this interface. Inside this region, results show that there are preferential sites where defects are easily formed. These sites have been identified and also the atomic rearrangements produced in the grain boundary structure have been analysed.

Two different combinations of clusters composed of two interstitials, which are the most common cluster size founded after radiation in the (530) symmetrical tilt, have been found. These two types of clusters, 'a' and 'b', have been observed to be repeated in most of the simulations and to be placed in the preferential sites of the boundary. Two mechanisms have been found to produce the type 'a' and 'b' defects. These two mechanisms are basically replacement collisions at the boundary region which ended forming either of these two defects. These two mechanisms reflect how the grain boundary acts as a barrier and also presents the grain boundary as a region where defects can be easily conducted along the boundary plane.

A key point in this study is how radiation damage affects the grain boundary energy of the interfaces. After radiation damage in the (530) boundary, the grain boundary energy increases. This increase in energy has been shown to be proportional to the number of defects which are inside the grain boundary region.

On the other hand, the grain boundary energy after radiation damage in two different models containing the [001] 28.07° (001) twist boundary decreases, rather than increases as expected. This suggests that the initial grain boundary chosen might have a more stable structure than the one obtained by our relaxation method. One approach to determine this might be by adding extra atoms to the interface. Another possibility would be to find the minimum relaxed structures of the boundaries by allowing more random positional changes to atoms in the grain boundary region and relaxing these structures. However, these procedures are beyond the scope of this thesis, and should be the subject of future work.

Future work is also suggested to be focused on a systematic study of collision cascade simulations near different symmetrical tilt boundaries. The main aim of this work would be the generalisation of some of the results found in this work for the (530) symmetrical tilt boundary, including: the increasing of grain boundary energy as a function of the number of defects for different boundaries; the relationship between preferential sites at the boundary and the structural units forming the boundary; characterisation of clusters formed at the boundary; and typical mechanisms such as replacement collisions which appeared along the boundary.

In this research a many-body potential for bcc iron was used as a simplification of steel. Another direction for further research would be the development of a realistic interatomic potential of steel, allowing for the presence of interstitial carbon atoms. This new potential could be based on energetics derived from ab-initio calculations. It might also be possible to include a good description of properties such as the magnetic behaviour and also phase transformations.

The molecular dynamics code used in this research is not optimised for its use in parallel computing systems. During the performance of this research an attempt was made to adapt some of the most computational time expensive subroutines into a parallel code, in particular the OpenMP (shared memory approach). The use of parallel computational systems in molecular dynamics clearly improves the possibilities of simulation. This would allow the simulation of bigger systems, and therefore collision cascades at higher energies. The optimisation of the actual code is under development at Loughborough University.

The ultimate main potential application of this work would be to convert it into quantitative data concerning reactor safety. The aim would be to estimate the average number of defects created per grain boundary per unit time and relate it to the increased potential energy of the boundaries and the subsequent embrittlement produced as a function of the exposure time. This information could be in principle extracted from this more fundamental study, however it would be more reliable when further work concerning the motion of impurities is included. This work should be performed with a technique able to simulate longer time scales, such as Hyper-MD now in development at Loughborough University for the study of diffusion of clusters. This thesis has been a necessary precursor to work involving impurities and how their segregation towards grain boundaries is affected by radiation, and now provides a firm foundation for the future.

Bibliography

[1] M. F. Ashby, Materials Science and Technology **8** (1992) 102.

[2] M. C. Payne, M. P. Teter, D. C. Allan, T. A. Arias and J. D. Joannopoulos, Review of Modern Physics **64** (4) (1992) 1045.

[3] W. E. King, G. Campbell, T. Gonis, G. Henshall, D. Lesuer, E. Zywicz and S. Foiles, Materials Science and Engineering A **191** (1995) 1.

[4] D. J. Bacon, Nuclear Instruments and Methods in Physics Research B **153** (1-4) (1999) 87.

[5] Neural networks newsgroup at com.ai.neural-nets, and Frequently Asked Questions available at ftp://ftp.sas.com/pub/neural/FAQ.html.

[6] W. Duch and G. H. F. Diercksen, Computer Physics Communication **82** (1994) 91.

[7] H. K. D. H. Bhadeshia, ISIJ International **39** (10) (1999) 966; R. C. Thomson, F. J. Pérez-Pérez, A. D. Warters and G. Thewlis, ISIJ International **39** (10) (1999) 1096.

[8] ISIJ International **39** (10) (1999), special Issue on Application of Neural Network Analysis in Materials Science.

[9] G. E. Hinton, Scientific American (September) (1992) 105.

[10] D. R. Baughman, *Neural Networks in Bioprocessing and Chemical Engineering* (Academic Press, London, 1995).

[11] D. J. C. Mackay, Neural Computation **4** (3) (1992) 415.

[12] D. J. C. Mackay, Neural Computation **4** (3) (1992) 448.

[13] D. J. C. Mackay, Bayesian Methods for Neural Networks: Theory and Applications, available at http://wol.ra.phy.cam.ac.uk/mackay.

[14] R. M. Neal, *Bayesial Learning for Neural Networks* (Springer Verlag, New York, 1996).

[15] D. J. C. Mackay , bigback version 5, non-linear data modelling tool combining Bayesian probability theory with neural networks, available at http://wol.ra.phy.cam.ca.uk/mackay.

[16] S. Duane, A. D. Kennedy, B. J. Pendleton and D. Roweth, Physics Letters B **195** (2) (1987) 216.

[17] C. E. Rasmussen, Bayesian Learning in Feed Forward Neural Networks, available at http://www.cs.toronto.edu/~carl.

[18] C. E. Rasmussen, in *Advances in Neural Information Processing Systems* (D. S. Touretzky, M. C. Mozer and M. E. Hasselmo, eds.) (MIT Press, 1996) pp. 598–604.

[19] R. M. Neal, Software for Flexible Bayesian Learning, available at http://www.cs.toronto.edu/~radford/.

[20] M. P. Allen and D. J. Tildersley, *Computer Simulation of Liquids* (Clarendon Press, Oxford, 1987).

[21] W. Eckstein, *Computer Simulation of Ion-Solid Interactions* (Springer Verlag, Berlin, 1991).

[22] L. Verlet, Physical Review **159** (1967) 98.

[23] R. Smith and D. E. Harrison, Computers in Physics (Sep/Oct) (1989).

[24] K. Beardmore, *Dynamical Simulations of Multicomponent Carbon Based Materials*, Ph.D. thesis, Loughborough University, (1995).

[25] R. Smith, *Atomic & Ion Collisions in Solids and at Surfaces. Theory, Simulations & Applications* (Cambridge University Press, Cambridge, 1997).

[26] D. C. Rapaport, Comp. Phys. Rep. **9** (1988) 1.

[27] R. A. Johnson, *Interatomic Potential Development in Materials Science* (ASM-International, 1988) pp. 29–44.

[28] J. Tersoff, Physical Review B **37** (1988) 6991.

[29] M. S. Daw and M. I. Baskes, Physical Review B **29** (12) (1984) 6443.

[30] M. W. Finnis and J. E. Sinclair, Philosophical Magazine A **50** (1) (1984) 45.

[31] M. W. Finnis and J. E. Sinclair, Philosophical Magazine A **53** (1986) 161.

[32] F. Ercolessi, E. Tosatti and M. Parinello, Physical Review Letters **57** (1986) 719.

[33] S. M. Foiles, MRS Bulletin (February) (1996) 24.

[34] A. E. Carlsson, Physical Review B **44** (1991) 6590.

[35] A. G. Marinopoulos, V. Vitek and A. E. Carlsoon, Philosophical Magazine A **72** (5) (1995) 1311.

[36] A. P. Sutton and R. W. Ballufi, *Interfaces in Crystalline Materials* (Oxford University Press, Oxford, 1996).

[37] A. F. Calder and D. J. Bacon, Journal of Nuclear Materials **207** (1993) 25.

[38] M. Marchese, G. Jacucci and C. P. Flynn, Philosophical Magazine Letters **57** (1) (1988) 25.

[39] J. Biersack and J. Ziegler, Nuclear Instruments and Methods **141** (1982) 93.

[40] C. Kolb, *Rayshade Manual*, Computer Science Department, Princeton University, (1992).

[41] Microcal Origin version 5.0, Microcal Software, Inc.

[42] L. E. Svensson, *Control of Microstructures and Properties in Steel Arc Welds* (CRC Press, 1994).

[43] T. H. North, H. B. Bell, A. Nowicki and I. Craig, Welding Research Supplement (1978) 63.

[44] J. E. Indacochea, M. Blander and D. L. Olson, Metallurgical Transactions B **16B** (1985) 237.

[45] T. Lau, G. C. Weatherly and A. McLean, Welding Research Supplement (1986) 31.

[46] G. Thewlis, Joining Materials (1989) 25 and 125.

[47] J. Tanaka, T. Kitada, Y. Naganawa, Y. Kunisada and H. Nakagawa, in *Proc. Int. Conf. Weld Pool Chemistry and Metallurgy* (The Welding Institute, London, 1980) p. 279.

[48] M. L. E. Davis and N. Bailey, in *Proc. Int. Conf. Weld Pool Chemistry and Metallurgy* (The Welding Institute, London, 1980) p. 289.

[49] H. Thier, in *International Conference on Weld Pool Chemistry and Metallurgy* (The Welding Institute, London, 1980) p. 271.

[50] H. Thier and R. Killing, Quantitative Determination of Metallurgical Reactions in Arc Welding Processes, Tech. Rep. IIW Doc. XXI-E-78, (1978).

[51] U. Mitra and T. W. Eagar, Metallurgical Transactions B **22B** (1991) 65.

[52] G. Thewlis and J. R. Dainty, in *Proc. 2nd Int. Pipeline Technology Conf., Ostend, Belgium* (R. Denys, ed.), vol. I (Elsevier Science B. V., 1995) pp. 173–184.

[53] R. S. Chandel and S. R. Bala, Welding Cutting **2** (1988) E28.

[54] R. S. Chandel, Materials Science Technology **6** (1990) 772.

[55] H. H. Thodberg, IEEE Transactions on Neural Networks **7** (1) (1996) 56.

[56] O. M. Akselsen and O. Grong, Materials Science and Engineering **159** (1992) 187.

[57] H. K. D. H. Bhadeshia, D. J. C. Mackay and L. E. Svensson, Materials Science and Technology **11** (1995) 1046.

[58] MAP, Materials Algorithms Project Library, available at http://www.msm.cam.ac.uk/map/mapmain.html.

[59] T. Cool, H. K. D. H. Bhadeshia and D. J. C. Mackay, Materials Science and Engineering A **223** (1997) 186.

[60] D. Wolf and S. Yip (eds.), *Materials Interfaces. Atomic-Level Structure and Properties* (Chapman & Hall, London, 1992).

[61] D. McLean, *Grain Boundaries in Metals* (Oxford University Press, Oxford, 1957).

[62] D. N. Seidman, *Experimental investigation of internal interfaces in solids* (Chapman & Hall, London, 1992) pp. 58–84.

[63] W. T. Read and W. Shockley, Physical Review **78** (3) (1950) 275.

[64] *Metals Handbook*, vol. 9, Metallography and Microstructure, 9th ed. (American Society for Metals, Ohio, 1985).

[65] L. Priester, J. Thibault and V. Pontikis, Solid State Phenomena **59-60** (1998) 1.

[66] V. Paidar, Key Engineering Materials **103** (1995) 79.

[67] G. Palumbo, E. M. Lehockey and P. Lin, JOM-Journal of the Minerals & Materials Society **50** (2) (1998) 40.

[68] K. L. Merkle, J. Phys. Chem. Solids **55** (10) (1994) 991.

[69] K. L. Merkle, Microscopy and Microanlaysis **3** (1997) 339.

[70] K. L. Merkle and L. J. Thompson, Physical Review Letters **83** (3) (1999) 556.

[71] R. J. Harrison, G. A. Bruggeman and G. H. Bishop, *Computer Simulation Methods Applied to Grain Boundaries* (Academic Press, 1976) pp. 45–91.

[72] R. Wu, A. J. Freeman and G. B. Olson, Science **265** (1994) 376.

[73] A. Paxton, Journal of Physics D. Applied Physics **29** (1996) 1689.

[74] M. Sob, I. Turek and V. Vitek, Materials Science Forum **294-296** (1999) 17.

[75] S. M. Woodley, P. D. Battle, J. D. Gale, C. Richard and A. Catlow, Physical Chemistry Chemical Physics **1** (1999) 2535.

[76] U. Dahmen, C. J. D. Hetherington, M. A. O'Keefe, K. H. Westmacott, M. . J. Mills, M. S. Daw and V. Vitek, Philosophical Magazine Letters **62** (5) (1990) 327.

[77] W. Krakow, Philosophical Magazine A **63** (2) (1991) 233.

[78] G. H. Campbell, S. M. Foiles, P. Gumbsch, M. Ruhle and W. E. King, Physical Review Letters **70** (4) (1993) 449.

[79] M. E. Azzaoui, J. M. Penisson and V. Pontikis, Interface Science **2** (1994) 79.

[80] C. Schmidt, F. Ernst, M. W. Finnis and V. Vitek, Physical Review Letters **75** (11) (1995) 2160.

[81] K. Morita and H. Nakashima, Materials Science and Engineering A **234-236** (1997) 1053.

[82] M. Bacia, J. Morillo, J. M. Penisson and V. Pontikis, Philosophical Magazine A **76** (5) (1997) 945.

[83] W. Bollmann, *Crystal Defects and Crystalline Interfaces* (Springer Verlag, Berlin, 1970).

[84] D. Romeu, L. B. del Rio, J. L. Aragon and A. Gomez, Physical Review B **59** (7) (1999) 5134.

[85] M. F. Ashby, F. Spaepen and S. Williams, Acta Metallurgica **26** (1978) 1647.

[86] A. P. Sutton and V. Vitek, Philosophycal Transactions of the Royal Society of London A **309** (1983) 1.

[87] G. J. Wang, A. P. Sutton and V. Vitek, Acta Metallurgica **32** (7) (1984) 1093.

[88] G. C. Hasson, J. B. Guillot, B. Baroux and C. Goux, Physica Status Solidi A **2** (1970) 551.

[89] M. J. Weins, H. Gleiter and B. Chalmers, Journal of Applied Physics **42** (7) (1971) 2639.

[90] G. Hasson, J.-Y. Boos, I. Herbeuval, M. Biscondi and C. Goux, Surface Science **31** (1972) 115.

[91] M. J. Weins, Surface Science **31** (1972) 138.

[92] D. A. Smith, V. Vitek and R. C. Pond, Acta Metallurgica **25** (1977) 475.

[93] P. D. Bristowe and A. G. Crocker, Philosophical Magazine **38** (5) (1978) 487.

[94] R. C. Pond, D. A. Smith and V. Vitek, Acta Metallurgica **27** (1979) 235.

[95] D. Schwartz, V. Vitek and A. P. Sutton, Philosophical Magazine A **51** (4) (1985) 499.

[96] J. F. Lutsko, D. Wolf, S. Yip, S. R. Phillpot and T. Nguyen, Physical Review B **38** (16) (1988) 11572.

[97] D. Wolf, Acta Metallurgica **37** (7) (1989) 1983.

[98] M. W. Finnis, Materials Science Forum **207-209** (1996) 35.

[99] N. Chandra and P. Danga, Journal of Materials Science **34** (1999) 655.

[100] R. J. Kurtz, Philosophical Magazine A **79** (3) (1999) 683.

[101] D. Wolf, Acta Metallurgica **32** (2) (1984) 245.

[102] D. Wolf, Acta Metallurgica **32** (5) (1984) 735.

[103] P. D. Bristowe and A. G. Crocker, Philosophical Magazine **31** (1975) 503.

[104] V. Vitek, D. Smith and R. Pond, Philosophical Magazine A **41** (5) (1980) 649.

[105] M. Hashimoto, Y. Ishida, R. Yamamoto and M. Doyama, Acta Metallurgica **32** (1) (1984) 1.

[106] D. Wolf, Philosophical Magazine B **59** (6) (1989) 667.

[107] D. Wolf, Philosophical Magazine A **62** (4) (1990) 447.

[108] R. A. Johnson, Physical Review **134** (5) (1964) A1329.

[109] R. J. Harrison, A. F. Voter and S.-P. Chen, *Embedded Atom Potential for bcc-Iron* (Plenum, New York, 1989) pp. 219–222.

[110] F. Gao, R. L. Johnston and J. N. Murrell, Journal of Physical Chemistry **97** (1993) 12073.

[111] G. Simonelli, R. Pasianot and E. J. Savino, Physical Review B **50** (2) (1994) 727.

[112] R. Watanabe, A. Nogami and T. Matsumiya, Materials Science Forum **204-206** (1996) 227.

[113] R. Wu, A. J. Freeman and G. B. Olson, Physical Review B **50** (1) (1994) 75.

[114] D. Wolf, *Atomic-level geometry of crystalline interfaces* (Chapman & Hall, London, 1992) pp. 1-57.

[115] D. Wolf, Grain Boundaries: Structure, preprint to be submitted for publication in The Encyclopedia of Matarials: Science and Technology.

[116] M. M. Jakas and D. E. Harrison, Physical Review B **30** (6) (1984) 3573.

[117] M. M. Jakas and D. E. Harrison, Physical Review B **32** (5) (1985) 2752.

[118] V. Y. Gertsman, A. A. Nazarov, A. E. Romanov, R. Z. Valiev and V. I. Vladimirov, Philosophical Magazine A **59** (5) (1989) 1113.

[119] K. Morita, M. Uehara, S. Tsurekawa and H. Nakashima, Journal of the Japanese Institute of Metals **61** (4) (1997) 251.

[120] M. R. Fitzsimmons and S. L. Sass, Acta metallurgica **37** (4) (1989) 1009.

[121] D. Wolf and K. L. Merkle, *Correlation Between the Structure and Energy of Grain Boundaries in Metals* (Chapman & Hall, London, 1992) pp. 87-150.

[122] D. Yesilleten, M. Nastar, T. A. Arias, A. T. Paxton and S. Yip, Physical Review Letters **81** (14) (1998) 2998.

[123] L. H. V. Vlack, Transactions AIME (March 1951) 251.

[124] J. L. Nilles and D. L. Olson, Journal of Appliled Physics **41** (2) (1970) 531.

[125] L. E. Murr, *Interfacial Phenomena in Metals and Alloys* (Addison-Wesley, 1975).

[126] P. Lejček, V. Paidar and S. Hofmann, Materials Science Forum **294-296** (1999) 103.

[127] G. J. Wood, W. M. Stobbs and D. J. Smith, Philosophical Magazine A **50** (3) (1984) 375.

[128] K. L. Merkle and D. J. Smith, Physical Review Letters **59** (25) (1987) 2887.

[129] F. L. Vook, Physics Today (September) (1975) 34.

[130] E. P. Wigner, Journal of Applied Physics **17** (11) (1946) 857.

[131] W. J. Phythian and C. A. English, Journal of Nuclear Materials **205** (1993) 162.

[132] B. N. Singh, Radiation Effects and Defects in Solids **148** (1999) 383.

[133] L. T. Chadderton, *Radiation Damage in Crystals* (Methuen & Co., London, 1965).

[134] F. Seitz, Discussions of the Faraday Society (5) (1949) 271.

[135] F. Seitz, Physics Today **5** (6) (1952) 6.

[136] J. A. Brinkman, Journal of Applied Physics **25** (8) (1954) 961.

[137] J. A. Brinkman, American Journal of Physics **24** (1956) 246.

[138] G. H. Kinchin and R. S. Pease, Reports on Progress in Physics **18** (1955) 1.

[139] L. T. Chadderton and I. M. Torrens, *Fission Damage in Crystals* (Methuen & Co., 1969).

[140] F. Seitz and Koehler, Solid State Physics **2** (1956) 305.

[141] M. Yoshida, Journal of the Physical Society of Japan **16** (1) (1961) 44.

[142] M. J. Norgett, M. T. Robinson and I. M. Torrens, Nuclear Engineering and Design **33** (1975) 50.

[143] J. Silcox and P. B. Hirsch, Philosophical Magazine **4** (43) (1959) 1356.

[144] A. Seeger, in *Radiation Damage in Solids* (International atomic energy agency, Vienna, 1962) pp. 101–127.

[145] R. H. Silsbee, Journal of Applied Physics **28** (11) (1957) 1246.

[146] J. B. Gibson, A. N. Goland, M. Milgram and G. H. Vineyard, Physical Review **120** (4) (1960) 1229.

[147] G. H. Vineyard, Discussions of the Faraday Society (31) (1961) 7.

[148] C. Erginsoy, G. H. Vineyard and A. Englert, Physical Review **133** (2A) (1964) 595.

[149] C. A. English, A. J. E. Foreman, W. J. Phytian, D. J. Bacon and M. L. Jenkins, Materials Science Forum **97-99** (1992) 1.

[150] D. J. Bacon and T. D. de la Rubia, Journal of Nuclear Materials **216** (1994) 275.

[151] T. D. de la Rubia, N. Soneda, M. J. Caturla and E. A. Alonso, Journal of Nuclear Materials **251** (1997) 13.

[152] R. E. Stoller, G. R. Odette and B. D. Wirth, Journal of Nuclear Materials **251** (1997) 49.

[153] J. J. R. Beeler, Journal of Applied Physics **35** (7) (1964) 2226.

[154] W. E. King and R. Benedek, Journal of Nuclear Materials **117** (1983) 26.

[155] M. T. Robinson, Journal of Nuclear Materials **216** (1994) 1.

[156] T. D. de la Rubia, M. J. Caturla, E. A. Alonso, N. Soneda and M. D. Johnson, Radiation Effects in Solids **148** (1999) 95.

[157] D. J. Bacon, A. F. Calder, F. Gao, V. G. Kapinos and S. J. Wooding, Nuclear Instruments and Methods in Physics Research B **102** (1995) 37.

[158] D. J. Bacon, A. F. Calder and F. Gao, Journal of Nuclear Materials **251** (1997) 1.

[159] N. Soneda and T. D. de la Rubia, Philosophical Magazine **78** (5) (1998) 995.

[160] Y. N. Osetsky, D. J. Bacon and A. Serra, Philosophical Magazine Letters **79** (5) (1999) 273.

[161] P. Lejček and S. Hofmann, Critical Reviews in Solid State and Materials Sciences **20** (1) (1995) 1.

[162] E. D. Hondros and M. P. Seah, International Metals Reviews **22** (1977) 262.

[163] S. Hofmann and P. Lejček, Interface Science **3** (1996) 241.

[164] F. J. Pérez-Pérez and R. Smith, Nuclear Instruments and Methods in Physics Research B **153** (1999) 136.

[165] F. J. Pérez-Pérez and R. Smith, Nuclear Instruments and Methods in Physics Research B (2000), accepted for publication.

[166] K. Sugio, Y. Shimomura and T. D. de la Rubia, Journal of the Physical Society of Japan **67** (3) (1998) 882.

[167] E. Ruedl, P. Delavignette and S. Amelinckx, Physical Review Letters **6** (10) (1961) 530.

[168] M. F. Chisholm, A. Maiti, S. J. Pennycook and S. T. Pantelides, Materials Science Forum **294-296** (1999) 161.

[169] R. S. Barnes, Philosophical Magazine **5** (1960) 635.